

DISSERTATION

Integrated Millimeter Wave Front-End Design in SiGe Bipolar Technology

ausgeführt zum Zwecke der Erlangung des akademischen Grades eines Doktors
der technischen Wissenschaften unter der Leitung von

Ao. Univ. Prof. Dr. Arpad L. Scholtz

E389

Institut für Nachrichtentechnik und Hochfrequenztechnik

eingereicht an der Technischen Universität Wien
Fakultät für Elektrotechnik und Informationstechnik

von

Dipl.-Ing. Bernhard Dehlink

Matrikelnummer 9825109

Magdalenengasse 13

A-2540 Bad Vöslau

Wien, im Juni 2007

Begutachter: Ao.Univ.Prof. Dipl.-Ing. Dr.techn. Arpad L. Scholtz

O.Univ.Prof. Dipl.-Ing. Dr.techn. Gottfried Magerl

Abstract

Decreasing the number of road accidents is a major objective of governments worldwide. A big step to achieve this goal is the implementation of on-board systems that capture the surroundings of motorized vehicles. These systems extend the driver's perception and support his reaction. Recent advancements in Silicon-Germanium bipolar technology will drop the cost of millimeter-wave radar based safety systems, which will result in their implementation even in low-budget cars. The effect were a substantial improvement in road safety.

This work presents the design, implementation, and characterization of millimeter-wave receiver circuits in SiGe bipolar technology. The target applications are long-range and short-range automotive radar. One circuit has the additional feature of being suitable for high data rate point-to-point communication. These systems operate in the frequency range from 76 to 86 GHz, which is a major challenge in the design process. The development of two integrated receiver circuits for different applications is elaborated.

The first design consists of an active down-conversion mixer for long-range automotive radar systems in the frequency range from 76 to 77 GHz. The circuit comprises a double-balanced mixer and on-chip single-ended to differential signal converters at the local oscillator as well as the signal port. The goal of this design is the simultaneous achievement of high linearity and low noise figure. The integrated circuit exhibits a measured input-referred 1 dB gain compression point of 0 dBm and a measured single-sideband noise figure of 16.5 dB. The conversion gain is 11 dB. This circuit consumes 75 mA from a 5.5 V supply.

The second integrated circuit is a receiver front-end that exhibits a high integration level of millimeter-wave components. The front-end covers either short-range automotive radar applications (77-81 GHz) or communication purposes (81-86 GHz). The integrated circuit employs a low-noise amplifier, single-ended to differential signal converters, and down-conversion mixers that deliver differential quadrature output signals. The quadrature generation is done on-chip by a passive transmission line coupler. The receiver front-end exhibits a single-sideband noise figure smaller than 12 dB and a conversion gain larger than 28 dB over the whole frequency range. The quadrature mismatch is at most 8°. The input-referred 1 dB gain compression point, measured at 79 GHz, is -19 dBm. The front-end consumes 192 mA from a 5.5 V supply.

Kurzfassung

Die jährlichen Statistiken zu Verkehrsunfällen zeigen auf, dass Maßnahmen zur langfristigen Erhöhung der Verkehrssicherheit getroffen werden müssen. Fortschritte in der Entwicklung von Silizium-Germanium Bipolartechnologie bieten die Möglichkeit Systeme, welche die Fahrzeugumgebung erfassen und den Fahrer auf Gefahrensituationen aufmerksam machen, günstig anzubieten. Dadurch kann die Zahl der Verkehrsunfälle drastisch gesenkt werden.

In dieser Arbeit wird die Entwicklung und Charakterisierung von integrierten Schaltungen im Millimeterwellenbereich beschrieben. Die Einsatzgebiete der Schaltungen reichen von Nah- und Fernbereichsradar bis hin zu schneller Datenkommunikation. Der verwendete Frequenzbereich liegt zwischen 76 und 86 GHz. Diese hohen Frequenzen erfordern spezielle Maßnahmen bei der Entwicklungsarbeit. Zwei Schaltungen für unterschiedliche Applikationen werden vorgestellt.

Zunächst wird ein aktiver Abwärtsmischer für den Einsatz in einem Fernbereichsradarsystem präsentiert. Die Arbeitsfrequenz liegt zwischen 76 und 77 GHz. Die integrierte Schaltung beinhaltet neben der aktiven differentiellen Mischerzelle auch passive Elemente zur Transformation der asymmetrischen Eingangssignale auf differentielle Signale. Besonderes Augenmerk beim Entwurf dieser Schaltung wurde auf das gleichzeitige Erreichen hoher Linearität und niedriger Rauschzahl gelegt. Der gemessene eingangsseitige 1 dB Verstärkungskompressionspunkt von 0 dBm und die Einseitenbandrauschzahl von 16.5 dB bestätigen das Erreichen dieses Ziels. Der Konversionsgewinn ist 11 dB. Der Mischer benötigt 75 mA bei einer Versorgungsspannung von 5.5 V.

Als zweite Schaltung wird ein Empfänger vorgestellt, der einen hohen Integrationsgrad an Hochfrequenzkomponenten aufweist. Als Anwendungen kommen Nahbereichsradar oder Datenkommunikation in Frage. Die integrierte Schaltung besteht aus einem rauscharmen Verstärker, Konvertern zur Umwandlung der asymmetrischen in differentielle Signale, Abwärtsmischern und Verstärkern für das Oszillatorsignal. Die Ausgangssignale dieses Empfängers sind differentiell und 90° phasenverschoben, was durch eine passive Kopplerstruktur auf dem Chip erreicht wird. Der Empfänger weist eine gemessene Einseitenbandrauschzahl kleiner als 12 dB bei einem Konversionsgewinn von mehr als 28 dB über den gesamten Frequenzbereich auf. Die Abweichung der Phasen der Ausgangssignale von 90° beträgt höchstens 8°. Der eingangsseitige 1 dB Kompressionspunkt ist -19 dBm, gemessen bei 79 GHz. Der Empfänger arbeitet an 5.5 V und benötigt 192 mA.

Acknowledgement

This thesis was performed at Infineon Technologies AG, Munich, Germany, and supported by the "Deutsches Bundesministerium für Bildung und Forschung (BMBF)" under contract 10 M3161A (KOKON). The work started at Corporate Research, department for High Frequency Circuits (CPR HF), and was finished at the department COM PS CE AC.

I express sincere appreciation to my advisor Prof. Arpad L. Scholtz for his guidance and support throughout my studies, and for giving me the chance to be part of the cooperation with Infineon. My gratitude goes to Prof. Gottfried Magerl for critical reading of the manuscript.

I would like to thank Werner Simbürger from Infineon Technologies AG for his sustained support, especially for providing a scientific environment within Infineon.

My most profound thanks go to my former supervisor at Infineon, Hans-Dieter Wohlmuth, who advanced my work with inspiring ideas and helpful discussions. I appreciate the support I received from Herbert Knapp, Klaus Aufinger, Saverio Trotta, and Ronald Thüringer, and I thank them for their valuable inputs.

I especially thank Hans-Dieter, Herbert, and Klaus for carefully reviewing this thesis.

I express gratitude to my parents, Brigitta and Alois, and to my sister Eleonora and her fiancé Franz, who enabled my education by their unshakable faith and their support. Finally, I thank my partner Elisabeth for encouraging and supporting me in any situation of my life.

Contents

Abstract	i
Kurzfassung	ii
Acknowledgement	iii
1 Introduction	1
2 Radar Systems	6
2.1 General Aspects	6
2.2 Frequency-Modulated Continuous-Wave Radar	9
2.3 Pulse-Doppler Radar	14
2.4 Direct-Sequence Spread-Spectrum Radar	16
3 Infineon's SiGe:C Bipolar Technology	19
3.1 High-Speed NPN Bipolar Transistor	19
3.2 Resistors	24
3.3 Metal-Insulator-Metal Capacitor	25
3.4 Transmission Lines	26
4 Highly Linear 77 GHz Down-Conversion Mixer	37
4.1 Design Considerations	37
4.1.1 Mixer Core	40
4.1.2 Local Oscillator Buffer	41
4.1.3 Balun Design	46
4.2 Performance Parameters	50
4.2.1 Linearity	50
4.2.2 Noise	56
4.2.3 Stability	66
4.2.4 Local Oscillator Amplitude Noise Suppression	71
4.2.5 Local Oscillator Leakage	72
4.2.6 Sensitivity Analysis	74
4.3 Measurement Results	75
4.3.1 Noise Figure and Conversion Gain	79
4.3.2 1 dB Compression Point	89

4.3.3	Third-Order Intercept Point	90
4.3.4	DC Offset	92
4.3.5	Matching and Isolation	92
4.3.6	Temperature Behavior	93
4.3.7	Measurement Repeatability	93
4.4	Summary	96
5	80 GHz Quadrature Receiver Front-End	97
5.1	Receiver Front-End Design	97
5.1.1	Low-Noise Amplifier	98
5.1.2	I/Q Mixer	105
5.2	Measurement Results	110
5.2.1	Noise Figure and Conversion Gain	111
5.2.2	Linearity	113
5.2.3	I/Q Mismatch	114
5.2.4	Temperature Behavior	117
5.2.5	Matching and Isolation	117
5.3	Summary	119
6	Conclusion and Outlook	120
	Bibliography	121
	Curriculum Vitae	133

List of Abbreviations

AC	Alternating current (small-signal)
ACC	Adaptive cruise control
A / D	Analog-to-digital
ADS	Advanced Design System
A_E	Fabricated emitter area of transistor
Balun	Balanced-to-unbalanced converter
BEC	Base-emitter-collector (transistor geometry)
BV_{CBO}	Collector-base breakdown voltage at open emitter
BV_{CEO}	Collector-emitter Breakdown Voltage at open base
CCD	Charge-coupled device
CMOS	Complementary metal oxide semiconductor
CVD	Chemical vapor deposition
CW	Continuous wave
DC	Direct current
DSP	Digital signal processor
DSSS	Direct-sequence spread spectrum
DT	Deep trench
DUT	Device under test
ECC	Electronic communications committee
ENR	Excess noise ratio
EU	European union
F	Noise factor
FFT	Fast-Fourier transformation
FMCW	Frequency-modulated continuous-wave
FSCW	Frequency-stepped continuous-wave
G.P.S.	Global positioning system
GS	Ground-signal configuration
GSG	Ground-signal-ground configuration
HB	Harmonic balance
HBT	Heterojunction bipolar transistor
HF	High frequency
HS	High speed
HV	High voltage

IC	Integrated circuit
iCP _{1dB}	Input-referred 1 dB compression point
IF	Intermediate frequency
IP ₂	Second-order intermodulation point
IP ₃	Third-order intermodulation point
I/Q	In-phase / quadrature
ISO	Isolator / isolation
L	Code length (in DSSS systems)
LIDAR	Light detection and ranging
LNA	Low-noise amplifier
LO	Local oscillator
LRR	Long-range radar
LSB	Lower sideband
MIM	Metal-insulator-metal
MMW	Millimeter-wave
M _x	Layer of metal stack, $x = 1 \dots 4$
NF	Noise figure
NF _{DSB}	Double-sideband noise figure
NF _{SSB}	Single-sideband noise figure
NFM	Noise figure meter
PCB	Printed circuit board
PLL	Phase-locked loop
PN	Pseudo-noise
PRF	Pulse repetition frequency
USB	Upper sideband
RADAR	Radio detection and ranging
RCS	Radar cross section
RF	Radio frequency
RSS	Root sum of squares
RX	Receiver
SMA	Sub-miniature A
SNR	Signal-to-noise ratio
SOLT	Short-open-load-thru (calibration)
SRR	Short-range radar
STI	Shallow-trench isolation
TEM	Transmission electron microscope / Transversal electro-magnetic
TX	Transmitter
WHO	World health organization
VCO	Voltage-controlled oscillator
VSWR	Voltage standing wave ratio

List of Symbols

$\alpha_{\text{conductor}}$	Attenuation of a transmission line due to conductor losses
$\alpha_{\text{dielectric}}$	Attenuation of a transmission line due to dielectric losses
α_{F}	Ratio of collector and emitter current
α_{target}	Azimuth angle to target (driving direction = 90°)
α_{total}	Total attenuation of a transmission line
A_{e}	Effective antenna aperture
β	Current gain of transistor
β_0	DC current gain of transistor
B	Bandwidth
B	Stability measure
C'	Length-specific capacitance of a transmission line
c	Phase velocity
c_0	Speed of light in vacuum, $c_0 \approx 2.9979 \cdot 10^8 \frac{\text{m}}{\text{s}}$
C_{BC}	Base-collector oxide capacitance of transistor
C_{BE}	Base-emitter oxide capacitance of transistor
C_{CS}	Collector-substrate capacitance of transistor
C_{J}	Depletion capacitance
C_{μ}	Total base-collector capacitance of transistor
C_{pad}	Parasitic pad capacitance
C_{π}	Small-signal input capacitance of transistor
δ	Skin-depth
Δ	Determinant of the S -matrix
d	Distance between transmitter and target
Δd	Resolution of distance
d_{max}	Maximum covered distance by radar system
ε_0	Permittivity of vacuum, $\varepsilon_0 \approx 8.854 \cdot 10^{-12} \frac{\text{As}}{\text{Vm}}$
ε_{r}	Relative permittivity
ε_{eff}	Effective permittivity
f	Frequency
Δf	Smallest resolvable frequency
f_{b}	Beat frequency
f_{c}	Bandwidth occupied by one chip in a DSSS systems
f_{D}	Doppler frequency
f_{max}	Maximum oscillation frequency

f_{Pulse}	Bandwidth occupied by one pulse in pulse-Doppler radar systems
f_{T}	Transit frequency
f_{transmit}	Frequency of transmitted signal
f_{receive}	Frequency of received signal
G'	Length-specific conductance of a transmission line
Γ	Reflection coefficient
g_m	Small-signal transconductance of transistor
G_{av}	Available gain
G_{ISO}	Antenna gain with reference to an isotropic radiator
I_{C}	Collector current
\hat{I}_{C}	Peak absolute value of collector current
I_{C0}	DC component of collector current
i_{C}	AC component of collector current
\tilde{i}_{C}	Relative collector current swing
\hat{i}_{C}	Peak relative collector current
I_{CS}	Collector saturation current
I_{DC}	DC current
k_{B}	Boltzmann's constant, $k_{\text{B}} \approx 1.38 \cdot 10^{-23} \frac{\text{J}}{\text{K}}$
K	Rollet's K-factor
$K(\cdot)$	Complete elliptic integral of the first kind
λ	Wavelength
$\lambda_{\text{transmit}}$	Wavelength of transmitted signal
L'	Length-specific inductance of a transmission line
μ	μ factor (in context of stability)
μ_0	Permeability of vacuum, $\mu_0 = 4\pi \cdot 10^{-7} \frac{\text{Vs}}{\text{Am}}$
μ_r	Relative permeability
N	Number of samples
P_{LO}	Power level driving the LO
P_{N}	Noise power
P_{receive}	Power of received signal
P_{RF}	Power level at the RF port
P_{S}	Signal power
P_{transmit}	Power of transmitted signal
R'	Length-specific resistance of a transmission line
$\Re(\cdot)$	Real part
q	Charge of a single electron, $q \approx 1.602 \cdot 10^{-19} \text{ As}$
Q_x	nnp transistor x (in schematics)
R_{AC}	AC resistance
R'_{DC}	Length-specific DC resistance
r_b	Internal base series resistance of transistor
R_{B}	Total base series resistance of transistor (internal & external)
R_{C}	Total collector series resistance of transistor (internal & external)
R_{L}	Load resistance

r_{π}	Small-signal input resistance of transistor
R_S	Generator's source resistance
S_{ik}	Element ik of the S - matrix
σ	Radar cross section, RCS
σ_x	Conductivity of material x
$\bar{\sigma}$	Standard deviation
T, T_0	Temperature, $T_0 = 290$ K
τ_F	Forward transit time
ΔT	Smallest resolvable time span
T_{Block}	Block length
T_C	Chip length in DSSS systems
T_m	Duration of one sweep from f_{\min} to f_{\max} in FMCW system
T_{Pulse}	Duration of pulse in pulse-Doppler radar system
T_{sample}	Sampling period
v_p	Phase velocity
v_{rel}	Relative velocity
Δv_{rel}	Resolvable relative velocity
V_A	Forward Early voltage
V_{BC}	Base-Collector Voltage
V_{BE}	Base-Emitter Voltage
\hat{V}_{BE}	Peak absolute value of Base-Emitter Voltage
V_{BE0}	DC component of Base-Emitter Voltage
v_{BE}	AC component of Base-Emitter Voltage
V_{CC}	Positive supply voltage
V_{CE}	Collector-Emitter Voltage
V_{EE}	Negative supply voltage
V_{id}	Differential input voltage
V_{od}	Differential output voltage
V_T	Thermal voltage
ω	Angular frequency
Z_0	Characteristic impedance of a transmission line
Z_{IN}	Input impedance of transistor
Z_{OUT}	Output impedance of transistor

Chapter 1

Introduction

Road accidents cause a high number of injuries and fatalities worldwide. Statistics state that each year, 50 million people are injured and 1.2 million people are killed because of accidents involving motorized vehicles. Within the European Union (EU), 1.7 million are injured and 40.000 die annually [Strohm 05]. Hence, the EU reacted to these shocking high numbers and set the ambitious target to reduce road deaths by 50 % until the year 2010. A report from the World Health Organization (WHO) suggests that "a scientific, systems approach to road safety is essential to tackling the problem" [WHO 07]. This approach covers traffic as a whole, and interactions between vehicles, road users, and the road infrastructure are used to identify and solve traffic problems.

Road safety systems require monitoring of the actual traffic situation and advising the road users how to react to it. Active reaction by the vehicle alone, like autonomous emergency braking and steering, is a much more reliable solution than driver interaction, but legal issues prevent its implementation. In addition, system malfunction can lead to dangerous situations.

Substantial progress in preventing accidents is achieved by reducing the time span from the recognition of the situation to the vehicle's reaction. Figure 1.1 shows typical probabilities of different kinds of accidents versus a shift-forward of the driver reaction time. Lowering the reaction time by 0.25 s results in a decrease of collision probability in case of rear-end collisions by 30 %, for example. Collisions at intersections, e.g., can be avoided in 50 % of all cases if the driver knows about the situation 0.5 s in advance. If an accident cannot be avoided, the information about the location and the severity of the impact lets the vehicle prepare safety features such that the risk of injuries is minimized. For example, the detection of an unavoidable side impact gives enough time to inflate airbags.

Hence, the key to increase road safety is scanning and mapping the vehicle's environment. On-board equipment is the first choice, since it is easiest to implement. It informs the driver in advance about probable hazardous situations. Next steps include car-to-car communication and car-to-infrastructure communication. An

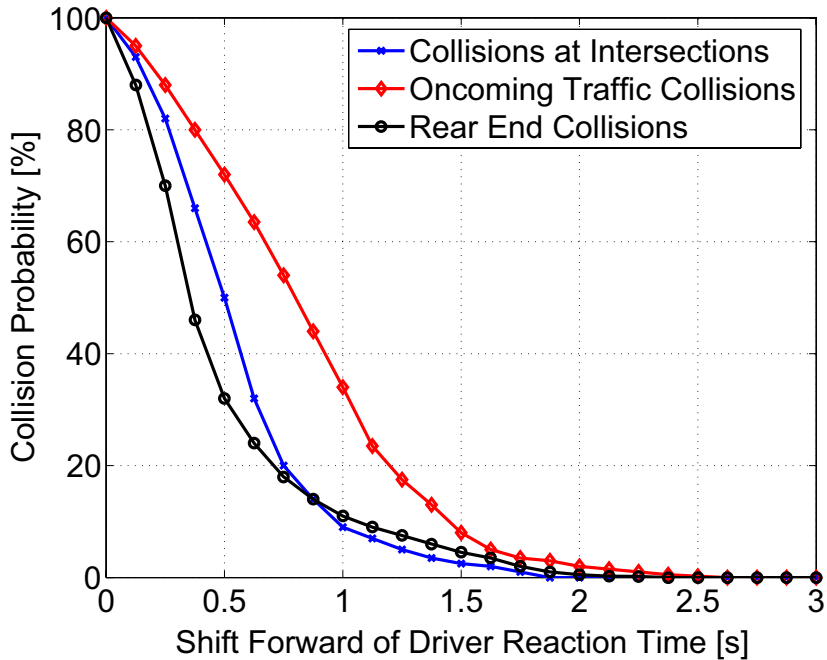


FIGURE 1.1: Probability of different crash scenarios versus driver reaction time [Gresham 04].

implementation of these features gives the ultimate protection of all road users without the need to establish new laws.

An additional benefit of equipping vehicles with systems that scan the environment is the simultaneous implementation of comfort features. The well-known cruise control can be extended to a version that brakes and accelerates the car on its own, depending on the traffic situation. The braking process does not suffer from legal issues in cruise control applications since the deceleration is much slower than in case of an emergency braking [Audi AG 07, BMW AG 07, DaimlerChrys 07, Lexus 07].

Today's safety and comfort features in the automotive environment are depicted in figure 1.2. These features are coarsely distinguished by the covered ranges: Short-range systems monitor the surroundings in the vicinity of the car up to 30m. Long-range systems scan distances up to 200m in front of or at the rear end of the car. Table 1.1 lists safety and comfort features and the way they are implemented today. Different technologies are used. These include CCD/CMOS cameras, infrared sensors, ultrasonic sensors, lidar (light detection and ranging), and radar (radio detection and ranging). The variety of sensors makes the implementation of several safety features expensive. This is contradictory to the target of improving road safety. An improvement can only be achieved if safety systems are offered at affordable prices so that they are standard equipment even in low-budget cars. Therefore, the goal is to provide systems that consist of as

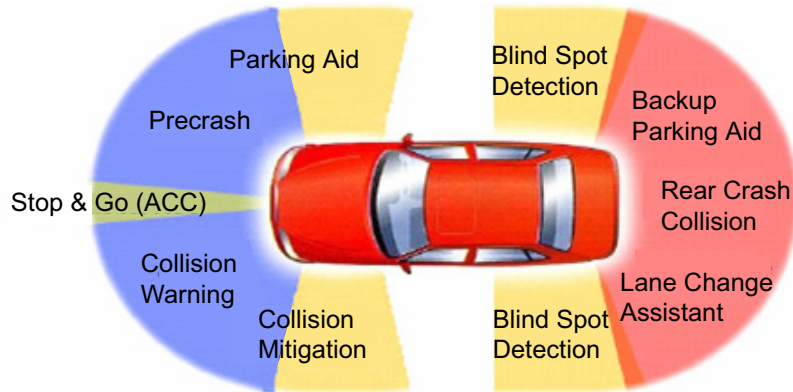


FIGURE 1.2: Safety and comfort features in the automotive environment [Strohm 05].

TABLE 1.1: Automotive safety and comfort features and today's implementation.

Function	Implementation
Pedestrian Detection	CCD/CMOS Camera, SRR
Blind Spot Surveillance / Lane Change Assistant	CCD/CMOS Camera, SRR
Lane Departure Warning System	Active Infrared ¹
Emergency Braking Assistant	LIDAR, LRR, SRR
Rear-view Applications	CCD/CMOS Camera, Ultrasonic, SRR
Occupant Detection and Assessment	Ultrasonic, Computer Vision
Automatic Cruise Control	LIDAR, LRR, SRR
Night Vision	Passive Infrared Camera, LRR
<i>Autonomous Driving</i>	LRR, SRR, Infrared/CCD/CMOS Camera

few components as feasible, but at the same time cover as many safety features as possible.

Automotive radar systems for short-range and long-range applications are ideal candidates for the simultaneous integration of different safety and comfort features. As shown in table 1.1, short-range radar systems (SRR) can take over the functionality of many different sensors. Long-range automotive radar (LRR) serves the same range of functions as LIDAR systems, but has the advantage of being less susceptible to weather conditions. Another advantage of SRR and LRR is the option to hide these devices behind the car's bumpers.

Long-range automotive radar systems were introduced to the market in 1998. These systems scan a narrow beam (2° to 3°) over an azimuth variation of 5° to 8° , covering distances up to 200m in front of or behind the car. LRR systems

¹Active infrared systems irradiate infrared light vertically onto the street and use the reflections to scan for road markings [Citröen 07].

operate in the frequency range from 76 to 77 GHz. These millimeter-wave frequencies offer the realization of a narrow beamwidth without the need for large antennas. Today's LRR systems are fabricated in III-V semiconductor technologies that are more cost intensive and do not offer the possibility of high-level integration. Silicon-Germanium (SiGe) bipolar technology excels these technologies by offering a high integration level and low production cost at the same time. Recent advancements in SiGe bipolar technology allow the implementation of radar components operating in the millimeter-wave range. Even higher integration levels can be achieved by fabricating the entire transceiver, including baseband, in CMOS. Recent publications report on the first building blocks in 65 nm CMOS, like a 90 GHz injection-locked frequency divider [Mayr 07].

Short-range automotive radar applications operate at a center frequency larger than 24.075 GHz with a bandwidth of at most 7 GHz. The allocated frequency band ranges from 22 to 29 GHz [FCC 02]. Systems operating at this frequency are commonly named 24 GHz systems. Due to interference with frequency bands used by radio astronomers [ERC 07, NTIA 07], limitations are imposed on the use of 24 GHz short-range radar systems worldwide. These limitations are, for example, that the penetration of vehicles with SRR systems must not exceed 7%, and that the systems must be switched off in the vicinity of radio astronomy sites either automatically (using G.P.S.[©] or Galileo[©]) or by hand. In addition, these systems must not be placed on the market after 2012.

An implementation of an SRR system in SiGe is presented in [Gresham 04]. The biggest competitor of SiGe in the 24 GHz SRR market is CMOS. In [Fujushima 06], a 22–29 GHz pulse generator in 90 nm CMOS is presented. A 24 GHz phased-array transceiver in 130 nm CMOS is reported in [Krishnaswamy 07].

One solution to overcome the SRR problem of interference is moving to another frequency band. The frequency band from 77 to 81 GHz does not have this limitation. Another advantage moving to higher frequencies is the associated shrink of the antenna and, hence, module size.

Aside from sensing, the frequencies above 70 GHz are attractive for data communication applications because of the large available bandwidths. Additionally, the narrow beam widths associated with the high operational frequencies offer the implementation of multiple point-to-point data communication systems that do not suffer from interference. A recent ECC recommendation suggests to approve the frequency bands from 71 to 76 GHz and from 81 to 86 GHz for very high-speed data communication [WGSE 05].

The presented thesis is organized as follows:

Automotive radar systems are implemented in different ways. An overview about the functionality of different concepts is presented in chapter 2.

The circuits presented in this work are designed and implemented in Infineon's SiGe:C bipolar technology. The components used within the circuits are outlined

in chapter 3. Resistors, capacitors, and transmission lines are treated in detail since the high operational frequencies of the circuits require thorough analyses of passive elements.

A down-conversion mixer that was developed for use in a low-cost long-range automotive radar system is elaborated in chapter 4. The circuit is analyzed in great detail in terms of noise, linearity, and stability. Excellent measurement results proof the successful design.

Chapter 5 presents a complete receiver front-end that shows a high level of integration of high-frequency components. The measurement results reveal that this IC outperforms published state-of-the-art millimeter-wave receivers.

Finally, chapter 6 summarizes the main achievements of this work, and an outlook for future systems and circuit implementations is given.

Chapter 2

Radar Systems

The implementation of safety and comfort features in the automotive environment requires exact knowledge about the surroundings of the car. This information is provided by high-frequency radar systems. Radar is superior to other technologies since it is de facto immune to weather conditions.

Automotive radar systems can be classified with respect to the covered area. Short-range radars (SRR) are used to scan 360° of the car's surrounding up to distances of 30 m. These sensors are used for blind-spot surveillance, lane-change assistants, or rear-view applications, for example. Long-range radars (LRR) map the environment located far ahead of the car. Maximum ranges are 200 m, and the angular coverage is at most 4° to the left and the right of the driving direction.

The basic functionality common to all presented radar systems is described in section 2.1. This covers the radar range equation that gives the received power depending on the target and the channel, and techniques that are used to get angular resolution. The measurement of the distance to and the relative velocity of the target is done depending on the specific implementation. The most prominent implementations are frequency-modulated continuous-wave (FMCW) systems for LRR and pulse-Doppler radar systems for SRR. They are introduced in sections 2.2 and 2.3, respectively. Another implementation of a radar system that uses spread-spectrum techniques is discussed in section 2.4.

2.1 General Aspects

Automotive radar systems transmit high-frequency signals and use the reflected echoes to determine the exact location and velocity of targets. The distance to targets and their relative angle to the driving direction (the azimuth) are measured to precisely determine the targets' location. The respective relative velocities are determined by measurement of Doppler-frequency shifts. Multiple targets must be resolved simultaneously.

Depending on the location of the transmit and the receive antenna, radar systems are classified monostatic or bistatic. The transmit and the receive antenna are at the same location in a monostatic radar system. The transmitter and the receiver do not necessarily share the antenna, but the distance between the antennas must be negligible compared with the covered range. When the distance between the transmit and the receive antennas cannot be neglected, the radar system is bistatic. Only monostatic solutions are used for automotive radars.

A target can be detected only if the received signal power is above a certain power level. This level is determined by the high-frequency transmit and receive front-ends and the baseband processing. Since the baseband processing is a well-protected secret of all manufacturers, no general expression for the required minimum power level can be stated. For a specific system and channel, the power level of the received signal is derived using the radar range equation.

Radar Range Equation

The radar range equation yields the received signal power after the transmitted power is scattered from a target. This scenario is depicted in figure 2.1. The re-

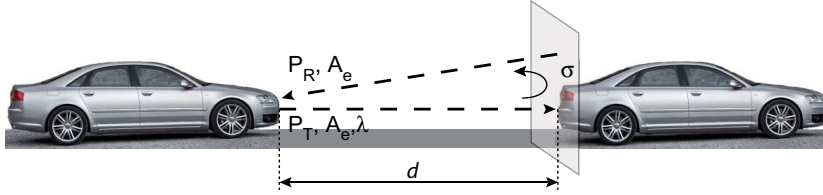


FIGURE 2.1: Illustration of the radar range equation in an automotive environment.

ceived signal power for a monostatic radar system is given by [Royal School 04,a]

$$P_{\text{receive}} = \frac{P_{\text{transmit}} A_e^2 \sigma}{4\pi d^4 \lambda^2}. \quad (2.1)$$

The power of the transmitted radar signal is P_{transmit} . The distance between the antenna of the radar system and the target is given by d . The radar cross section (RCS) σ of the target is defined as the equivalent area that intercepts the radiated electromagnetic power and scatters it isotropically such as to produce the same power at the receiver as the real target. The RCS is dependent on the wavelength λ , the angle of the incident and the reflected waves, and material properties. Variable A_e is the effective antenna aperture¹. It is linked to the antenna gain via

$$G_{\text{ISO}} = \frac{4\pi A_e}{\lambda^2}, \quad (2.2)$$

¹For a bistatic radar system, A_e^2 must be replaced by the product of the effective antenna apertures of the transmit and the receive antenna, $A_{e,\text{transmit}} A_{e,\text{receive}}$. The range d^4 must also be substituted by $d_1^2 d_2^2$, where d_1 and d_2 are the distances from the transmitter and the receiver to the target.

where G_{ISO} is the relative antenna gain with reference to an isotropic radiator.

Equation (2.1) shows that the received signal power increases with increasing antenna gain and radar cross section, and decreases with increasing distance and wavelength. For a real 77 GHz automotive radar system, the power of the transmitted signal can reach levels up to +16 dBm [Li 04]. An RCS of 10 dBsm (area referred to 1 square meter) at 77 GHz is assumed as a realistic target [Hall 02]. The radar system is supposed to identify targets up to 200 m. Publications report on antenna gains of 27 dBi [Grubert 03] and 30 dBi [Kolak 01] at 77 GHz, which is equivalent to effective antenna apertures of 6.05 cm² and 12.08 cm², respectively. Taking the higher value of the two antenna apertures, the received power will be -87 dBm in case of no atmospheric losses. The received signal is then down-converted by a mixer for further processing. The signal-to-noise ratio (SNR) is additionally deteriorated by the noise figure of the mixer.

Angle Measurement

The angular measurement capability of a radar system can be implemented either by steering the antenna mechanically or using an antenna array. These antenna configurations are independent of the architecture of the radar, i.e., whether it is a CW or a pulsed radar.

Mechanical steering has the advantage of simplicity in baseband processing since the angle of the target is known directly from the angle of the antenna. The antenna is set to a certain azimuth α_{target} and the signal is transmitted. The received signal is collected at the same azimuth. The antenna is then set to a different angle, and the procedure is repeated. If a range of e.g. 200 m must be covered, which is typical for an automotive long-range radar system, the antenna must remain at the same position for transmitting and receiving for at least 1.33 μs . The drawback of the mechanical solution is the sensitivity to environmental impacts, like humidity or variations in temperature, that require a robust thus expensive antenna design.

Using antenna arrays for the determination of the angle is more robust to environmental impacts than mechanically steered antennas. In addition, this solution offers the possibility for on-chip integration. In receive mode information about the angle of incidence is extracted from the phase difference of the received signals, see figure 2.2. Arrays that consist of antennas with equal antenna gain and equal spacing d between the elements have a phase delay $\Delta\varphi$ between the received signals of

$$\Delta\varphi = d \sin(\alpha_{\text{target}}) \frac{360^\circ}{\lambda}. \quad (2.3)$$

Rearranging this equation gives the angle of the transmitted wave α_{target} in dependence of the phase difference $\Delta\varphi$. An implementation of a receiver front-end with four on-chip antennas is presented in [Babkhani 06].

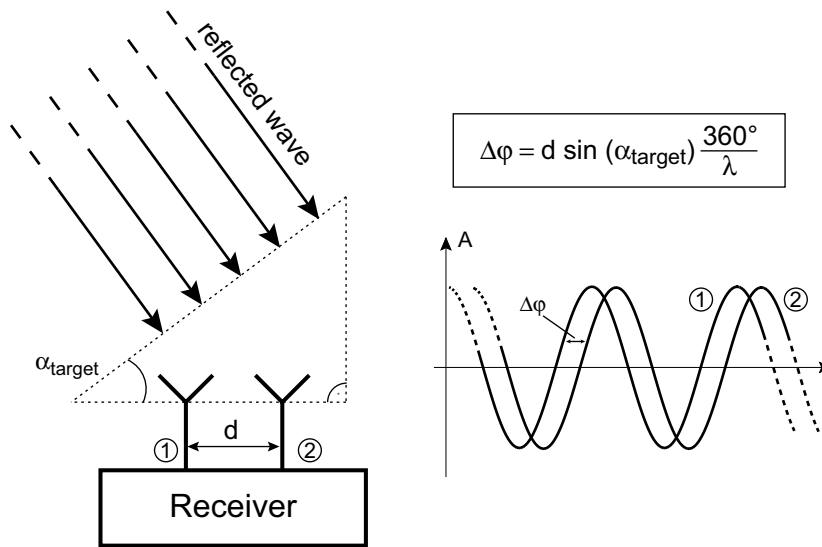


FIGURE 2.2: Working principle of an antenna array in receive mode. In transmit mode, the phase difference $\Delta\varphi$ determines the angle α_{target} .

In transmit mode antenna arrays have the ability to use the phase difference $\Delta\varphi$ of the driving signals to steer the antenna beam. This feature is not implemented in today's long-range automotive radar systems since the required azimuth coverage is already obtained from multiple antennas on the receive side. Beam steering increases the covered area and will be useful in next-generation radar systems. A transmitter with four on-chip antennas and the possibility to adjust the beam electrically is presented in [Natarajan 06].

The increased robustness of antenna arrays comes at the cost of increased base-band processing, which requires a powerful digital signal processor (DSP). Antenna arrays for long-range automotive radar are commercially available, e.g. [Electronic 07].

2.2 Frequency-Modulated Continuous-Wave Radar

Frequency-modulated continuous-wave (FMCW) radar systems simultaneously determine the relative velocity of a target and the distance to a target. This is done by varying the frequency of a continuous-wave (CW) radar system in time.

A classic CW radar system uses a fixed transmit frequency. The HF signals are transmitted and received without interruption. This system can only measure Doppler shifts, but not the distance to a target. Therefore, it is not of interest for automotive radar applications. Varying the frequency of the carrier in time solves this problem since the frequency difference between the received signal and the transmitted signal can be mapped directly to an unambiguous distance. The frequency can be changed by a (linear or nonlinear) sweep (frequency-modulated

continuous-wave, FMCW) or in discrete steps (frequency-stepped continuous-wave, FSCW). The latter will not be treated further since it does not have advantages over FMCW in an automotive environment.

An implementation of a homodyne FMCW radar system is depicted in figure 2.3. The local oscillator (LO) generates the transmit signal. A coupler feeds this signal

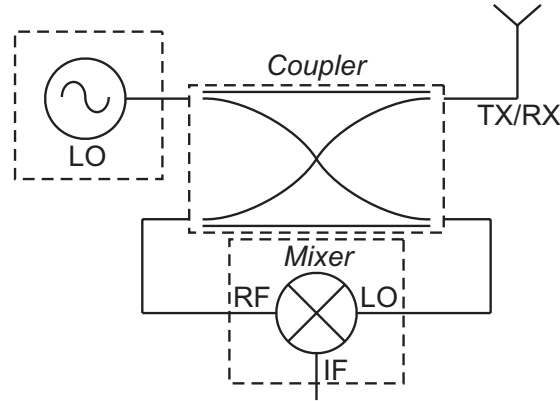


FIGURE 2.3: Implementation of a single-antenna FMCW radar system consisting of a local oscillator (LO), a coupler, one antenna, and a homodyne down-conversion mixer.

to the antenna. Part of the signal is used as the LO for the down-conversion mixer. The LO signal can be split to feed several coupler/mixer/antenna sections for the ability to detect angles. In the receive case, the signal that is backscattered from the target gets to the RF port of the mixer through the coupler. Part of the RF signal is lost in the output of the LO. The RF signal is down-converted to the intermediate frequency (IF), where it is sampled, digitized, and further processed by Fast Fourier Transformation (FFT) methods to calculate the relative velocity of the target.

The coupler in figure 2.3 can be implemented as a rat-race coupler, for example [Pozar 01]. This topology is depicted in figure 2.4. The signal is fed into port number one (P1) and split into equal parts to the ports numbered two (P2) and three (P3), which are 180° out of phase. Port number four (P4) is isolated. One drawback of this coupler is the occupied chip area (e.g., $\lambda/4 = 493 \mu\text{m}$ at 77 GHz in SiO_2 , yielding a total length of 2.96 mm). Another disadvantage arises from the losses of the transmission lines: Path $1 \rightarrow 2$ is $\lambda/2$ longer than path $1 \rightarrow 3$, so the amplitude difference is 0.5 dB due to transmission line losses only (see chapter 3.4). The same considerations apply for the isolation of P4 from P1: Going from P1 clockwise to P4 is $\lambda/2$ longer than going counter-clockwise, which results in an amplitude difference. Thus the incident waves do not cancel perfectly. The maximum achievable isolation is therefore given by

$$\text{ISO} = -20 \log_{10}(A_1 - A_2) \text{ dB}, \quad (2.4)$$

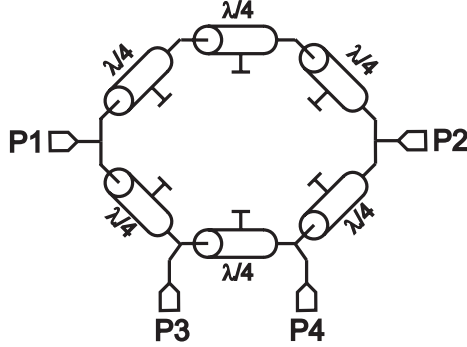


FIGURE 2.4: Rat-race coupler. $Z_0 = 70.7 \Omega$

where $A_{1,2}$ are the amplitudes of the interfering waves. An amplitude difference of 5.6 %, which is equal to 0.5 dB on a logarithmic dB scale, results in a maximum isolation of 25 dB. Taking a peak output power of +16 dBm for the VCO [Li 04], the unwanted LO signal at the RF port of the mixer has a power level of -9 dBm, neglecting parasitic coupling. In addition, LO power that is reflected from the antenna enters directly into the RF port. Therefore, the down-conversion mixer must exhibit high linearity. The design of such a mixer is elaborated in chapter 4.

FMCW Radar Functionality

The functionality of FMCW radar is explained using figure 2.5. The transmit signal changes its frequency periodically according to

$$f_{\text{transmit}} = f_{\text{min}} + \frac{(f_{\text{max}} - f_{\text{min}})}{T_m/2} t \quad \text{for } 0 \leq t < T_m/2, \quad (2.5)$$

$$f_{\text{transmit}} = f_{\text{max}} - \frac{(f_{\text{max}} - f_{\text{min}})}{T_m/2} (t - T_m/2) \quad \text{for } T_m/2 \leq t < T_m, \quad (2.6)$$

where T_m is the period. The minimum and maximum transmit frequencies are f_{min} and f_{max} , respectively. The duration of one sweep from f_{min} to f_{max} (equivalently from f_{max} to f_{min}) is termed the block length $T_{\text{Block}} = T_m/2$. The transmit signal is the red trace in figure 2.5. The transmit signal propagates to the target and returns to the radar system after backscattering, resulting in the blue signal in figure 2.5. Since the frequency at the transmitter has changed in the meantime, the received frequency deviates from the transmitted frequency by the beat frequency f_b . Its absolute value is

$$f_b = \frac{f_{\text{max}} - f_{\text{min}}}{T_{\text{Block}}} \cdot \frac{2d}{c}. \quad (2.7)$$

The propagation delay of the received signal is $\frac{2d}{c}$ with d being the distance between the radar system and the target. The speed of the propagating signal is

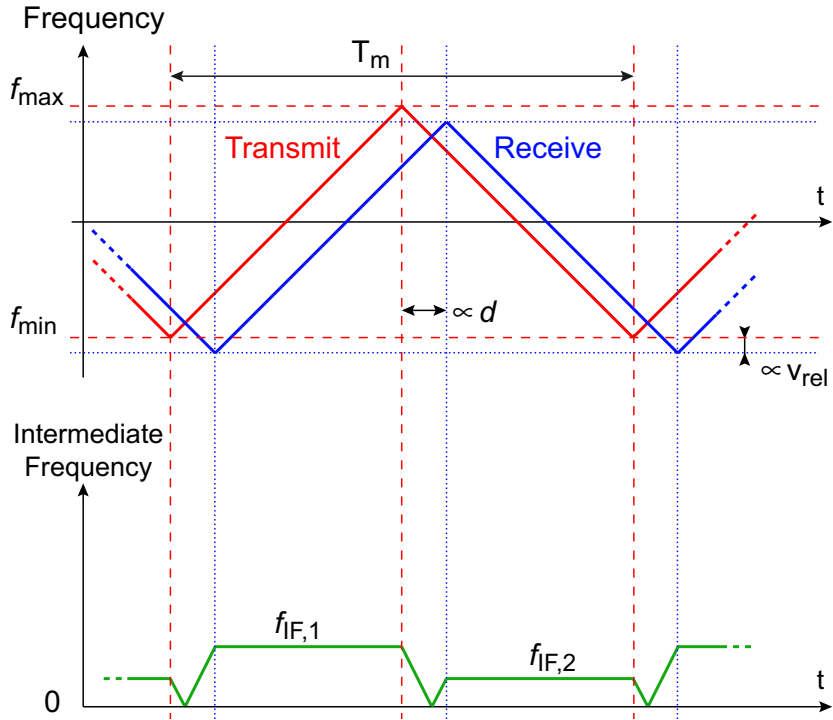


FIGURE 2.5: Range and relative velocity detection using a swept frequency FMCW radar. This figure depicts the scenario where the receding target is located at distance d from the radar transceiver.

c . It is approximately equal to the speed of light in vacuum, $c_0 = 2.998 \cdot 10^8$ m/s. Targets with zero relative velocity to the transmitter result in no frequency shift of the received signal, corresponding to no shift of the blue curve in vertical direction in figure 2.5. The down-converted echoes then result in constant intermediate frequencies. This is only the case if the slope of the frequency sweep is constant, which is a stringent requirement on the VCO and the phase-locked loop (PLL).

Information about the target is therefore contained in the intermediate frequency. Hence, also frequency components that arise from non-ideal system components are treated as targets ("ghost targets"). The third-order nonlinearities of the down-conversion mixer, for example, cause ghost targets at twice the IF. These frequency components can be identified by using different slopes for the frequency sweep. The impact of nonlinearities is also reduced when highly linear components are employed. A highly-linear down-conversion mixer is presented in chapter 4.

If the relative velocity between the radar transceiver and the target is non-zero, the backscattered frequency changes according to

$$f_D = -\frac{2v_{\text{rel}}f_{\text{transmit}}}{c} = -\frac{2v_{\text{rel}}}{\lambda_{\text{transmit}}}. \quad (2.8)$$

The frequency shift f_D is the Doppler frequency. In this equation, $f_{\text{transmit}} = c/\lambda_{\text{transmit}}$ is the frequency of the transmitted signal. The relative velocity of

the target is v_{rel} . It is determined by $v_{\text{rel}} = v_{\text{target}} \sin \alpha_{\text{target}}$ with the target's absolute velocity v_{target} and azimuth angle α_{target} (the driving direction equals $\alpha_{\text{target}} = 90^\circ$). The relative velocity v_{rel} is positive for receding and negative for approaching targets. The Doppler effect is illustrated in figure 2.6.

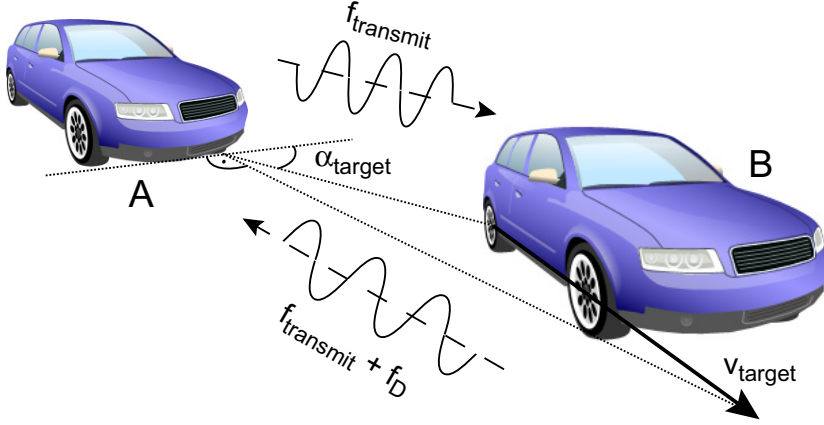


FIGURE 2.6: Illustration of the Doppler effect. This scenario represents a receding target, $v_{\text{target}} > 0$.

The smallest resolvable frequency Δf is determined by the sampling frequency f_{sample} of the analog-to-digital converter (ADC) and the observation time. The observation time is usually chosen such as to be equal to the block length T_{Block} [Mende 99]. The sampling frequency f_{sample} is set to fulfill $T_{\text{Block}} = NT_{\text{sample}}$, where $T_{\text{sample}} = 1/f_{\text{sample}}$ is the sampling period and N the number of samples in one observation period. These settings result in the general expressions

$$\Delta T = NT_{\text{sample}} = T_{\text{Block}} \quad \leftrightarrow \quad \Delta f = \frac{f_{\text{sample}}}{N} = \frac{1}{T_{\text{Block}}} \quad (2.9)$$

for the smallest resolvable time span ΔT and the largest resolvable frequency Δf , respectively.

Equation (2.9) directly determines the resolvable relative velocity, Δv_{rel} from equation (2.8),

$$\Delta v_{\text{rel}} = \frac{\lambda_{\text{transmit}} \Delta f_D}{2} = \frac{\lambda_{\text{transmit}}}{2} \frac{1}{T_{\text{Block}}}. \quad (2.10)$$

This equation shows that a large block length T_{Block} results in a good resolution of the Doppler frequency shift.

Rearranging equation (2.7) yields an expression for the resolution of the distance,

$$\Delta d = \frac{c}{2(f_{\text{max}} - f_{\text{min}})} \Delta f_b T_{\text{Block}}, \quad (2.11)$$

where Δf_b represents the change in beat frequency. Since the product $\Delta f_b T_{\text{Block}}$ is equal to "1", refer to equation (2.9), this equation simplifies to

$$\Delta d = \frac{c}{2(f_{\text{max}} - f_{\text{min}})}. \quad (2.12)$$

A large difference between the maximum and the minimum frequency of the FMCW signal therefore results in a high resolution of the distance.

The maximum unambiguous range is derived from equation (2.7) by insertion of the maximum detectable frequency $f_{b,\text{max}}$ that is set by the used baseband components,

$$d_{\text{max}} = \frac{f_{b,\text{max}} c T_{\text{Block}}}{2(f_{\text{max}} - f_{\text{min}})}. \quad (2.13)$$

If the frequency difference is set according to equation (2.12), $f_{b,\text{max}}$ and T_{Block} are the only degrees of freedom left. The maximum detectable frequency $f_{b,\text{max}}$ depends on the used hardware, i.e., the ADC. Since T_{Block} is also set according to equation (2.10), a trade-off must be found to achieve the required performance.

The frequency difference associated with the distance between the radar system and the target adds to the frequency shift due to the Doppler effect. Referring to figure 2.5, the absolute values of the received frequencies after down-conversion to baseband (intermediate frequency, IF) are

$$f_{\text{IF},1} = f_b + f_D \quad (2.14)$$

and

$$f_{\text{IF},2} = f_b - f_D. \quad (2.15)$$

The combination of these two frequencies yields the distance to and the relative velocity of the target,

$$\frac{f_{\text{IF},1} - f_{\text{IF},2}}{2} = f_b \quad \rightarrow \quad d = \frac{c T_{\text{Block}} (f_{\text{IF},1} - f_{\text{IF},2})}{4(f_{\text{max}} - f_{\text{min}})}, \quad (2.16)$$

$$\frac{f_{\text{IF},1} + f_{\text{IF},2}}{2} = f_D \quad \rightarrow \quad v_{\text{rel}} = -\frac{c(f_{\text{IF},1} + f_{\text{IF},2})}{4f_{\text{transmit}}}. \quad (2.17)$$

2.3 Pulse-Doppler Radar

Pulse-Doppler radar systems use the time and the frequency domain to determine the distance to and the relative velocity of targets. The functionality of a pulse-Doppler radar system is explained using figure 2.7. The receiver is turned off while transmitting. The duty cycle of pulse-Doppler radars is typically a few percent, resulting in the transceiver spending more time listening to echoes than transmitting signals. This results in a low average transmit power ($P_{\text{transmit}} \times \text{duty cycle}$) for pulsed radar systems.

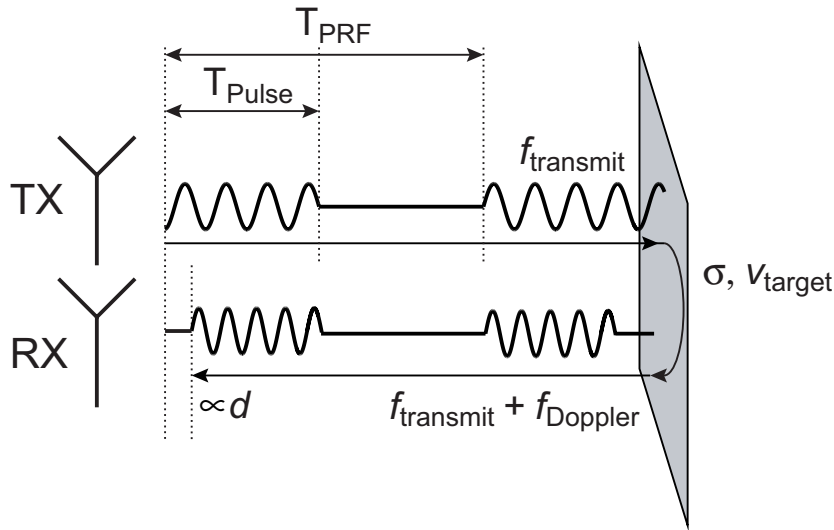


FIGURE 2.7: Pulse-Doppler Radar functionality: The transmitter sends pulses of width T_{Pulse} and frequency f_{transmit} every $T_{\text{PRF}} = 1/\text{PRF}$ seconds. The moving targets with RCS σ and relative velocity v_{target} reflect the signal and change the frequency.

Determination of the distance is done by transmitting high-frequency signals with a pulse-shaped envelope. The time span between transmission of the pulses and reception of echoes is measured. This time span is proportional to the target's distance. The rate at which pulses are sent is the pulse repetition frequency, PRF. Low PRFs result in large unambiguous ranges. The unambiguous range is defined as the distance at which targets can be uniquely identified. For example, an object located beyond the unambiguous range causes echoes that are indistinguishable from echoes of objects within the unambiguous range.

The resolution of the radar system is defined as Δd , given by

$$\Delta d = \frac{c}{2\Delta f_{\text{Pulse}}}. \quad (2.18)$$

The bandwidth occupied by a pulse is Δf_{Pulse} . For constant transmit frequencies and rectangular pulses, approximately 90% of the signal power is located within a bandwidth of $\Delta f_{\text{Pulse}} = 1/T_{\text{Pulse}}$. Thus, the pulse width must be low for high resolution.

The frequencies contained in one short pulse cannot be used to accurately measure the Doppler frequency shift [Royal School 04,b]. The Doppler frequency, equation (2.8), is on the order of a few kilohertz in an automotive environment, corresponding to a time period $1/f_D$ of hundreds of microseconds. The duration of one pulse is on the order of a few microseconds, thus the time interval of one pulse is only a fraction of the Doppler time period. The information about the relative velocity of the target can only be extracted if the duration of one pulse

is increased or if more than one pulse is analyzed. Increasing the pulse width decreases the resolution, therefore, the PRF must be chosen high enough to collect the information contained in many pulses and extract the Doppler frequency.

The dilemma of small pulse widths for high resolution and large pulse widths for accurate Doppler frequency determination is resolved using pulse-compression techniques. Radar systems employing pulse compression modulate the frequency of the transmit pulses, thereby increasing Δf_{Pulse} . This reduces Δd in equation (2.18) [Barton 98].

The received signal arrives with an arbitrary phase angle with reference to the LO. These signals can be out-of-phase such that coherent detection results in zero output. No information about the target's relative velocity can therefore be extracted [Royal School 04,b]. A second branch in the receive chain that is shifted in phase by 90° yields the desired information in that case. The combination of both in-phase (0° , I) and quadrature (90° , Q) components using $\sqrt{S_I^2 + S_Q^2}$ results in no loss of information. The front-end presented in chapter 5 addresses the implementation of an I/Q receiver.

Pulse-Doppler radar systems are used mainly for short-range automotive radar (SRR) applications, that is, up to a maximum detection range of 30 m. The use of a constant transmit frequency results in a simple and cheap transmitter, since the frequency must be held constant only. Knowledge of the absolute frequency is not necessary. Due to the simplicity and the low duty cycle, the power consumption is less than in FMCW systems. Since SRR applications necessitate up to 16 sensors for complete coverage around the car, the power consumption is of great concern. Additionally, requirements on the large-signal properties of the receiver are relaxed since the transmitter and the receiver are not "on" at the same time.

The frequency band allocated to SRR ranges from 22 to 29 GHz, with a center frequency larger than 24.075 GHz [FCC 02]. Interference with other applications in this frequency range, like radio astronomy, force the use of other frequencies. For example, the frequency band from 77 to 81 GHz is allocated to future SRR implementations. A 24 GHz pulse-Doppler radar demonstrator for automotive applications is reported in [Gresham 01].

2.4 Direct-Sequence Spread-Spectrum Radar

The drawback of both FMCW and pulsed radar systems is their susceptibility to interference. It is impossible to distinguish whether the received signal originated from the own transmitter or from the transmitter of another system. This increases the probability of erroneous detections.

Modulating the transmit signal with a pseudo-noise (PN) code marks the transmitted signal with a unique tag, making it immune to interferers and improving its

performance regarding multipath propagation. In addition, the increased bandwidth of the signal results in good resolution in distance measurement, similar to equation (2.18). This technique is called direct-sequence spread-spectrum (DSSS). Circuit implementations for the receiver and the transmitter of a 79 GHz DSSS system will be presented in [Trotta 07,a].

The functionality of a spread-spectrum radar system is explained in figure 2.8. The biphas modulator toggles the phase of the transmitted signal between 0°

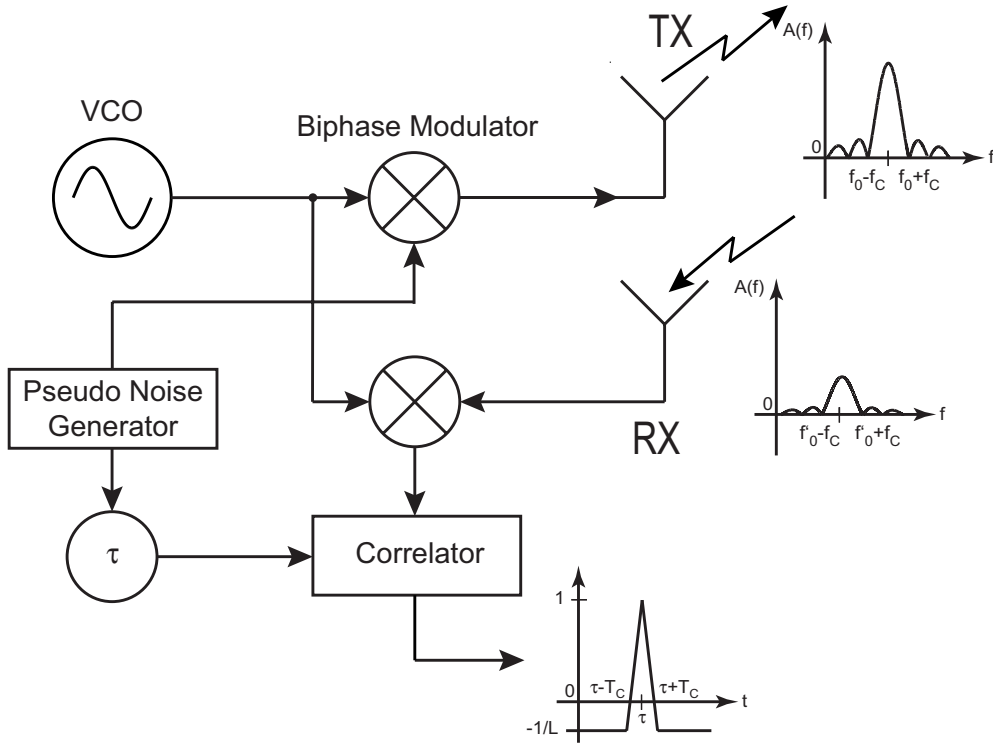


FIGURE 2.8: Simplified functionality of a spread-spectrum radar system.

and 180° according to the PN sequence. Each chip of the sequence has a length of T_C . Roughly 90% of its power is concentrated in a bandwidth of $f_C = 1/T_C$. The power spectral density of the transmit signal is shown on the right hand side of the transmit antenna (TX). The received signal is an attenuated version of the transmitted one. The absolute frequency can also be shifted due to the Doppler effect. The received signal is down-converted and subsequently correlated with a time-delayed version of the PN sequence. The output of the correlator is the correlation function shown at the bottom of figure 2.8. The distance to the target is extracted from the peak in the correlation function and the related time delay τ . The magnitude of the peak is equal to "one" for correlation and $-1/L$ if the sequences are not correlated. The variable L is the code length.

The delayed reference and the incoming signal are incoherent, therefore the correlation can yield zero output. For that case, the correlation with both I and Q ver-

sions of the received signal are needed [Filimon 00]. The receiver front-end elaborated in chapter 5 features in-phase and quadrature low-noise down-conversion of the received signal.

The deviation of the received center frequency from the transmitted one gives directly the Doppler frequency and, hence, the relative velocity.

The disadvantage of direct-sequence spread-spectrum systems is the complexity in transmit path, receive path, and baseband. The PN sequence must be generated, stored, and shifted in time. The determination of the relative velocity from the measured Doppler frequency shift requires additional efforts since the intermediate frequency will be close to zero.

A spread-spectrum transmitter for 79 GHz SRR is presented in [Trotta 07,b]. This transmitter features on-chip PN-code generation.

Chapter 3

Infineon's SiGe:C Bipolar Technology

The circuits presented in this work are designed and implemented in Infineon's SiGe:C bipolar technology [Böck 04]. This chapter outlines the used components.

Details about the vertical npn transistors are given in section 3.1. This section also covers the electric model of the transistor that is provided by Infineon's designkit. The technology additionally offers vertical pnp devices which are not treated since they were not used in the designs.

Passive components include different types of resistors and metal-insulator-metal (MIM) capacitors. They are introduced in section 3.2 and section 3.3, respectively.

Transmission lines are essential components of the circuits presented in chapters 4 and 5. Section 3.4 is therefore dedicated to the implementation and modeling of these elements.

3.1 High-Speed NPN Bipolar Transistor

Infineon's SiGe:C technology offers different kinds of transistors. These are high speed (HS) and high voltage (HV) transistors, of which only the HS transistor is implemented in the presented circuits. The main differences in transistor types are in transit frequency f_T , maximum oscillation frequency f_{max} , and breakdown voltage. For each of the transistor types, a wide range of emitter dimensions is provided which allows to choose emitter areas such as to operate the transistor at optimum current density. A summary of typical performance parameters of available transistor types is given in table 3.1. The parameter A_E gives the fabricated emitter area of the characterized device, BV_{CEO} is the collector-emitter breakdown voltage at open base, and BV_{CBO} is the collector-base breakdown voltage at open emitter. The DC current gain is β_0 . The frequencies f_T and f_{max} are the transit frequency and the maximum oscillation frequency at optimum

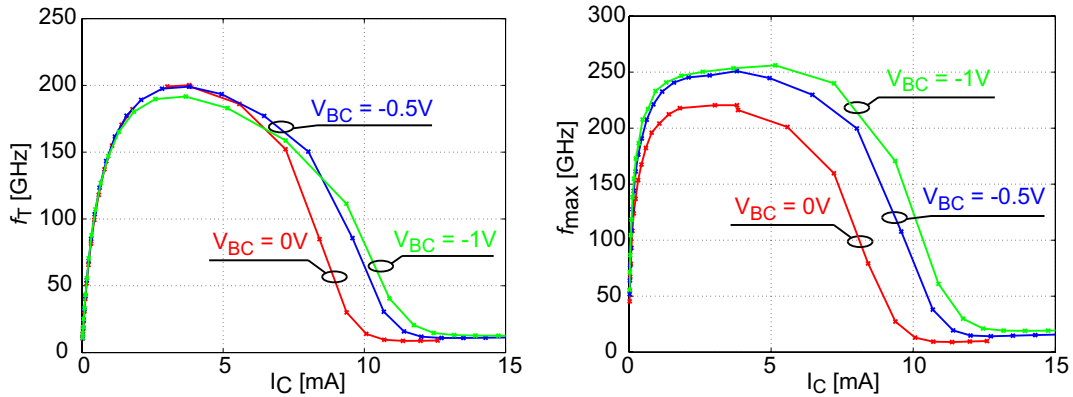
TABLE 3.1: Transistor types of Infineon’s SiGe:C technology and their measured performance [Infineon 05, Vytla 06].

	HS ¹	HV
A_E	$0.18 \times 2.6 \mu\text{m}^2$	$0.14 \times 2.6 \mu\text{m}^2$
f_T	200 GHz	52 GHz
f_{max}	256 GHz	174 GHz
β_0	320	300
BV_{CEO}	1.7 V	5.0 V
BV_{CBO}	5.8 V	17 V
$f_T \cdot BV_{\text{CEO}}$	340 GHz·V	260 GHz·V

current density, respectively. The transit frequency is the frequency where the current gain is equal to unity, and the maximum oscillation frequency gives the frequency where the unilateral power gain equals unity. These frequencies are linked by [Rein 96]

$$f_{\text{max}} \approx \sqrt{\frac{f_T}{8\pi R_B C_\mu}}, \quad (3.1)$$

where R_B is the base resistance and C_μ is the base-collector capacitance that consists of the junction capacitance plus additional parasitic oxide capacitance. Plots of f_T and f_{max} for the HS transistor under different biasing conditions are shown in figure 3.1(a) and figure 3.1(b), respectively. The highest f_T of 200 GHz



(a) Transit frequency f_T versus collector current I_C .

(b) Maximum oscillation frequency f_{max} versus collector current I_C .

FIGURE 3.1: High-frequency characteristics of the HS transistor. The size of the emitter is $0.18 \times 2.6 \mu\text{m}^2$ [Infineon 05].

achieved at a current density of $7 \text{ mA}/\mu\text{m}^2$ and a base-collector voltage V_{BC} of 0 V.

¹The technology also provides an ultra-high speed transistor with 10% higher f_T and f_{max} at the cost of 10% lower BV_{CEO} and BV_{CBO} .

The same current density and $V_{BC} = -1$ V result in the highest $f_{\max} = 256$ GHz. The value of f_{\max} is higher at a larger V_{BC} since C_{BC} decreases with increasing V_{BC} .

Infineon’s SiGe:C technology offers a wide range of emitter mask areas A_E and different contact configurations for the transistors themselves. The standard transistor contact configuration is the base-emitter-collector (BEC) configuration. Its layout is shown in figure 3.2(a). If, for example, a low base resistance is needed, a

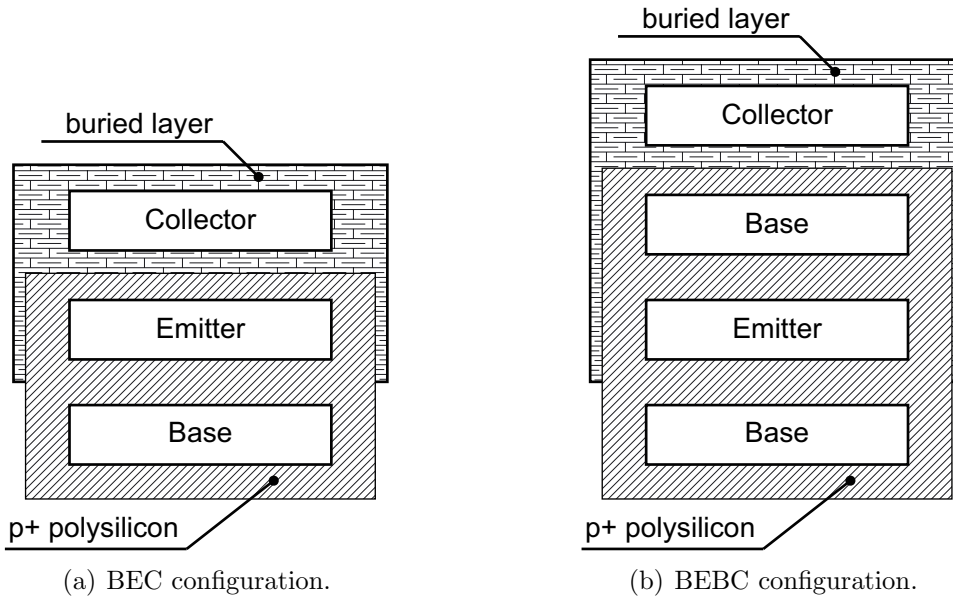


FIGURE 3.2: Single and double base transistor configuration [Perndl 04,a]

transistor with two base contacts (BEBC) can be chosen at the cost of increased base-emitter and base-collector capacitances. This geometry is depicted in figure 3.2(b). Another example is a configuration where two transistors share the same collector. The realization of high-frequency applications, like up-conversion mixers, latches, or multiplexers, is facilitated by this configuration. The shared collector results in a small parasitic capacitance between the buried layer (the collector) and the substrate, C_{CS} . The variety of transistor geometries available from the technology, of which only a few are mentioned here, allows for a powerful optimization of circuit performance.

Transistor cross-section

The npn transistors of Infineon’s SiGe:C technology are implemented using a double-polysilicon self-aligned configuration [Cuthbertson 85]. The SiGe:C base is grown by selective epitaxy, which means that the desired material only grows on a specific surface, e.g. the Si-surface.

A cross-sectional view of the HS npn transistor is depicted in figure 3.3. This

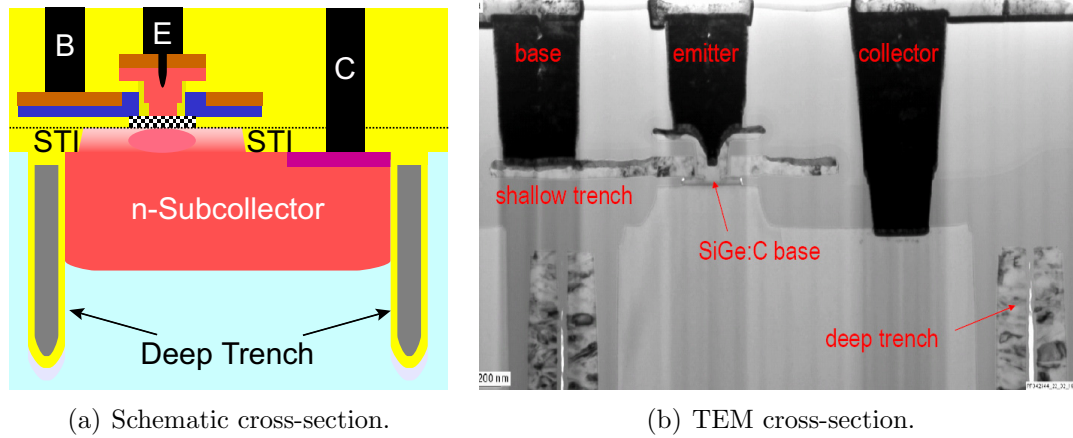


FIGURE 3.3: Cross-sectional view of a HS npn transistor in BEC configuration [Infineon 05].

figure shows the schematic cross-section (figure 3.3(a)) and a TEM photograph of a fabricated transistor (figure 3.3(b)). The cross-section also depicts shallow and deep trench isolation structures. Shallow trench isolation (STI) enables compact transistor dimensions, while deep trenches (DT) isolate the transistors electrically. In addition, due to the position of the DT below the base contact, the collector-substrate capacitance C_{CS} and the base-collector capacitance C_{BC} are small. The base is contacted by a silicided p^+ polysilicon layer and by tungsten vias. The collector contact is brought out from below the transistor via a highly doped, thus low-ohmic, buried layer. It is then contacted to the surface by a highly doped n^+ region and tungsten vias.

The emitter mask window has a drawn width of $0.35 \mu\text{m}$, resulting in a small base resistance. The processed emitter window width is defined by L-shaped nitride spacers that separate the emitter from the base contact. This results in an effective emitter width of $0.18 \mu\text{m}$. The n^+ polysilicon layer for contacting the emitter grows monocrystalline in the effective emitter window. Thus, no barrier exists between the intrinsic emitter and the tungsten emitter contact, yielding a low ohmic contact.

The width of the SiGe:C base is determined by the doping profile. Steep doping gradients enable a small base thickness, which is a requirement for high-frequency transistors. The measured doping profile is depicted in figure 3.4. Doping silicon with germanium (Ge) increases the electron mobility. This results in increased high-frequency performance. The maximum Ge content in the base of the transistors is 25%. A higher concentration does not improve the performance further. The Ge concentration has a graded profile over the base to additionally increase the electrons' drift velocity. Doping the base with boron (B) yields a p-type base. Since the B profile would flatten in further process steps, carbon (C) is implemented in the base to suppress boron diffusion. The n-type characteristic of the

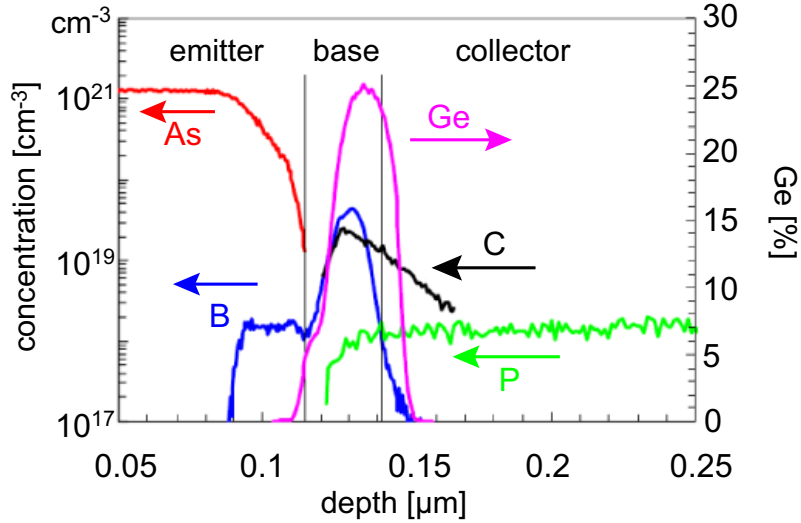


FIGURE 3.4: Vertical SIMS doping profile of the HS transistor: Germanium, Carbon, Boron, Phosphor, and Arsenic [Infineon 05].

emitter and the collector are achieved by doping with arsenic (As) and phosphor (P), respectively.

Small-signal electric transistor model

The currently used electric transistor model within the designkit is based on the SPICE–Gummel–Poon model. The basis for this model is the charge-control theory that links junction voltages, collector current, and base charge. The actual implementation in the designkit extends the model by external resistances and capacitances. The model for a BEC transistor geometry is depicted in figure 3.5. This figure also shows the orientation of the voltages used throughout this document. Details about the SPICE–Gummel–Poon transistor model are not included in this work. A detailed summary about this model is given in an Agilent application note, [Agilent Tech 07,c], for example. The extrinsic model parameters are explained in table 3.2.

TABLE 3.2: Parameters associated with the extrinsic electric transistor model shown in figure 3.5

Parameter	Description
R_B	base series resistance
R_C	collector series resistance
C_{BE}	base-emitter oxide capacitance
C_{BC}	base-collector oxide capacitance

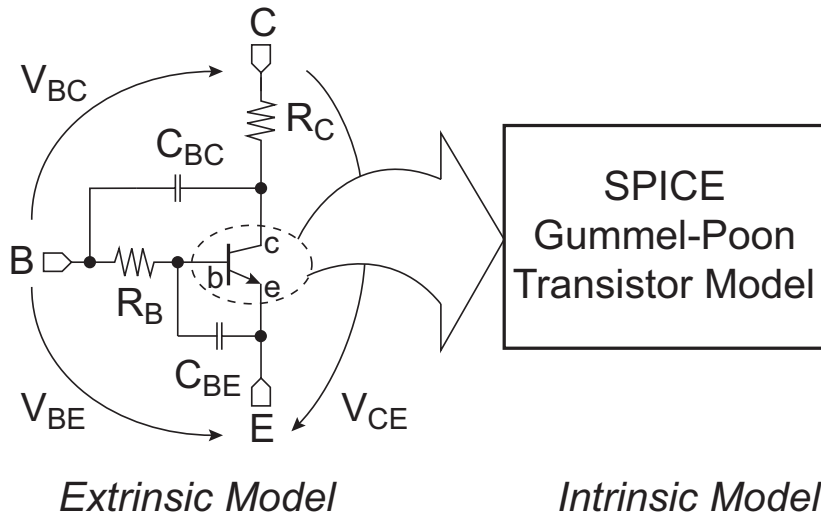


FIGURE 3.5: Small-signal electric model for an npn transistor in BEC configuration.

High-current effects, like base push-out (Kirk-effect [Kirk 62]), are not included in the model. These operating conditions of the transistor must be avoided by careful circuit design.

3.2 Resistors

The used technology offers three different types of resistors: two polysilicon resistors and a TaN resistor [Infineon 05]. They differ in their sheet resistance, temperature coefficient, and parasitic capacitance. Different types of resistors are necessary to provide a wide range of implementable resistance values with reasonable layout area.

Polysilicon resistors are implemented in Infineon's SiGe:C technology with the same process steps as the p^+ -polysilicon base contact, but with a different doping concentration. The two polysilicon resistors themselves differ in their doping concentration only. As a result, they have sheet resistances of $1000 \Omega/\square$ and $150 \Omega/\square$, respectively. The resistors are located on top of a 300 nm oxide layer which isolates them from the substrate. Since the subsequent process steps for the base contact, like the silicidation process, must not affect the resistors, they are covered with oxide. A TEM cross-sectional view of the processed polysilicon resistors is depicted in figure 3.6.

Infineon's SiGe technology offers an additional type of resistor that consists of a tantalum-nitride compound (TaN). This resistor has a sheet resistance of $20 \Omega/\square$. It is implemented between the first and the second metal layer (M1 and M2, respectively), which results in a lower parasitic capacitance than for polysilicon

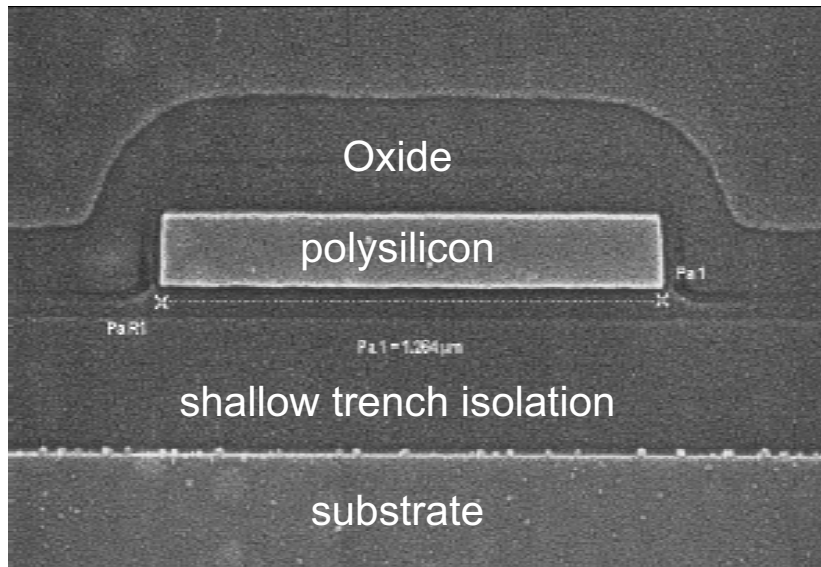


FIGURE 3.6: TEM cross-sectional view of the polysilicon resistor [Infineon 05].

resistors. An additional feature of the TaN resistor is its improved matching constant compared with the polysilicon resistors [Infineon 05]. The matching constant gives the deviation of two adjacent, equally fabricated resistors.

3.3 Metal-Insulator-Metal Capacitor

The required chip area and, thus, the costs of integrated circuits can be kept low if adequate capacitors are included in the technology. The main requirement on capacitors therefore is a large specific capacitance. High quality factors, equivalent to low series resistances, are also required. In addition, coupling into the substrate must be minimized, which requires small parasitic capacitances between the capacitor and the substrate.

Integrated capacitors are fabricated with a thin layer of dielectric between metal layers. The dielectric Al_2O_3 with a relative dielectric constant of $\epsilon_r = 7.9$ is used [Infineon 05]. An implementation of a metal-insulator-metal (MIM) capacitor is depicted in figure 3.7. This figure shows that the surface roughness of the capacitor is only a few nanometers. This is a result of the way the dielectric is implemented. It is processed layer by layer using CVD (chemical vapor deposition). The thickness of the dielectric is 50 nm. This gives a specific capacitance of $1.4 \text{ fF}/\mu\text{m}^2$. Figure 3.8 shows a detailed cross-sectional view of the MIM capacitor. The MIM capacitor is implemented between the second and the third metallization layer of the metal stack (see section 3.4 for details about the metallization). This yields a small parasitic capacitance to the substrate.

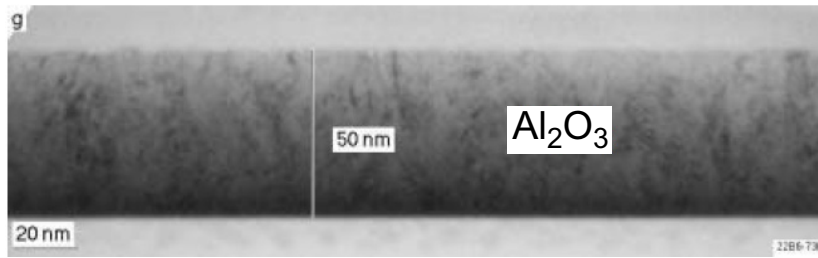


FIGURE 3.7: Implementation of the Metal-Insulator-Metal (MIM) capacitor [Infineon 05].

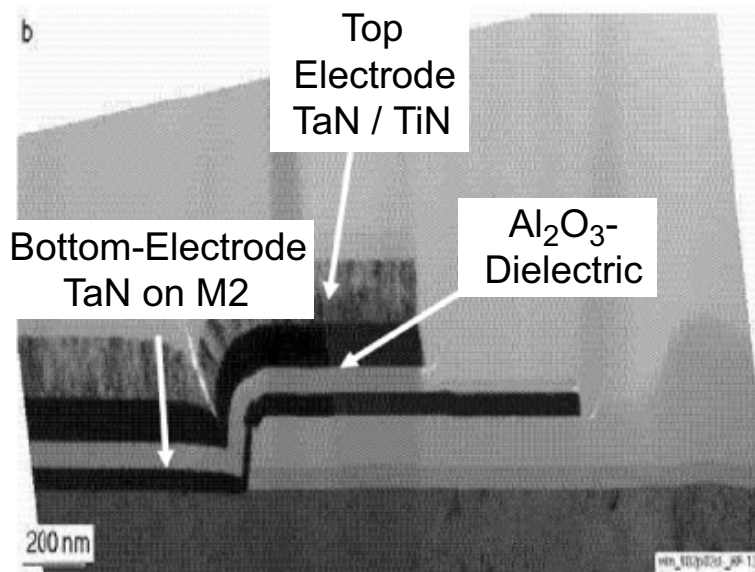


FIGURE 3.8: Detailed cross-sectional view of the MIM capacitor [Infineon 05].

3.4 Transmission Lines

The dimensions of the circuits presented in this work are in the same range as the wavelengths they are operated at. Therefore, passive components can be implemented using distributed in addition to lumped elements. On the other hand, attention must be paid to the design of interconnections between and within building blocks.

Metallization

The technology provides four layers of copper metallization. Other technologies use aluminum for the metal stack. One advantage of copper is the reduced electromigration. In addition, high-quality passive components, like coils and transmission lines, can be implemented due to the high conductivity of copper,

$\sigma_{\text{Cu}} = 57\text{S}/\mu\text{m}$. A schematic plot of the metallization is shown in figure 3.9. The top metal layer (M4) has the largest thickness of all layers, thus it has the

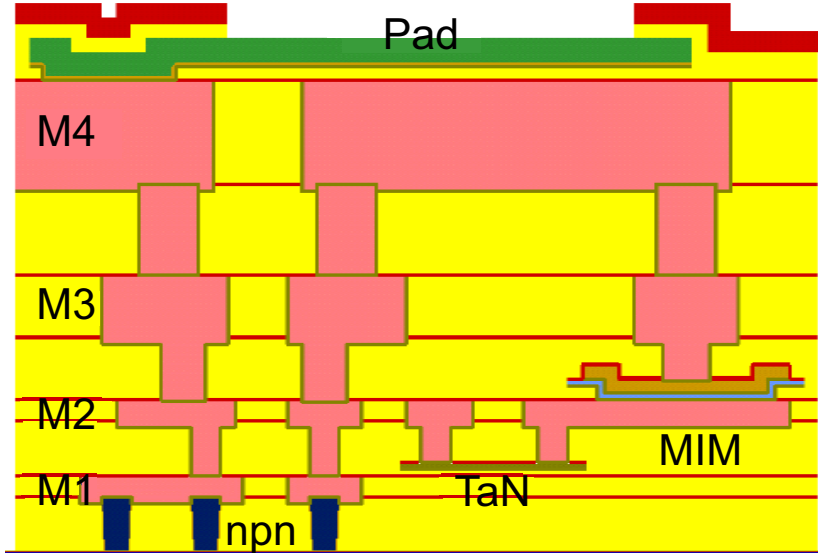


FIGURE 3.9: Schematic view of the metallization layers [Infineon 05].

lowest DC resistance. The thickness of the oxide between the metallization layers increases from M1 to M4. This leads to low capacitive coupling between the top metallization layers and the substrate. Therefore, the M4 layer is attractive for the implementation of coils [Dehlink 07].

Aluminum pads have been used to externally contact the demonstrator chips presented in this work. This material allows the usage of standard techniques and materials for bonding.

Figure 3.10 shows a TEM picture of the metallization layers (or metal stack). Thin layers of nitride compounds are used within the oxide and for the passivation [Schwerd 03]. Those layers have an impact on the properties of the transmission lines that will be described later.

Skin effect

High frequencies cause the resistance of signal lines to be higher than the DC value. Induced eddy currents in the metal result in magnetic fields that push the electric field to the outside of the conductor. This is called skin effect. Thus, the area that is penetrated by the current is reduced, resulting in increased resistance. A measure for the area that is penetrated by the current is the skin depth. It is defined as the distance from the metal surface where the amplitude of an electromagnetic wave is attenuated to $1/e$ of its value at the surface. The skin

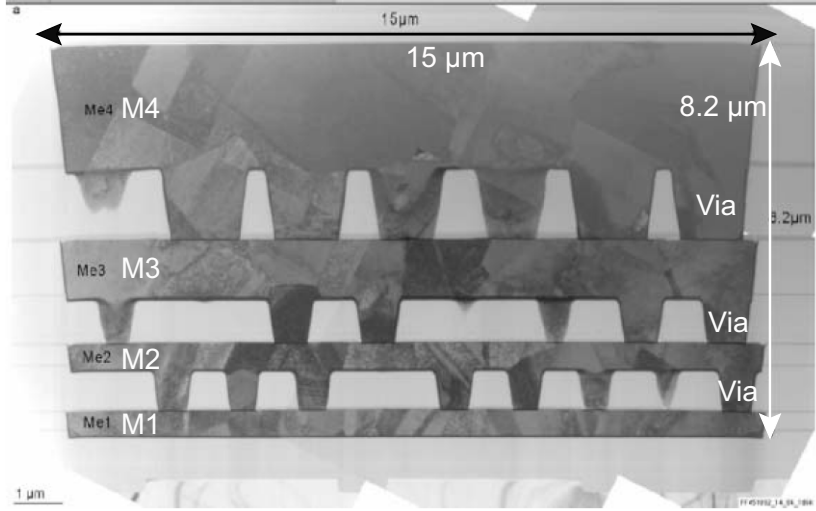


FIGURE 3.10: Metallization of Infineon's SiGe:C bipolar technology [Infineon 05].

depth of plane or circular geometries is given by

$$\delta = \frac{1}{\sqrt{\pi \cdot \mu_0 \mu_r \cdot f \cdot \sigma_x}}, \quad (3.2)$$

where f is the frequency, σ_x is the electric conductivity, and μ_0 and μ_r are the magnetic permeability of vacuum and of the material, respectively. Copper has a conductivity σ_{Cu} of $57 \text{ S}/\mu\text{m}$. The skin depth of copper versus frequency is depicted in figure 3.11. This plot shows that the penetration depth of the current in a plane copper conductor, like a wide ground plane, is 236 nm for 80 GHz.

As a result of the skin effect, the effective area for current conduction is smaller, which increases resistivity. Closed form solutions for the calculation of the AC resistance R_{AC} do not exist for rectangular geometries, like the signal line of a microstrip configuration. Thus, the determination of this resistance is left to simulations or approximations. In [Lotfi 95], conformal mapping, power series solutions, and asymptotic matching techniques are used to provide a single solution for the AC resistance of a single rectangular conductor. The rectangular cross-section is regarded as an ellipse of large eccentricity in this publication. The parameters of the ellipse are

$$b = \frac{2b'}{\sqrt{\pi}}, \quad (3.3) \quad a = a' \frac{b}{b'}, \quad (3.4) \quad \text{and} \quad h = \sqrt{a^2 - b^2}, \quad (3.5)$$

where $2a'$ and $2b'$ are the dimensions of the rectangular conductor ($a' > b'$), a and b are the half-axes, and h is the eccentricity of the ellipse. The length-specific AC resistance of a single rectangular conductor in free space is given by [Lotfi 95]

$$R'_{\text{AC}} = \frac{K(h/a)}{\pi a} \sqrt{\mu_0 f_0 \sigma_x \pi} \cdot \left[1 + \left(\frac{f}{f_l} \right)^2 + \left(\frac{f}{f_u} \right)^5 \right]^{1/10}. \quad (3.6)$$

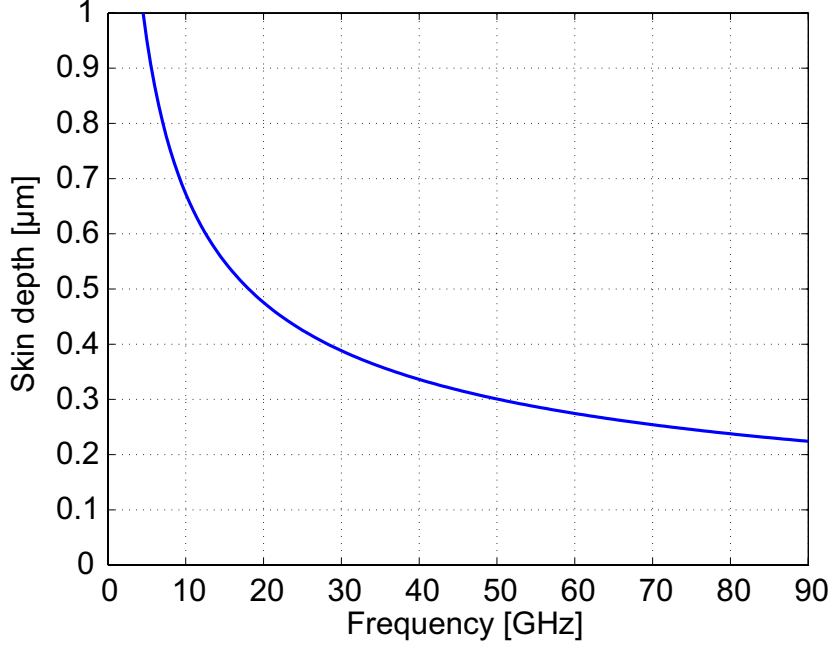


FIGURE 3.11: Skin depth for plane geometries of copper versus frequency.

The first part of this equation gives the length-dependent DC resistance. The complete elliptic integral of the first kind, $K(\cdot)$, is given by

$$K(k) = \int_0^1 \frac{1}{\sqrt{(1-t^2)(1-k^2t^2)}} dt, \quad 0 \leq k \leq 1. \quad (3.7)$$

The corner frequencies f_l and f_u are introduced to satisfy the asymptotic behavior of the AC resistance at low and high frequencies,

$$R'_{AC} \sim \sqrt{f}, \quad f \rightarrow \infty \quad (3.8)$$

$$R'_{AC} \sim 1 + f^2, \quad f \rightarrow 0. \quad (3.9)$$

The corner frequencies are calculated according to

$$f_l = \frac{\pi}{8\sigma_x \mu_0 a' b'} \quad (3.10)$$

and

$$f_u = \frac{\pi^2}{4\sigma_x \mu_0 b'^2} K^{-2}(\sqrt{1 - b'^2/a'^2}). \quad (3.11)$$

For the used technology, these corner frequencies are $f_l = 1.33$ GHz and $f_u = 2.88$ GHz.

A comparison between equation (3.6) and simulations from a 2D field simulator [Weiss 04] is depicted in figure 3.12. The length-specific DC resistance is obtained from the conductivity and the cross-section, $R'_{DC} = 1/[\sigma_{Cu}(5.5 \times 2.4 \mu\text{m}^2)] =$

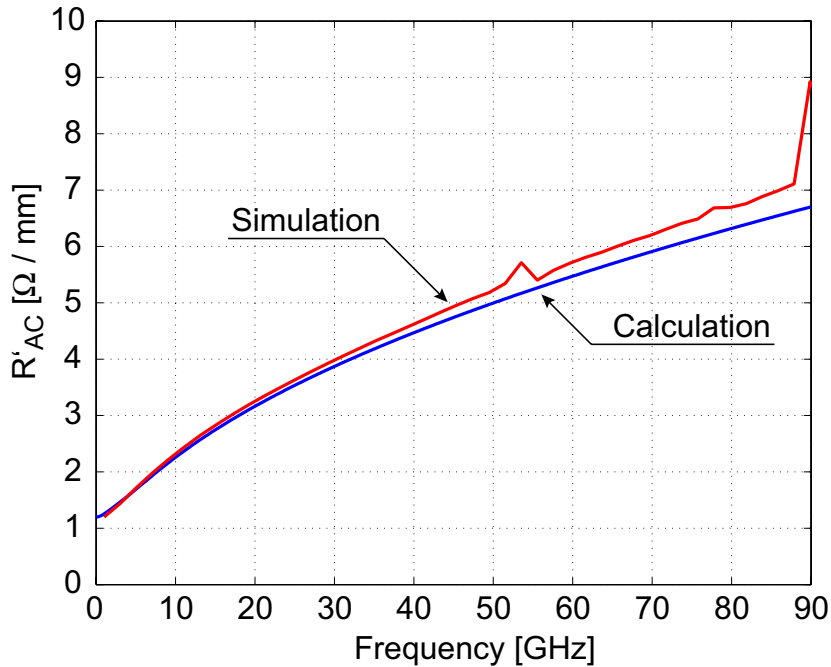


FIGURE 3.12: Comparison of calculation and simulation of the length-specific AC resistance of a single $5.5 \mu\text{m}$ wide and $2.4 \mu\text{m}$ thick copper line.

$1.3 \Omega/\text{mm}$. This figure shows that the deviation of calculations and simulations is smaller than 5% up to 70 GHz. The spikes in the simulated curve result from convergence issues of the simulator at certain frequencies.

Embedded microstrip configuration

Microstrip transmission lines consist of a signal line, a ground plane, and dielectric between them. The signal line is on top of the dielectric and surrounded by air. These lines do not support the propagation of pure TEM waves due to the electric discontinuity between the dielectric and air. The exact fields are best described as hybrid TM-TE waves. Since the thickness of the dielectric is electrically very thin ($d \ll \lambda$), modes that have quasi-TEM character develop, which means that the electric and magnetic field components in propagation direction are negligible [Poazar 01]. Therefore, the phase velocity of a TEM wave gives a good approximation for the phase velocity of quasi-TEM waves,

$$v_p = \frac{c}{\sqrt{\epsilon_{\text{eff}}}}. \quad (3.12)$$

The relative dielectric constant ϵ_r , used for TEM waves, is replaced by the effective dielectric constant ϵ_{eff} , since some of the electric field components are inside the dielectric and some are in air. Therefore, $1 < \epsilon_{\text{eff}} < \epsilon_r$. Approximations for the calculation of ϵ_{eff} exist for microstrip configurations [Hammerstad 80, Poazar 01].

Also approximations for the characteristic impedance Z_0 of a microstrip line are given there.

The metal layers of the SiGe:C bipolar technology are embedded in oxide. Thus, an implementation of a traditional microstrip configuration is not possible. Instead, an embedded microstrip configuration is used, as depicted in figure 3.13. Shown in the same plot are the substrate (resistivity: $18.5\Omega\text{cm}$) and the pas-

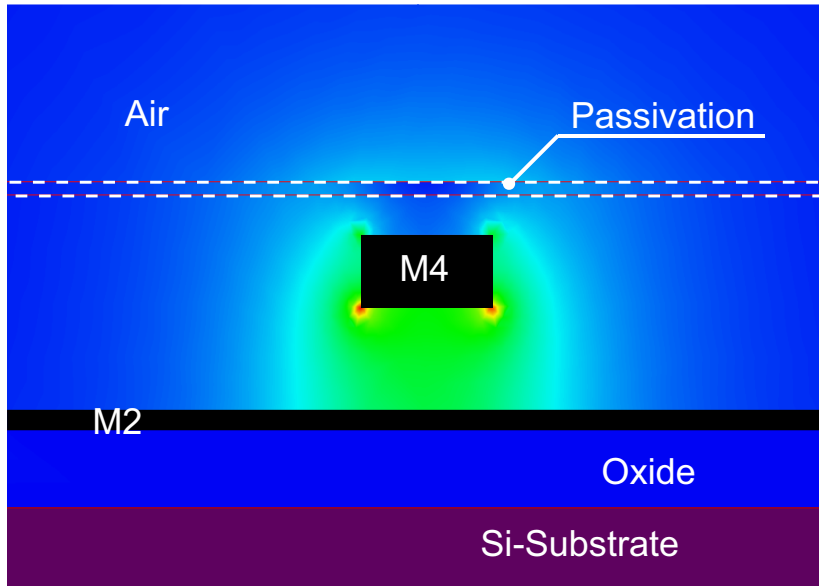


FIGURE 3.13: Magnitude of the electric field of a propagating wave at 80 GHz in an embedded microstrip configuration. The largest field components are red (at the bottom corners of M4), and dark blue represents negligible electric field.

sivation on top of the oxide (nitride, $\epsilon_r = 7.5$). Thin SiN layers in the oxide [Schwerd 03] (not shown in the figure) result in a relative dielectric constant ϵ_r of 4 (pure SiO_2 : $\epsilon_r = 3.9$).

Figure 3.13 additionally plots the magnitude of the electric field, simulated at 80 GHz. The magnitude of the electric field in air is small. This indicates that the mode that develops in this configuration will be a quasi-TEM mode like with the classic microstrip. The approximations for the transmission line properties of microstrip configurations cannot be used for the embedded microstrip line. The transmission line properties are therefore obtained from simulations. The simulated value for the effective dielectric constant of the configuration shown in figure 3.13 is $\epsilon_{\text{eff}} = 3.8$ at 80 GHz. This value results in wavelengths of $\lambda/4 = 498\ \mu\text{m}$ at 77 GHz and $480\ \mu\text{m}$ at 80 GHz.

Special attention must be paid to the realization of the ground plane in the layout. The maximum width of an M2 metal line is limited to $15\ \mu\text{m}$ by design rules. A cheesed structure is used to expand the ground plane. The holes used

for this purpose are much smaller ($20 \times 20 \mu\text{m}^2$) than a tenth of the wavelength. Remembering the distribution of the electric field, figure 3.13, this measure should not impact the properties of the transmission line.

The embedded microstrip configuration supports wave propagation of different modes. The fundamental mode is the quasi-TEM mode. The frequency limit where other modes arise is given by [Hoffmann 83]

$$f_g = \frac{c_0}{2w_{\text{eff}}\sqrt{\epsilon_{\text{eff}}}}. \quad (3.13)$$

Using the definitions given in the cited book for the effective width of the microstrip, w_{eff} , results in a frequency limit of 2.4 THz for the implemented M4 over M2 transmission lines. Thus, only the fundamental mode will propagate on the embedded microstrip configuration.

Some transmission line configurations can suffer from the excitation and propagation of slow-wave modes [Johnson 01]. If the semiconductor in a metal-insulator-semiconductor-metal transmission line configuration is conductive, the electric field penetrates only to the interface between the insulator and the semiconductor. The magnetic field, however, penetrates down to the bottom metallization of the chip. This physical separation of the field components results in the combination of a large capacitance and a large inductance. The group velocity of signals is therefore much slower than the permittivity of either insulator or semiconductor alone would indicate. In addition, the frequency-dependence of slow-wave modes results in signal distortion. Coplanar transmission lines, e.g., or unshielded (from the substrate) interconnects are prone to slow-wave modes. The implemented embedded microstrip configuration is shielded from the substrate, therefore slow-wave modes cannot occur.

Transmission line model

Transmission line components are included in our electric circuit simulations using the lumped element equivalent circuit [Pozar 01]. In this model, an incremental length dz of transmission line is represented by an RLCG circuit. This equivalent circuit is depicted in figure 3.14. The elements of the equivalent circuit model different properties of the transmission line. The length-specific series resistance R' represents the finite conductivity of the conductors; the length-specific inductance L' models the self-inductance; the length-specific shunt conductance G' stands for dielectric losses in the material between the conductors; and the length-specific shunt capacitance C' arises from the close spacing between the conductors. The resistive components R' and G' therefore represent losses. A transmission line of arbitrary length is modeled by cascading the RLCG circuit of figure 3.14.

Closed form solutions for the calculation of the RLCG parameters do not exist for arbitrary geometries. For example, closed form solutions for the parameters

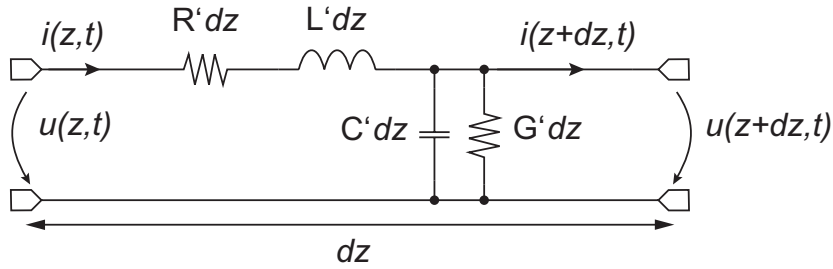


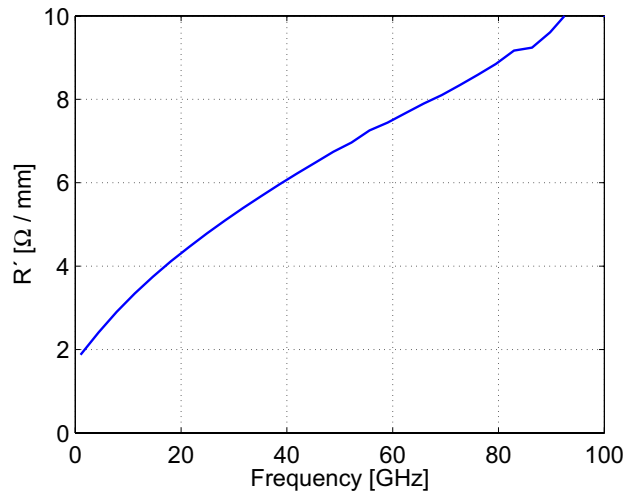
FIGURE 3.14: Lumped-element equivalent circuit of a transmission line segment of length dz .

associated with microstrip configurations, where a dielectric fills the space between the signal line and the ground plane, do not exist. Approximate analytical solutions, however, are possible in many cases, see e.g. [Kaden 74, Hoffmann 83]. Since these approximations cannot be applied to the embedded microstrip configuration, simulations give the parameters. They are presented in figure 3.15 for the configuration shown in figure 3.13. The results are obtained from a simulator that was developed at Infineon [Weiss 04]. The frequency dependence of the length-specific resistance R' is explained by the skin effect, see figure 3.12. The difference to figure 3.12 is a result of the additional resistance associated with the ground plane. Roughly 70 % of the transmission line's AC resistance are caused by conductor M4, while 30 % are contributed by the ground plane, M2. At 80 GHz, R' has a value of $9 \Omega / \text{mm}$. The length-specific inductance L' decreases with frequency. This behavior is also related to the skin effect: The current does not occupy the entire conductor at high frequencies, therefore the inner inductance, which results from the magnetic flux inside the conductor, decreases. The component L' is roughly $325 \text{ pH} / \text{mm}$ at 80 GHz. The capacitance of the embedded microstrip configuration is given by the geometry of the cross-section alone. Hence, the length-specific capacitance is nearly independent of frequency, accounting to $131.4 \text{ fF} / \text{mm}$. The conductance G' represents the losses associated with the dielectric. No published measurements exist for the dielectric losses of SiO_2 at millimeter-wave frequencies, but a low-frequency value states $\tan \delta_{\text{SiO}_2} = 15 \cdot 10^{-6} @ 1 \text{ MHz}$ [Centerline 07]. The millimeter-wave frequency value is expected to be of the same order, therefore G' will be neglected in the model. This assumption is confirmed by the matching of circuit simulations and measurements, presented in chapter 4 and chapter 5.

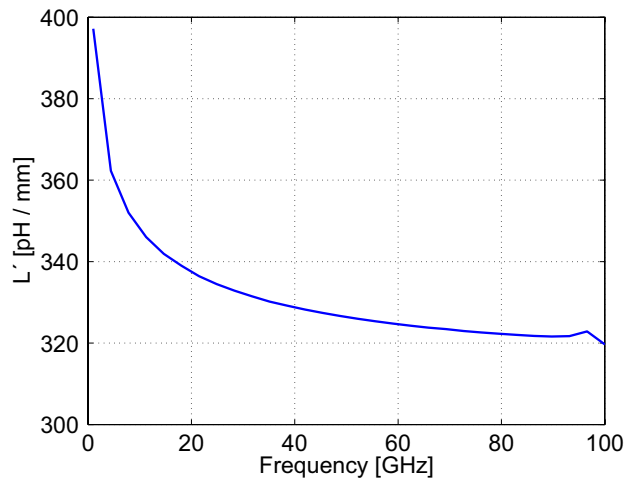
The RLCG model parameters can be converted to the physical properties of a transmission line. The characteristic impedance Z_0 is given by [Pozar 01]

$$Z_0 = \sqrt{\frac{R' + j\omega L'}{G' + j\omega C'}}. \quad (3.14)$$

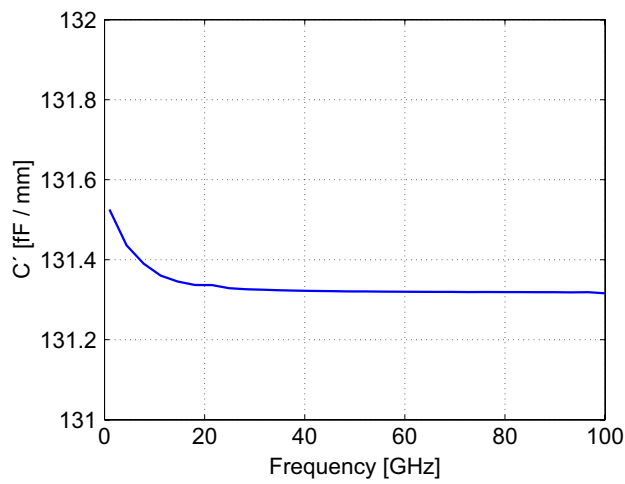
For the embedded microstrip configuration depicted in figure 3.13, the simulated



(a) Length-specific resistance.



(b) Length-specific inductance.



(c) Length-specific capacitance.

FIGURE 3.15: Frequency-dependent lumped element parameters of the $5.5 \mu\text{m}$ wide M4 over M2 embedded microstrip line.

characteristic impedance Z_0 is $(50.38 - j1.43) \Omega$., which is close to the targeted impedance of 50Ω .

The effective dielectric constant ϵ_{eff} is a measure for the electric field distribution of the microstrip configuration. It is almost independent of frequency. The simulated value is $\epsilon_{\text{eff}} = 3.8$. This value is obtained from the ratio of the length-specific capacitance of the embedded microstrip configuration as shown in figure 3.13, and the length-specific capacitance of the same configuration with vacuum as dielectric.

Electromagnetic waves are characterized by their propagation constant. The complex propagation constant γ is linked to the length-specific parameters from the electric model using

$$\gamma = \alpha + j\beta = \sqrt{(R' + j\omega L')(G' + j\omega C')}, \quad (3.15)$$

where β is the phase constant and α determines the attenuation of the wave. The total attenuation α_{total} associated with a transmission line can be split according to

$$\alpha_{\text{total}} = \alpha_{\text{conductor}} + \alpha_{\text{dielectric}}, \quad (3.16)$$

where $\alpha_{\text{conductor}}$ is the attenuation resulting from the metallization and $\alpha_{\text{dielectric}}$ is the attenuation associated with the dielectric. As stated before, dielectric losses are neglected in the model, therefore $\alpha_{\text{total}} = \alpha_{\text{conductor}}$. Figure 3.16 shows the frequency-dependent attenuation (in dB per mm) of the embedded microstrip configuration. The total attenuation associated with the embedded microstrip configuration from figure 3.13 is $\alpha = 0.8 \text{ dB per mm}$ at 80 GHz.

The simulator used, Advanced Design System (ADS), employs the following parameters to model transmission lines: The characteristic impedance Z_0 , the effective dielectric constant ϵ_{eff} , the attenuation coefficient α , and the length. These properties are converted to an equivalent RLCG model internally.

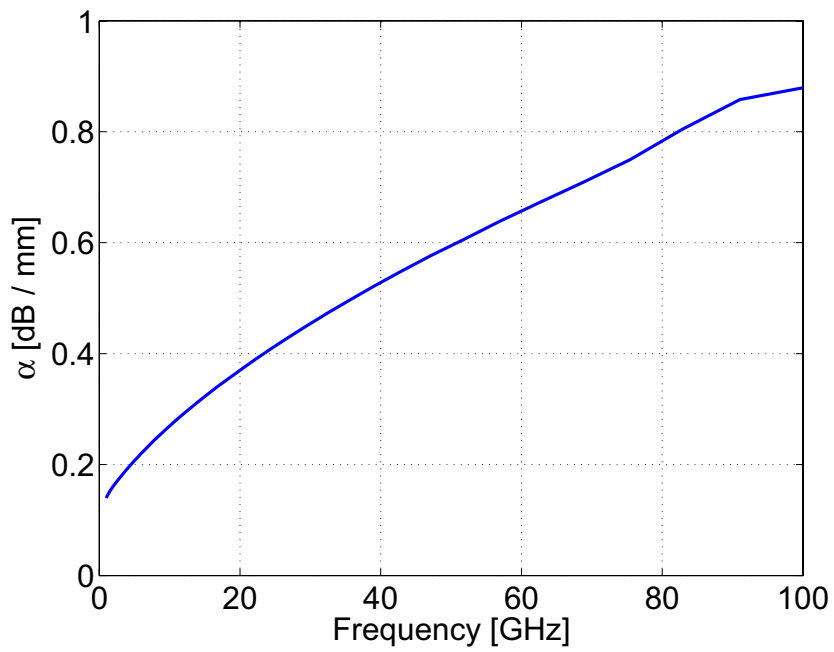


FIGURE 3.16: Attenuation coefficient α versus frequency ($M4 = 5.5\mu\text{m}$, $M2$ ground).

Chapter 4

Highly Linear 77 GHz Down-Conversion Mixer

The design of a receiver frontend at frequencies in the millimeter wave (MMW) range is a challenging task. It is important to analyze every single component regarding its impact on the overall performance. Design, realization, and characterization of an active mixer for automotive radar applications at 77 GHz are discussed in this chapter. The focus in the presented frontend is on simultaneous high linearity and low noise figure. For the HF part of the mixer, different circuit topologies are examined in terms of noise, linearity, and stability. However, it turns out that the best configuration regarding the noise behavior is the one with the highest potential for instability.

4.1 Design Considerations

The frequency translation process in any mixer is accomplished either by exploiting building blocks with nonlinear transfer functions, or by using building blocks with time-varying transfer functions. The nonlinearities can be single device nonlinearities, like the nonlinear transconductance of a transistor. The time-varying transfer function is implemented using switches. While the frequency translation process by nonlinearities is mainly an unwanted side effect, the implementation of a time-varying transfer function is the preferred choice for the realization of mixers.

A time-varying transfer function is implemented by switches. The transfer function A of a switch used in mixers has two discrete states either in amplitude ($A = 1$ and $A = 0$, unipolar operation) or in phase ($A = \pm 1$, bipolar operation). Both operations result in a multiplication of the RF signal by a rectangular waveform with angular frequency ω_{LO} . For bipolar operation, the transfer function in

the frequency domain is represented by

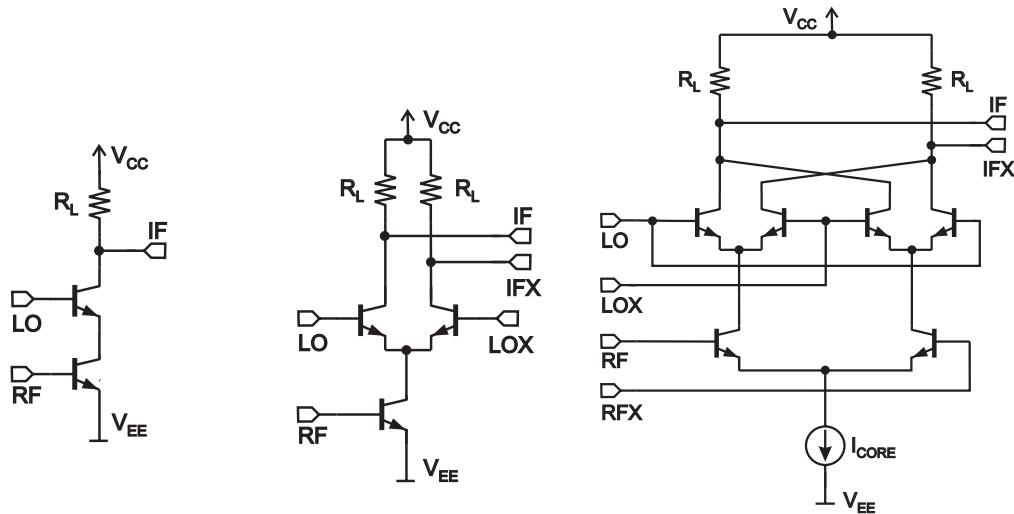
$$S_{LO} = \frac{4}{\pi} \left\{ \sin(\omega_{LO}t) - \frac{1}{3} \sin(3\omega_{LO}t) + \frac{1}{5} \sin(5\omega_{LO}t) - \dots \right\}. \quad (4.1)$$

After multiplication with the RF signal, $S_{RF} = \sin(\omega_{RF}t)$, expansion of the trigonometric products yields

$$S_{IF} = \frac{2}{\pi} \left\{ \cos([\omega_{RF} - \omega_{LO}]t) + \cos([\omega_{RF} + \omega_{LO}]t) - \frac{1}{3} \cos([\omega_{RF} - 3\omega_{LO}]t) - \frac{1}{3} \cos([\omega_{RF} + 3\omega_{LO}]t) + \frac{1}{5} \cos([\omega_{RF} - 5\omega_{LO}]t) + \frac{1}{5} \cos([\omega_{RF} + 5\omega_{LO}]t) \dots \right\}. \quad (4.2)$$

The first element in this equation, $2/\pi \cos([\omega_{RF} - \omega_{LO}]t)$, is the the desired mixing product for a down-conversion mixer. From this equation, the mixing procedure by ideal multiplication with a square wave is inherently associated with signal losses on the order of $2/\pi$, or -3.9 dB.

Active mixers are classified by the configuration of the LO and the RF section. Either single-ended or differential circuit topologies are possible [Gilbert 95]. An overview of mixer implementations suitable for millimeter-wave integration is given in figure 4.1:



(a) Unbalanced Mixer. (b) Single-balanced Mixer. (c) Double-balanced Mixer.

FIGURE 4.1: Mixer topologies.

- *Unbalanced mixer*: The single-ended RF signal is applied to the LO section of the mixer. An unipolar LO switch continuously opens and closes the RF path to the IF. This mixer topology is depicted in figure 4.1(a). Advantages

are low power consumption and low complexity, disadvantages are bad LO - IF and RF - IF isolations. For homodyne systems, the LO - RF isolation is bad since both spectral components are closely spaced and therefore cannot be filtered. A special implementation of the unbalanced mixer is the *sampling mixer* where the switch is opened for a very short period of time rather than by a signal with 50% duty cycle.

- *Single-balanced mixer*: The RF section of this mixer is a single-ended configuration, like a transconductance stage, while the LO part consists of a bipolar switch. The LO signal thus needs to be applied differentially, which means that two single-ended signals have the same amplitude but opposite sign. The IF output is differential. The single-balanced mixer is shown in figure 4.1(b). An advantage of the single-balanced mixer is the single-ended RF input since the RF signal is usually provided single-ended. The disadvantage of this configuration is the leakage of LO signal at the IF output.
- *Double-balanced mixer*: Differential circuit configurations are used at the RF as well as the LO section. Therefore, the LO and the RF signals must be applied differentially. The double-balanced mixer, also known as Gilbert cell, is depicted in figure 4.1(c). An advantage of this configuration is the cancelation of second-order harmonics. With respect to single-ended signal sources, the noise performance of the double-balanced mixer is worse than the noise performance of single-ended configurations since additional losses in front of the active stages are introduced by baluns. Due to the fully balanced topology, no LO components are present at the IF output.

Differential signal transmission uses two signal lines, one carrying the signal, and the other one the inverse of the signal. The information lies in the difference of both. This configuration makes differential signals less susceptible to interferers than single-ended configurations since external impacts in general appear on both lines as a common mode.

The advantages of differential over single-ended designs are [Rein 96, Peeters 97]:

- Reduced distortion (crosstalk, interferers)
- Improved PSRR (Power supply rejection ratio)
- Simpler mounting techniques (ground connections are less critical)
- Lower single-ended voltage swing across load resistors for equal absolute voltage swing

There also exist disadvantages:

- Higher noise figure due to increased number of noise sources

and "LO bias" consist of level shifting diodes, resistors, and bypass capacitors. Details of these blocks are not shown since the design is straight forward.

The topology of the mixer core is based on the four quadrant multiplier presented in [Gilbert 68]. The difference in the design is the focus on mixing operation rather than multiplication. Mixers must exhibit linear behavior only at one port rather than at both input ports, which is the case for multipliers. The linear RF input stage is implemented as a differential common base stage, transistors Q_5 and Q_6 in figure 4.2. This configuration has a broad bandwidth (up to the transistors' f_T) since the base-collector capacitance C_{BC} is shorted to the virtual ground node. Additionally, a differential common base stage is less susceptible to stability issues than common emitter stages. Another advantage of this configuration is the inherent linearization by the resistance of the signal source. The disadvantage of the common base configuration is the limited noise performance in comparison with the degenerated common-emitter configuration.

The thermal noise of the base resistances of the RF transistors $Q_{5,6}$ is amplified like in a common emitter configuration. For this reason, these transistors are designed with a very large size. The RF transistors consist of two emitter fingers with an area of $10.15 \times 0.2 \mu\text{m}^2$ each, and three base contacts. This measure leads to a base resistance on the order of 9Ω .

The switching behavior of the four current commutating transistors Q_{1-4} impacts the noise figure and the conversion gain of the mixer. Thus, the transistors are designed to operate at maximum f_T , or $7 \text{ mA}/\mu\text{m}^2$. Since these transistors operate as switches, they must exhibit their fastest behavior when the current is flowing completely through the outer or the inner pair of transistors, $Q_{1,4}$ or $Q_{2,3}$, respectively. The disadvantage of this design rule is the large base resistance, resulting in high thermal noise that is transferred to the IF output and increases the noise figure.

A current mirror feeds the mixer current of 20 mA to the mixer core. This high current is necessary for the linearity requirement. The current is fed to the mixer core through the virtual ground node. This node is decoupled from the signal path by quarter-wavelength transformers. The two capacitors C_1 and C_2 transform the inductive input impedance of the differential common-base stage to a purely real value.

4.1.2 Local Oscillator Buffer

The performance of the mixer in terms of noise and conversion gain depends on the switching speed of the current commutating transistors (Q_{1-4} in figure 4.2). Thus, as described section 4.1.1, the transistors were designed to operate at maximum f_T , i.e. $7 \text{ mA}/\mu\text{m}^2$. Switching is ideally performed by a rectangular signal. This kind of waveform exhibits an ideal transition from one voltage level to the inverse, so that at no time all switching transistors are 'on'. Fast switching can

be obtained only if large currents are supplied to charge and discharge the inherent parasitic capacitances. These currents must be delivered either by the signal source or by a buffer amplifier. Since loading of the signal source must be avoided, a buffer amplifier that has a high input impedance and a low output impedance is implemented.

The amplifier supplies the current needed to switch the transistors between the 'on' to the 'off' states. It is implemented using cascaded emitter followers since this configuration is capable of driving the subsequent stage without loading the source. The schematic of the LO buffer amplifier without biasing details is depicted in figure 4.3. The input impedance is high, the output impedance is low.

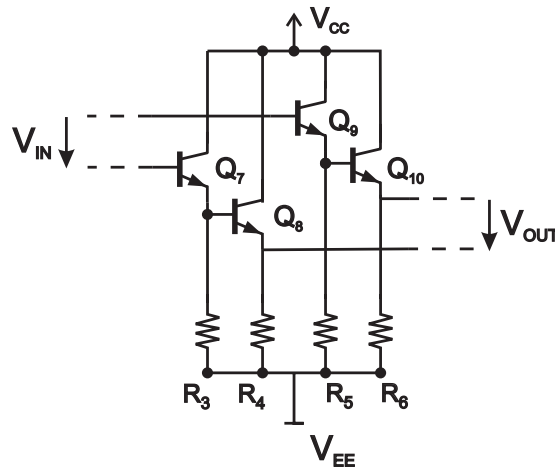


FIGURE 4.3: Schematic of the LO buffer. Biasing details are not shown. The differential signal is provided by the balun. The output voltage is applied to the switching transistors of the Gilbert cell.

Therefore the voltage swing at the load can be larger than the voltage swing at the source.

The input impedance Z_{IN} of an emitter follower depends on the load impedance Z_E times the current gain β ,

$$Z_{IN} \approx \beta Z_E. \quad (4.3)$$

Due to the low current gain at high frequencies, a high value for Z_{IN} can be achieved only by employing a second emitter follower.

The high-frequency input impedance of an emitter follower is given by a series connection of the base resistance r_b , the load impedance Z_E , and a parallel connection of an equivalent resistance and capacitance, R and C . The collector-base capacitance C_μ can be included as a parallel impedance to ground. The equivalent small-signal input impedance of an emitter follower is depicted in figure 4.4 as Z_{IN} . The analytical expression is [Gray 01]

$$Z_{IN} = r_b + \frac{R}{1 + j\omega RC} + Z_E, \quad (4.4)$$

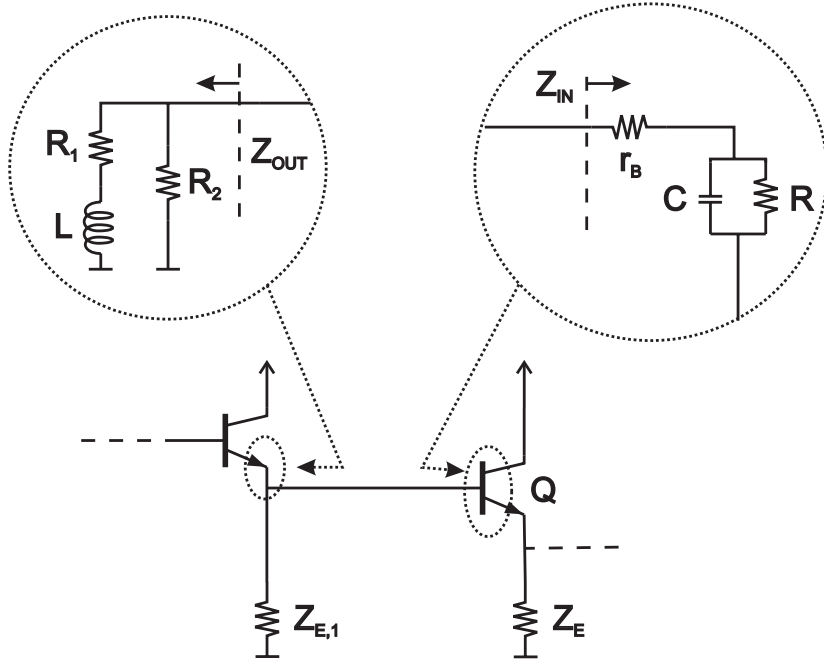


FIGURE 4.4: High-frequency equivalent circuit of one branch of the LO buffer.

The variables R and C are defined by

$$R = (1 + g_m Z_E) r_\pi = \frac{\beta}{g_m} + \beta Z_E \quad (4.5)$$

and

$$C = \frac{C_\pi}{1 + g_m Z_E}. \quad (4.6)$$

The transistor's transconductance is g_m , $r_\pi = \beta/g_m$ is the small-signal input resistance, and C_π is the small-signal input capacitance¹. Accounting also for C_μ , which dominates the input capacitance, the emitter follower's input impedance is capacitive.

The high-frequency output impedance of an emitter follower is given by [Gray 01]

$$Z_{OUT} = \frac{z_\pi + R_S + r_b}{1 + g_m r_\pi}, \quad (4.7)$$

where R_S is the source impedance of the generator driving the emitter follower, and

$$z_\pi = \frac{r_\pi}{1 + j\omega C_\pi r_\pi}. \quad (4.8)$$

¹This capacitance consists of the forward-active base-emitter junction depletion capacitance C_{je} and the base-charging capacitance $C_b = g_m \tau_F$. The parameter τ_F is the forward transit time.

At low frequencies, $z_\pi \approx r_\pi$, thus

$$Z_{\text{OUT}}|_{\omega=0} \approx \frac{1}{g_m} + \frac{R_S + r_b}{\beta_0}, \quad (4.9)$$

where β_0 is the low-frequency current gain. At high frequencies, $z_\pi \rightarrow 0$, yielding

$$Z_{\text{OUT}}|_{\omega \rightarrow \infty} \approx R_S + r_b. \quad (4.10)$$

Therefore, the output impedance of an emitter follower is resistive at low and at high frequencies, and its impedance in between depends on parameter values. For low collector currents, $1/g_m$ is large and dominates the low-frequency output impedance in equation (4.9). With increasing frequency, the impedance decreases to reach the value given in equation (4.10), thus the overall behavior of the emitter follower's output impedance is capacitive.

For collector currents where $1/g_m < R_S + r_b$, $|Z_{\text{OUT}}|$ increases with frequency which is equivalent to inductive behavior. In this case, the output impedance Z_{OUT} can be represented by a parallel connection of an equivalent resistor R_2 and a series connection of an equivalent resistor R_1 with an inductance L . This small-signal output impedance is shown in figure 4.4 as Z_{OUT} . It is given by [Gray 01]

$$Z_{\text{OUT}} = \frac{(R_1 + j\omega L)R_2}{R_1 + R_2 + j\omega L}, \quad (4.11)$$

where

$$R_1 = \frac{1}{g_m} + \frac{R_S + r_b}{\beta_0}, \quad (4.12)$$

$$R_2 = R_S + r_b, \quad (4.13)$$

and

$$L = C_\pi r_\pi \frac{R_S + r_b}{\beta_0}. \quad (4.14)$$

The topology of the configuration depicted in figure 4.4 is the same as that of a negative resistance oscillator [Pozar 01]. From equation (4.4), the real part of the emitter follower's input impedance becomes negative for certain capacitive loads. An inductive impedance at the base of transistor Q in figure 4.4, like the inductance of a short grounded transmission line or the output impedance of another emitter follower, then causes unstable behavior [Kozikowski 64].

The voltage transfer function, depicted in figure 4.5, exhibits a peak at 70 GHz. This is a result of the series resonant circuit formed by the output impedance of the first emitter follower and the input impedance of the second one [Trotta 06]. The mixer circuit in figure 4.2 was simulated with small-signal and large-signal excitation at the LO port. The plot shows the differential voltage at the output referred to the differential voltage at the input of the emitter followers, $V_{\text{OUT}}/V_{\text{IN}}$ in figure 4.3. The blue curves are the result of small-signal (AC) simulations, the red ones result from large-signal (Harmonic Balance) simulation, where $P_{\text{LO}} =$

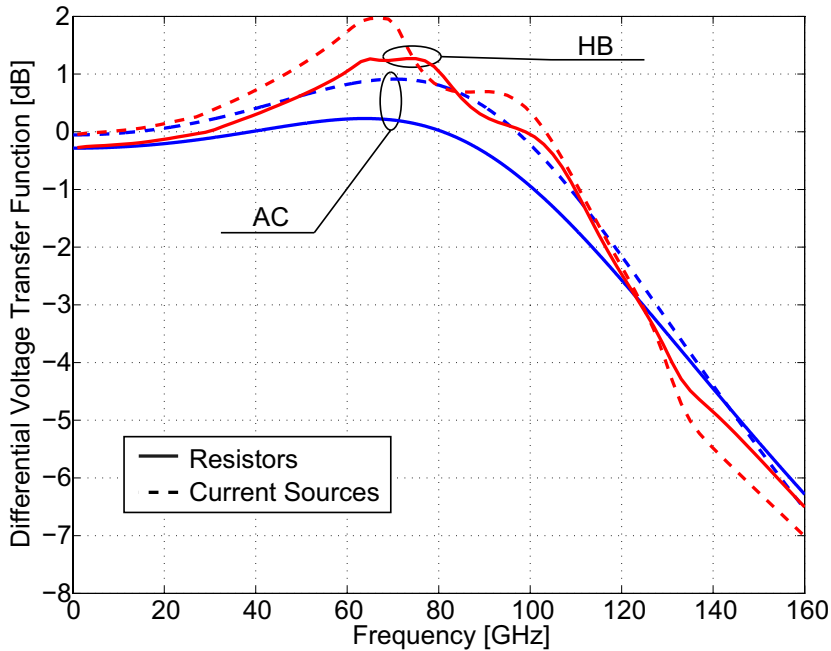


FIGURE 4.5: Simulated differential voltage transfer function of the used LO Buffer, V_{OUT}/V_{IN} in figure 4.3. The simulation frequency is 77 GHz.

0 dBm. The emitter current was provided by resistors (solid curves) and current sources (dashed curves), both including parasitics. The mismatches in the results have different causes:

- The load of the LO buffer are the switching transistors of the Gilbert cell. Their input impedance² is dependent on the LO level. The load impedance connected to the emitter of one switching transistor, Z_E , is given by the parallel connection of the impedance looking into the emitter of the second transistor and the output impedance of the RF transistor ($Q_{5,6}$ in figure 4.2). Different signal levels result in different impedances:
 - For small-signal operation, the input impedance of one switching transistor is mostly determined by the low impedance path to ground through the opposite transistor. Its input impedance is given by the output impedance of an emitter follower, see equation (4.11).
 - Large-signal operation increases the input impedance of the differential pair to the input impedance of an emitter follower, see equation (4.4). The load impedance at the emitter, Z_E , is now mostly determined by the output impedance of the RF transistor since the second transistor

²The term 'impedance' refers to the voltage to current ratio at the fundamental frequency. The LO signal is assumed to be a sinusoidal waveform, which is justified due to the high operational frequency.

is turned "off". The output impedance of the RF transistor consists of the small-signal output impedance r_o of the transistor in parallel to the collector-substrate and collector-base capacitances, C_{CS} and C_{BC} , respectively. The output resistance r_o is given by

$$r_o = \frac{V_A}{I_C}. \quad (4.15)$$

The numerator, V_A , is the forward Early voltage, and its absolute value is 150 V for the technology used. The denominator is the collector current, I_C , and is 10 mA for the presented circuit. This results in a value of 15 k Ω for r_o . The total capacitance at the collector of the RF transistors is on the order of $C_{par} = 20$ fF, so the overall impedance is dominated by this value ($1/\omega C_{par} = 103.3 \Omega$ at 77 GHz). Under large-signal operation, the LO buffer including the switching transistors forms a series connection of three emitter followers with capacitive load, which is the reason for the increased overall gain compared to the case of small-signal excitation.

- The difference in the shape of the AC and HB curves is a result of changes in the input impedance of the first emitter followers under large-signal excitation. By this, the resonant tank that consists of the transmission lines of the balun and the capacitance of the emitter follower changes. Therefore, the curves from the HB simulation are not as smooth as the ones from AC simulation.

Figure 4.6 shows a Harmonic Balance simulation of the differential voltage transfer function versus temperature. The available resistor types of the used technology (p⁺ poly, p⁻ poly-, and TaN) are compared with respect to their impact on the LO buffer transfer function. At room temperature, the voltage transfer function of the LO buffer has a value of +1 dB. The resistor of the p⁺ poly type has a positive temperature coefficient, which means that the resistance increases with temperature, and the other types have negative temperature coefficients. A negative temperature coefficient thus results in larger currents at higher temperatures. Therefore, the p⁻ poly resistor is the best choice. The TaN resistor shows comparable performance in terms of temperature behavior, but its size in the layout is much larger than the size of the other implementations because it has a low specific resistance. Using p⁻ poly resistors instead of p⁺ poly resistors increases the temperature where the voltage transfer function of the buffer is larger than 0 dB from 80°C to 110°C.

4.1.3 Balun Design

Measurement equipment for millimeter-wave frequencies typically have single-ended inputs or outputs. Therefore, an unbalanced to balanced transformer must be included to benefit from the advantages of differential circuits.

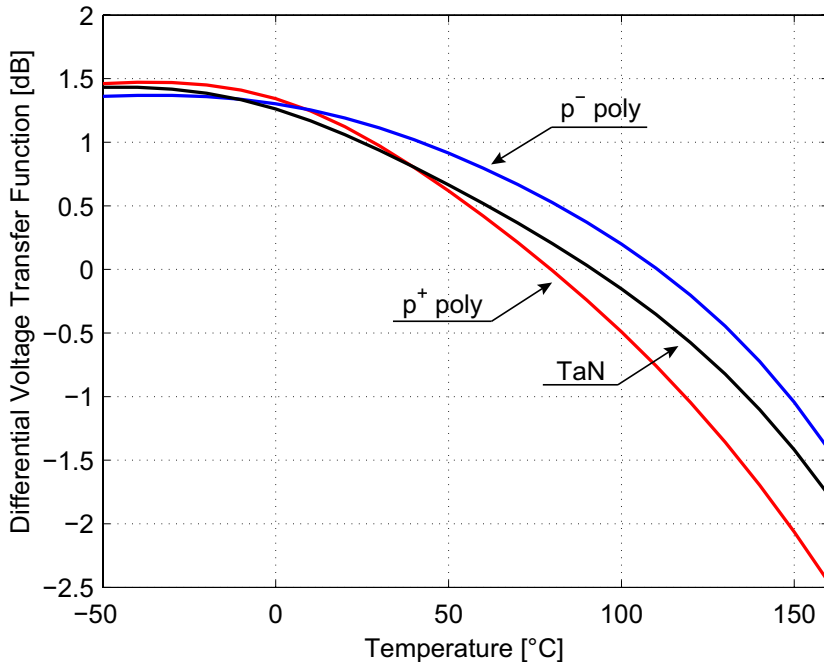


FIGURE 4.6: Simulated (HB) temperature behavior of the differential voltage transfer function of the LO buffer. Different types of resistors are compared. $P_{LO} = 0$ dBm, $f_{LO} = 77$ GHz

Regarding the RF path, a requirement on the performance of the balun is low insertion loss. Any losses in front of the device degrade the noise figure and the conversion gain of the mixer. Therefore, coupled structures like Lange couplers or transformers are bad choices. In addition, these configurations occupy large chip area.

A simple and low insertion loss implementation of an on-chip balun is based on the LC-balun described in [Vizmuller 95]. This balun consists of two inductors and two capacitors in a bridge configuration. One branch shifts the single-ended input signal by $+90^\circ$, the other branch by -90° . The LC realization provides the desired phase shift, amplitude balance, and impedance matching simultaneously. These properties and the small occupied area make it an ideal candidate for on-chip integration.

The required values for the inductors and capacitors are dependent on the source resistor R_S and the differential load resistor R_L . They are calculated using

$$L_{1,2} = \frac{\sqrt{R_S R_L}}{\omega} \quad (4.16) \quad \text{and} \quad C_{1,2} = \frac{1}{\omega \sqrt{R_S R_L}}. \quad (4.17)$$

High-frequency applications offer the possibility to replace the inductors with transmission lines [Bakalski 02], as depicted in figure 4.7. The replacement of capacitors with stubs is also an option but was not implemented since the used technology provides MIM capacitors. The procedure for the calculation of the

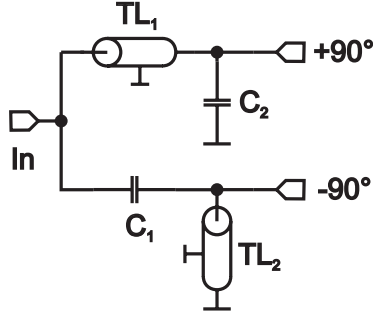


FIGURE 4.7: Balun with transmission lines. $Z_0 = 50 \Omega$

lengths of the transmission lines is as follows:

1. Calculate the value of the capacitors $C_{1,2}$ and the inductors $L_{1,2}$ using equations 4.16 and 4.17.
2. Transform the inductor values to electric lengths using

$$\varphi_1 = \arctan \frac{\omega L_1}{Z_0}, \quad \varphi_1 < \frac{\pi}{2}, \quad (4.18)$$

$$\varphi_2 = \arcsin \frac{\omega L_2}{Z_0}, \quad \varphi_2 < \frac{\pi}{2}, \quad (4.19)$$

where Z_0 is the impedance of the transmission line, $\frac{\pi}{2} \triangleq \frac{\lambda}{4}$, and λ is the wavelength in the microstrip line, e.g. $\lambda = 1.992 \text{ mm}$ in SiO_2 at 77 GHz.

3. Calculate the length of the transmission lines for the layout.

The disadvantage of the described procedure is the necessity for real load and source impedances. Usually, the source impedance has an imaginary part, for example due to the parasitic pad capacitance ($C_{\text{pad}} = 25 \text{ fF}$). Additionally, the used capacitors have a parasitic stray field that cannot easily be included in the above calculations. These points show the need for an automated optimization tool. The used simulator, ADS, offers such an optimizer. The calculated values of idealized circuits were used as the starting point for the optimization process.

The optimizer uses small-signal analyses to determine the amplitude and phase difference at the input of the differential pairs. Then, an error function returns a measure for the deviation from the desired value, which can be, e.g., $180^\circ \pm 5^\circ$ for the phase difference. By variation of the parameters, which are the length of the transmission lines and the capacitors, the gradient of the error function is determined. The gradient is used to find the minimum value for the error function and the corresponding device parameters.

The amplitude ratio in dB and the phase difference at the output port of the RF balun are depicted in figure 4.8. At the center frequency of 77 GHz, the amplitudes

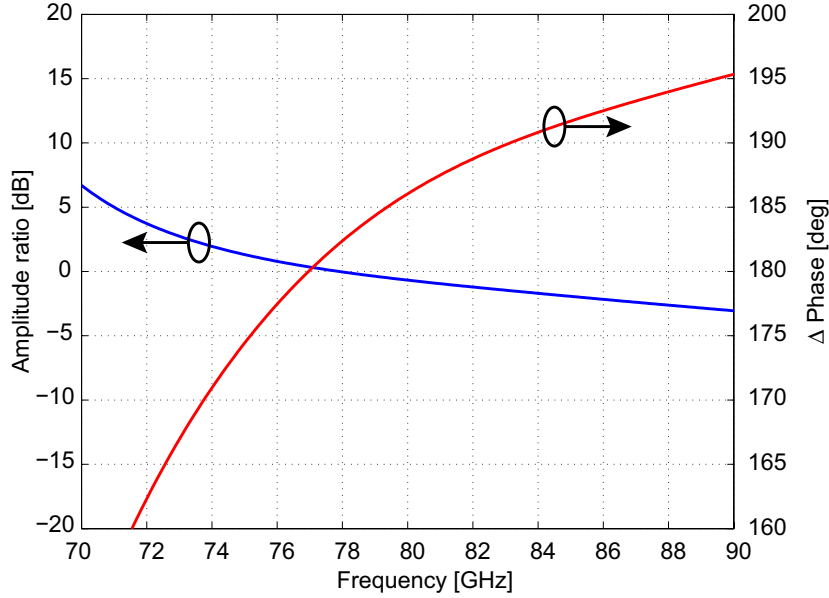


FIGURE 4.8: Simulated (AC) amplitude ratio and phase difference at the differential port of the RF balun versus frequency.

are equal and the phase difference is 180° . From 73 to 88 GHz, the amplitude ratio remains below 3 dB. The phase difference is in the range of $180^\circ \pm 10^\circ$ from 74 to 83 GHz. The overall mixer circuit behavior is only weakly affected by variations in the phase difference since the baluns are followed by differential amplifiers that suppress common mode signals.

Designing the balun for the LO path requires additional attention. The emitter followers of the LO buffer are operated with large signals that influence the LO buffer's biasing and, consequently, its input impedance (see section 4.1.2). The balun is designed for a specific load impedance, therefore, any changes in this impedance affect the phase split and the amplitude ratio. Therefore, after optimizing the balun using small-signal analysis, the behavior of the balun must be checked when large signals are applied to the following stages. If needed, the values must be adjusted. The deviations of the phase and the amplitude for an AC (small-signal) and a Harmonic Balance (large-signal) simulation are depicted in figure 4.9(a) and figure 4.9(b), respectively. The balun was optimized using AC simulations only. The graph shows that the differences between the AC and the HB simulation regarding the amplitude ratio are negligible over the whole frequency range. The phase shows the largest difference at 60 GHz, 6° . Around the frequency of interest, 77 GHz, the difference between the two simulations is 1° at most .

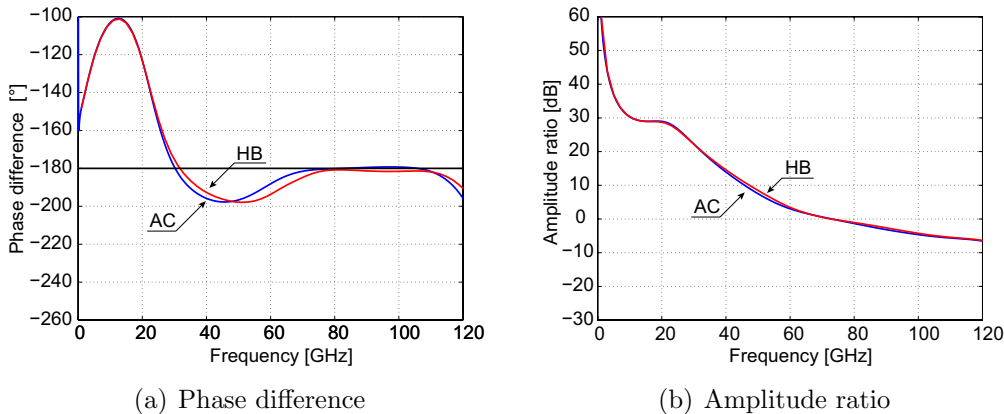


FIGURE 4.9: Comparison of the phase difference and amplitude ratio of the LO balun's differential output signals. Small-signal (AC, blue curve) and large-signal (Harmonic Balance, red curve) analyses are investigated. The large-signal analyses use an input power P_{LO} of +5 dBm.

4.2 Performance Parameters

The design considerations presented in the previous section are only a gross overview of the implemented design. In this section, the most important parameters of the active circuit are elaborated in detail. These are linearity, noise, and stability. Other properties, like AM suppression of the LO signal, LO leakage, and a sensitivity analysis are important for the application and are therefore treated at the end of this section.

4.2.1 Linearity

The nonlinearity of a circuit is one measure for signal degradation. Any changes of the signal shape in the time domain except scaling and delay are regarded as distortion. In the frequency domain, distortion refers to additional frequency components that are generated by the circuit. Frequency converting devices like mixers exploit nonlinearities to generate frequency components different from the input signal. Thus, only unwanted additional frequency components are regarded as distortion.

Linear circuits can also cause distortion [Sansen 99]. For example, a filter with a linear but nonconstant amplitude or phase transfer characteristic changes the shape of a broadband input waveform, e.g. of a square wave.

Nonlinear distortion is the major cause for linearity issues in active circuits. Different mechanisms that have an impact on the linearity can be identified:

Nonlinear transconductance: Distortion in heterojunction bipolar transistors (HBTs) is caused by the nonlinear dependence of the HBT's collector current I_C

on the base-emitter voltage V_{BE} . For operation in the forward-active region, this dependence follows an exponential law,

$$I_C(V_{BE}) \approx I_{CS} \left[\exp\left(\frac{V_{BE}}{V_T}\right) - 1 \right], \quad (4.20)$$

where I_{CS} is the collector saturation current and V_T the thermal voltage. Equation (4.20) is a strongly nonlinear function. Since only large magnitudes of V_{BE} are treated in this section, the last term in equation (4.20) will be neglected in the following considerations.

The nonlinearity of an HBT is dependent on the peak signal levels of V_{BE} and, thus, I_C [Sansen 99]: Both the base-emitter voltage and the collector current can be split into a DC and an AC component,

$$I_C = I_{C0} + i_C, \quad (4.21)$$

$$V_{BE} = V_{BE0} + v_{BE}. \quad (4.22)$$

Insertion of these expressions into equation (4.20) results in

$$I_{C0} + i_C \approx I_{CS} \exp\left(\frac{V_{BE0} + v_{BE}}{V_T}\right). \quad (4.23)$$

Normalizing the components of this equation to the DC values obtained from equation (4.20) yields

$$1 + \tilde{i}_C \approx \exp\left(\frac{v_{BE}}{V_T}\right), \quad (4.24)$$

where \tilde{i}_C is the relative current swing i_C/I_{C0} . It is the fraction of the DC current in the transistor that generates AC output signals.

The exponential term in equation (4.24) can be expanded into a Taylor series,

$$\exp(x) = 1 + x + \frac{x^2}{2} + \frac{x^3}{6} + \dots \quad (4.25)$$

Since the peak absolute values of the base-emitter voltage \hat{V}_{BE} and the collector current \hat{I}_C are the largest magnitudes that appear in the device, they determine the linearity. Thus, these values are inserted into equation (4.24), yielding

$$\hat{i}_C = \frac{\hat{I}_C}{I_{C0}} = \frac{\hat{V}_{BE}}{V_T} + \frac{1}{2} \left(\frac{\hat{V}_{BE}}{V_T}\right)^2 + \frac{1}{6} \left(\frac{\hat{V}_{BE}}{V_T}\right)^3 + \dots \quad (4.26)$$

The first term of this equation is the small-signal transconductance, $\hat{I}_C = g_m \hat{V}_{BE}$. Equation (4.26) shows that the peak base-emitter voltage's impact on the linearity depends on the DC collector current [Sansen 99]. Aside from the peaks related to the input signal, voltage or current spikes caused by switching, e.g., also result

in an increase of the magnitude of higher-order harmonics. In order to realize a highly linear circuit, a large tail current (20 mA) was chosen for the design of the mixer cell.

Nonlinearities due to the transistor’s capacitances: The behavior of the transistor in terms of linearity is, aside from the voltage–current dependence, additionally influenced by the base–emitter and base–collector depletion capacitances³. The bias dependence of the depletion capacitance C_J is given by [Reisch 02]

$$C_J(V) = \frac{C_{J0}}{(1 - V/V_J)^M}, \quad (4.27)$$

where V is the applied voltage and C_{J0} is the value of C_J for $V=0$. The voltage V_J is dependent on the doping and the exponent M depends on the type of junction ($M = 1/2$ for abrupt junctions, $M = 1/3$ for linear junctions). Equation (4.27) shows that the depletion capacitance is de facto constant for large reverse biases ($V \gg 0$). This applies to the biasing conditions of all base–collector junctions in the mixer core. When the voltage across the junction is close to zero or the junction is forward biased (as in the base–emitter junction), the changes in capacitance C_J are nonlinear. Both the voltage dependence and the absolute value of the base–emitter depletion capacitance have an impact on the linearity of HBTs [Welch 99].

The entire transistor: Although many elements in an HBT exhibit nonlinear behavior, the overall linearity of the transistor can be quite good at high frequencies. The reason for this phenomenon is the partial cancelation of nonlinear effects. In [Maas 92], the partial cancelation of the nonlinear behavior of the base–emitter junction resistance and capacitance are identified as contributors to the HBT’s linearity. It depends on several factors, like the frequency, the load impedance, and the biasing, whether or not these nonlinearities cancel. This is verified analytically in [Samelis 92] and experimentally in [Welch 99]. The latter two publications identify impacts associated with C_{BC} as the largest contributions to the total linearity.

Under small-signal operation, C_{BC} is quite linear (if biased properly). Thus, it is not the nonlinearity of this capacitance, but the feedback path from the collector to the base provided by this capacitance that linearizes the device [Wambacq 98]:

- Part of the fundamental tone is fed back to the base of the device and acts as a negative feedback which linearizes the transistor.
- Degradation of linearity due to C_{BC} is caused by the second-order harmonics at the collector of the device. They are fed back to the base through C_{BC} and generate distortion at the fundamental frequency by mixing with the fundamental tone [Aparin 99, Sheng 03].

³The impact of the diffusion capacitance of the base–emitter junction is usually negligible [Niu 99].

Nonlinearity of the differential amplifier The basis for differential designs is the differential amplifier. A differential amplifier can be either an emitter-coupled pair (with or without degeneration) or a differential common-base stage. The differential voltage transfer function of an emitter-coupled pair is [Meyer 77],

$$V_{od} = \alpha_F I_{EE} R_C \tanh\left(-\frac{V_{id}}{2V_T}\right), \quad (4.28)$$

where V_{id} and V_{od} are the differential input and output voltages, respectively, α_F is the ratio of the collector and the emitter current, I_{EE} is the tail current, and R_C represents the load. It is apparent from this equation that the input-output characteristic is, strictly speaking, never linear.

The smallest changes in the slope of equation (4.28) are in the vicinity of $V_{id} = 0$. This region can be extended by insertion of an impedance between the emitters of the emitter-coupled pair. This measure results in a linearization by introducing negative feedback [Abidi 03]. It is shown in [Fong 98] that inductive degeneration is superior to resistive and capacitive degeneration in suppressing intermodulation products. Regarding noise behavior, inductive degeneration outperforms resistive degeneration. In a differential common-base stage, the voltage drop across the series connection of the source resistance of the signal source and the input impedance of the transistor is large due to the high input signal current. Thus, this configuration offers inherent resistive degeneration [Qin 07].

Under large-signal excitation, the output waveform can be distorted due to limited voltage headroom at the load impedance. The maximum available output swing is limited by the supply voltage on the one side, and by saturation of the transistors on the other side. Once the output signal is "clipped" due to these limits, additional harmonics are generated.

Nonlinearities in Mixers: Regarding mixers, the switches have an influence on signal distortion [Meyer 86]. The intermodulation products are dependent on the voltage level driving the LO. At low LO levels, the intermodulation performance improves with increasing LO amplitude since the impact of the nonlinearities introduced by the switching transistors is small. When the switching transistors are fully switched, they are in a common base configuration for the signal path. This topology has good properties in terms of linearity [Sansen 73]. High LO levels result in large voltage variations at the common-emitter node, thus the collector potentials of the RF transistors change. This modulates the collector-base capacitance, generating harmonics. In the design process, the voltage across the base-collector junction of the RF transistors should therefore be as large as possible. An optimum value exists for minimum intermodulation products [Kim 02, Meyer 86, Terrovitis 00].

Second-order Intermodulation

Two tones at closely spaced frequencies ω_1 and ω_2 applied to the input of a nonlinear device result in second-order intermodulation products that are located at $\omega_1 \pm \omega_2$. Therefore, they appear in the baseband and at roughly twice the RF frequency. The baseband components lead to errors in target detection of radar systems. The high-frequency components result in additional third-order distortion due feedback via C_{BC} and mixing with the fundamental tone. Thus, the second-order intermodulation point, defined as the (extrapolated) point where the second-order harmonics are as large as the fundamental tone, is important from a system as well as from a linearity point of view.

Second-order intermodulation arises from impairments in the symmetry of the circuit [Kivekäs 01, Sheng 03]. In a mixer, the suppression of even order products additionally requires LO amplitude balance at the switches and a 50 % duty cycle [Razavi 97]. In [Kivekäs 01], analyses and experiments show that a combination of device mismatches and LO mismatches can result either in IP_2 improvement or degradation. The absolute voltage level of the LO additionally impacts the IP_2 .

Third-Order Intermodulation

Applying two closely spaced input tones at ω_1 and ω_2 to a nonlinear device yields intermodulation products of third order that are closely spaced to the frequencies of the fundamental tones, $2\omega_1 - \omega_2$ and $2\omega_2 - \omega_1$. They cannot be filtered since also the fundamental tones were affected.

The simulated fundamental tone and third-order intermodulation products of the mixer from subsection 4.1.1 versus RF input power are depicted in figure 4.10. The extrapolated lines intersect at the third-order intercept point (IP_3). This graph shows the RF power in dBm on the horizontal and the differential peak-to-peak output voltage of the intermediate frequency in dBV_{pp} at the vertical axis⁴. The RF frequencies for the two-tone simulation are 76.510 GHz and 76.515 GHz. The LO frequency is 76.5 GHz, the LO power level is +2 dBm. The simulated input-referred third-order intercept point is +7.5 dBm.

Frequency components at twice the RF input frequency have an impact on the IP_3 as derived at the beginning of the subsection. The largest components are generated by the emitter-coupled LO transistors, which act as full-wave rectifiers for the LO signal [Pozar 01]. Expanded to a Fourier series, the rectified LO signal is

$$A_{LO}|\sin(\omega_{LO}t)| = A_{LO}\frac{4}{\pi}\left(\frac{1}{2} - \frac{\cos(2\omega_{LO}t)}{3} - \frac{\cos(4\omega_{LO}t)}{15} - \dots\right), \quad (4.29)$$

where A_{LO} is the magnitude of the LO signal. Neglecting the DC component, the largest components at the common emitter node are at twice the LO frequency.

⁴The unit dBV_{pp} refers to the peak-to-peak voltage referred to 1 V on a logarithmic scale.

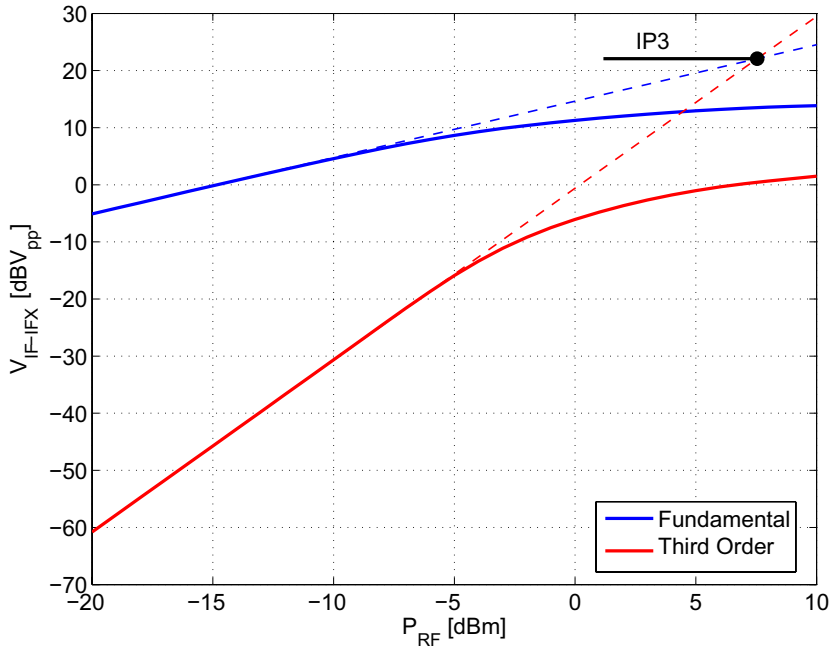


FIGURE 4.10: Simulation of the input-referred third-order intercept point. $iIP3_{sim} = +7.5$ dBm.

This large signal is then fed to the base of the RF transistor via C_{BC} , generating further harmonics by interaction with the RF signal. The dependence of the input-referred IP_3 on the LO power is depicted in figure 4.11. At low LO power levels, the degradation of the IP_3 due to the LO can be neglected since the LO power is too weak to generate perceivable harmonics. At a power level of -2 dBm, the distance between the amplified fundamental tone and the third-order harmonics is maximum. Beyond that power level, the generation of harmonics due to excessive LO power deteriorates the IP_3 .

1 dB Compression Point

The input referred 1 dB compression point is defined as the input power level where the gain of the device decreases from the nominal value by 1 dB. In contrast to the second and third-order intermodulation points, the 1 dB compression point can be determined experimentally without the uncertainty of extrapolation.

For systems that exhibit mainly third-order nonlinearities, the 1 dB compression point and the third-order intercept point are 9.64 dB apart [Sansen 99]. For systems that cannot be classified weakly nonlinear, the distance between the 1 dB compression point and the third-order intercept point differs from this value. The reason is that the 1 dB compression point is determined by the magnitudes and the phases of all intermodulation products and harmonics, contrary to the IP_3 that measures the magnitude of the intermodulation products due to third-

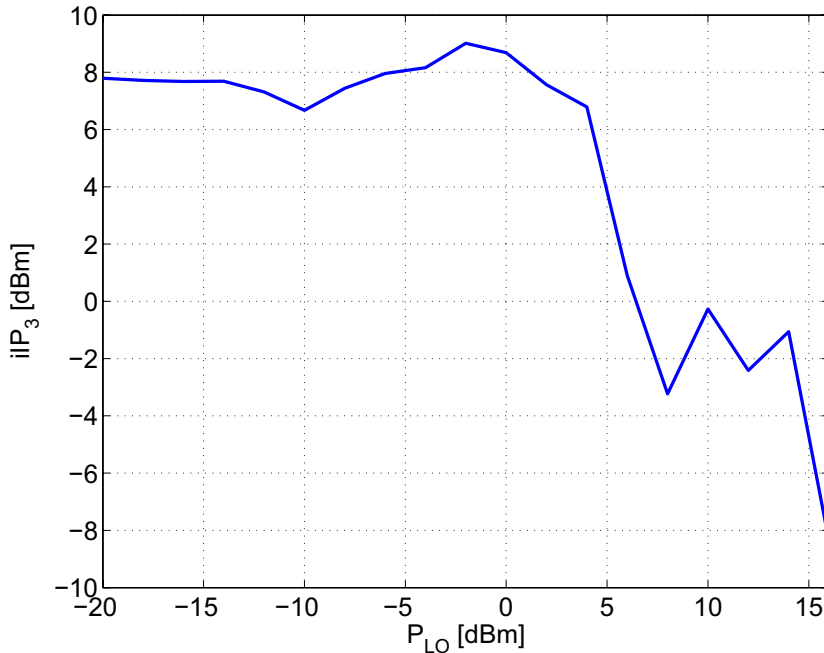


FIGURE 4.11: Dependence of the third-order intercept point on the LO power. The optimum value for the LO power level is -2 dBm.

order nonlinearities only. The mixer presented in this work cannot be classified as weakly nonlinear, thus higher-order nonlinearities must be included. Figure 4.12 shows the simulated 1 dB compression point of the presented mixer. The simulated input-referred 1 dB compression point is -3 dBm.

4.2.2 Noise

Noise in general refers to every spectral component that is not part of the signal containing the desired information. The sources of noise can be random or deterministic. On the one hand, noise contributors may be signals from other transmitters. Their operational frequency is not necessarily the same as the received signal. Also signals that couple to the input via the substrate are regarded as this type of noise. On the other hand, random fluctuations of the charge carriers (thermal or Johnson noise), or noise arising from the discrete nature of the electrons (shot noise), contribute to the noise floor. In this work, the impact of random noise is treated.

Noise Sources

There are different mechanisms in electric circuits that result in noise. The most important ones are summarized briefly:

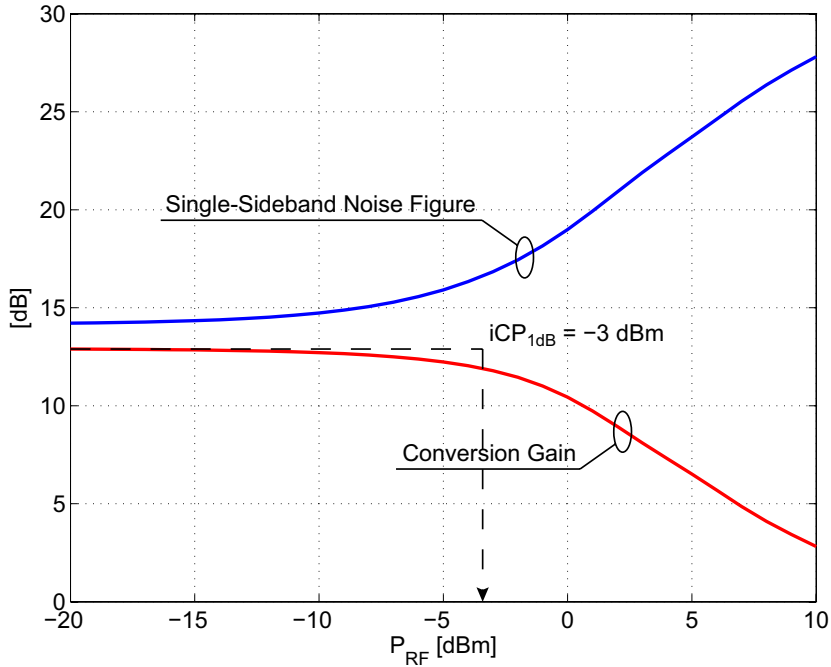


FIGURE 4.12: Simulation of the input referred 1dB gain compression point. The single-sideband noise figure versus applied RF power is also shown. $f_{LO} = 76.5$ GHz, $f_{IF} = 10$ MHz.

Thermal noise (Johnson noise, Nyquist noise): The movement of electric charges in a conductor exhibits statistical fluctuations due to thermal issues. This causes random fluctuations in the current and the voltage across the conductor, which is called thermal noise. This type of noise was measured first by J.B. Johnson [Johnson 28] for different types and values of resistors and at various temperatures. Shortly after these experiments, theoretical work by H. Nyquist [Nyquist 28] explained the experimental results.

The mathematical description of thermal noise is given by the variance of the noise voltage. It is equal to the root mean square of the noise voltage, \bar{v}_n^2 , which is

$$\bar{v}_n^2 = 4k_B TRB \quad [V^2]. \quad (4.30)$$

In this equation, k_B denotes Boltzmann's constant ($k_B = 1.38 \times 10^{-23}$ J / K), T is the temperature (in K), R is the value of the resistor (in Ω), and the bandwidth is B (in Hz). The spectral representation of this equation is frequency independent, i.e. it is white noise⁵.

Shot noise The granular structure of electric current is the source of shot noise.

⁵In fact, equation (4.30) is an approximation that must be extended by the Planck factor for frequencies in the THz range [Reisch 02]. The error in \bar{v}_n^2 assuming independence of frequency is only $\bar{v}_n^2 \cdot 8 \times 10^{-3}$ at an operating frequency of 100 GHz. Therefore, thermal noise is assumed white.

Whenever a potential barrier is present, e.g. in the base-emitter junction of a bipolar transistor, charge carriers pass this barrier depending on their kinetic energy. The energy is statistically distributed, which results in variations of the current with the mean value equal to the direct current, I_{DC} . The shot noise associated with the base current results from the injection of holes into the emitter, and the shot noise associated with the collector current from the injection of electrons into the base. The shot noise is quantified by the root mean square of the noise current. It is given by [Müller 89, Reisch 02]

$$\bar{i}_n^2 = 2qI_{\text{DC}}B \quad [\text{A}^2]. \quad (4.31)$$

The charge of a single electron is $q = 1.602 \times 10^{-19}$ As, and the mean (or DC) current is given by I_{DC} . The bandwidth is denoted B . The spectral characteristic of shot noise is white.

Shot noise in a bipolar transistor is caused mainly by the potential barrier of the base-emitter junction [Gilbert 06]. This can be illustrated by comparing the transistor with a vacuum diode, where the electrons need sufficiently high kinetic energy to leave the cathode. Regarding the base-collector junction of a bipolar transistor, the transition of electrons from the base to the collector is a drift process [Niu 05]. Therefore, no additional shot noise is introduced. The origin of the shot noise in the collector current is to be found in the emitter base junction.

1/f noise The spectral behavior of this type of noise is dependent on the frequency by $1/f$. Thus, it is dominant at very low frequencies. The frequency where $1/f$ noise becomes larger than the frequency-independent noise is marked by the corner frequency f_c . The corner frequency is dependent on the type of device and on the current density the device is operated at. Published values for f_c range from a few Hertz, e.g. for some bipolar transistors, up to the GHz range, e.g. for MOS transistors. The causes for this kind of noise are various [Müller 89]. Impurities in the crystal lattice of a semiconductor result in $1/f$ noise, for example. Also traps for electrons and holes, located at the surface of the transistor's base, are the cause for $1/f$ noise. The spectral representation $S(f)$ of this type of noise is generally given by

$$S(f) = \frac{\text{const.}}{|f|^\gamma}, \quad (4.32)$$

where const. refers to an empirical parameter that is specific to the device, and γ is usually close to unity.

Generation / Recombination noise The number of electrons and holes in a semiconductor varies stochastically due to generation and recombination. This leads to fluctuations in the base current and, subsequently, in the collector current. The spectrum of this type of noise is given by [Müller 89,

Reisch 02]

$$S_{\Delta n}(f) = \frac{2(G + R)\tau^2}{1 + (2\pi f\tau)^2} \frac{1}{V}, \quad (4.33)$$

where G and R are the generation and recombination rates, respectively, V is the semiconductor volume, and τ is the relaxation time. Generation and recombination processes contribute to the generated noise in equal parts.

Avalanche noise When a large voltage is applied to a junction of a transistor, for example the collector–base junction, charge carriers gather sufficient energy to tear out other carriers through physical impact (“Impact Ionization”). This is a statistical process, so the resulting current has random behavior. The current produced by this mechanism is therefore regarded as noise. Noise current due to avalanche multiplication can be much higher than shot noise current. The electron current shot noise from the emitter base junction is also amplified by the avalanche process since it traverses the large electric field, generating additional electron – hole pairs. Similar to shot noise, avalanche noise has a white spectrum.

Burst noise Also known as “Popcorn noise”, burst noise is characterized by its multimodal amplitude distribution. This means that the noise amplitude switches between two or more discrete values at random times. The transitions happen at intervals in the audio range, e.g. 100 ms, causing a “popping” sound in an audio amplifier for example.

Device impurities are the cause for burst noise. Thus, it can rarely be observed in modern integrated circuits.

Noise Figure Definition

An important measure for the quality of a signal at any stage in a receiver chain is the ratio of the signal power and the noise power,

$$\text{SNR}_{\text{lin}} = \frac{\text{Signal power}}{\text{Noise power}} = \frac{P_{\text{S,lin}}}{P_{\text{N,lin}}}. \quad (4.34)$$

where SNR_{lin} denotes the linear Signal-to-Noise ratio. The quantities $P_{\text{S,lin}}$ and $P_{\text{N,lin}}$ refer to the available signal power and the available noise power on a linear scale. Available power is the power level that can be delivered to a power matched load. It is therefore independent of the impedance of the circuit it is actually attached to.

It is more convenient to define the SNR using logarithmic scales,

$$\text{SNR} = 10 \log_{10} \frac{P_{\text{S,lin}}}{P_{\text{N,lin}}} = P_{\text{S}} [\text{dB}] - P_{\text{N}} [\text{dB}], \quad (4.35)$$

where $P_{\text{S}} [\text{dB}]$ and $P_{\text{N}} [\text{dB}]$ are the available signal and available noise power on a logarithmic dB scale, respectively.

Each building block in a receiver changes the signal to noise ratio. The absolute value of both signal power and noise power at the input are amplified by the block's gain or attenuated by its loss. In addition, the noise that is inherent in each device is added. The amount of noise power added to the noise floor at the input is quantified by the noise factor.

The noise factor of any two-port is defined as

$$F = \frac{\text{SNR}_{\text{In,lin}}}{\text{SNR}_{\text{Out,lin}}} \quad (4.36)$$

$$= \frac{P_{\text{S,In}}}{P_{\text{N,In}}} \cdot \frac{P_{\text{N,Out}}}{P_{\text{S,Out}}} \quad (4.37)$$

$$= \frac{P_{\text{S,In}} \cdot (P_{\text{N,In}}G_{\text{av}} + P_{\text{N,DUT}})}{P_{\text{N,In}} \cdot G_{\text{av}}P_{\text{S,In}}} \quad (4.38)$$

$$= \frac{P_{\text{N,In}}G_{\text{av}} + P_{\text{N,DUT}}}{P_{\text{N,In}}G_{\text{av}}} \quad (4.39)$$

$$= \frac{kT_0BG_{\text{av}} + P_{\text{N,DUT}}}{kT_0BG_{\text{av}}}. \quad (4.40)$$

In this equation, G_{av} is the available gain, B is the bandwidth, and $P_{\text{N,DUT}}$ is the noise that is added by the device under test (DUT). This definition is independent of the input or output signal. It only accounts for the amplified noise at the input (kT_0) and the inherent noise of the DUT. The temperature T_0 is by definition 290 K. Another way of defining the noise factor is by using the concept of noise temperatures, resulting in [Agilent Tech 07,a]

$$F = 1 + \frac{T_{\text{DUT}}}{T_0}. \quad (4.41)$$

In this equation, T_{DUT} is the equivalent noise temperature of the DUT.

The more common measure for the noise of a DUT is the logarithm of the noise factor, being

$$\text{NF} = 10 \log_{10} F \quad [\text{dB}]. \quad (4.42)$$

The quantity NF is called noise figure. It is a direct measure for the degradation of the SNR. The changes in SNR due to the gain and the noise figure are illustrated in figure 4.13.

Further definitions need to be introduced in order to define the noise figure of frequency converting devices. A mixer translates all frequency components from the RF frequency range to the IF frequency range. In addition to the wanted RF signal, noise from both the upper (USB) as well as the lower (LSB) sideband is translated to the IF. The spectral representation of the components contributing to the IF output of the mixer is depicted in figure 4.14.

In a radar system, the RF signal resides only in one sideband. The corresponding single sideband noise factor is derived from equation (4.40), yielding

$$F_{\text{SSB}} = \frac{kT_0B_{\text{LSB}}G_{\text{av,LSB}} + kT_0B_{\text{USB}}G_{\text{av,USB}} + P_{\text{N,DUT}}}{kT_0B_{\text{USB}}G_{\text{av,USB}}}, \quad (4.43)$$

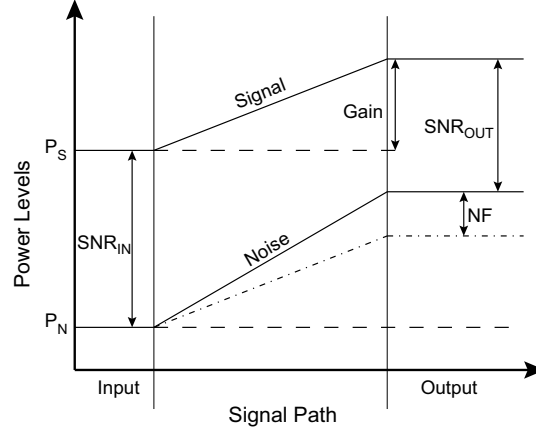


FIGURE 4.13: Definition of the noise figure and gain of any device. The dash-dotted line refers to the amplified input noise.

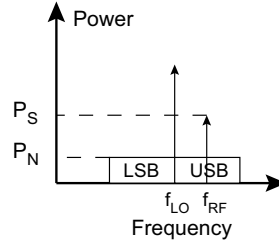


FIGURE 4.14: Spectral components contributing to the noise figure of a mixer.
 $f_{RF} = f_{LO} + f_{IF}$

where the RF signal is located in the upper sideband in this case. Equation (4.43) applies for unequal receiver bandwidths and conversion gains in the USB and the LSB, denoted $B_{USB,LSB}$ and $G_{av,USB/LSB}$, respectively. The single-sideband noise figure is defined by

$$NF_{SSB} = 10 \log_{10} F_{SSB}. \quad (4.44)$$

If the RF signal is located in both sidebands, the double sideband noise figure is defined by

$$F_{DSB} = \frac{kT_0 B_{LSB} G_{av,LSB} + kT_0 B_{USB} G_{av,USB} + P_{N,DUT}}{kT_0 B_{USB} G_{av,USB} + kT_0 B_{LSB} G_{av,LSB}}. \quad (4.45)$$

and

$$NF_{DSB} = 10 \log_{10} F_{DSB}. \quad (4.46)$$

For equal receiver bandwidths in the USB and the LSB, equation (4.43) and equation (4.45) are related

$$F_{SSB} = F_{DSB} \left(1 + \frac{G_{av,LSB}}{G_{av,USB}} \right) \quad (4.47)$$

for the RF signal located in the USB. If the RF signal is located in the LSB, the expression in brackets reads $(1 + \frac{G_{av,USB}}{G_{av,LSB}})$. In the case of equal gains, equation (4.47) states that F_{SSB} is two times larger than F_{DSB} . In a logarithmic scale, this yields $NF_{SSB} = NF_{DSB} + 3$ dB. This assumption is justified for the measurements presented later in this chapter. Since the IF is close to DC, the variations in conversion gain are negligible.

Noise in Mixers

The frequency bands where mixers collect RF power lie in various ranges. Noise in all of these bands contributes to the total noise power at the output of the mixer. These contributions are

- Noise at the RF frequency (including the image frequency),
- Noise at the IF frequency,
- Noise at multiples of the LO frequency.

The noise power of these components may only be superimposed if their power spectra are uncorrelated [Weinrichter 91]. This requirement is not fulfilled by noise components that are translated to the IF from multiples of the LO frequency. These components have cyclostationary power spectral densities, thus correlation exists between any two frequency components that are separated by multiples of the LO frequency [Hull 93]. A cyclostationary process is converted to a stationary process when it is filtered. The requirement for the filter is that the bandwidth is smaller than the LO frequency. This is the case in most mixers, since an IF filter usually follows the mixer. Frequency components at multiples of the LO frequency are additionally attenuated by the active stages since the gain of the latter is quite low. For the mixer presented in this work, the second harmonic of the LO frequency is at 154 GHz. The gain of the transconductance stages at this frequency is small.

The total output noise power of a mixer depends mainly on two factors: The noise properties of the amplifier stage (the RF transistors), and the contribution from the switches (the LO quad).

The main noise contributors of the RF amplifier are the thermal noise of the base resistance and the shot noise generated in the base-emitter junction by the collector current. If resistive degeneration is used, also the thermal noise introduced by this resistor has a large contribution.

In the IF section, the load resistors (R_L in figure 4.2) contribute thermal noise that enters into the output noise voltage independently of the operating state of the mixer.

The switching transistors of the mixer determine the transfer function of most of the noise contributors to the IF output. The individual contribution of each

noise component changes with the power that is fed to the switching quad. This procedure is illustrated in figure 4.15, where the total output noise power referred to $1\ \Omega$ in 1 Hz bandwidth of the mixer depicted in figure 4.2 is plotted versus the applied LO power level. The relative contributions to the total noise power are

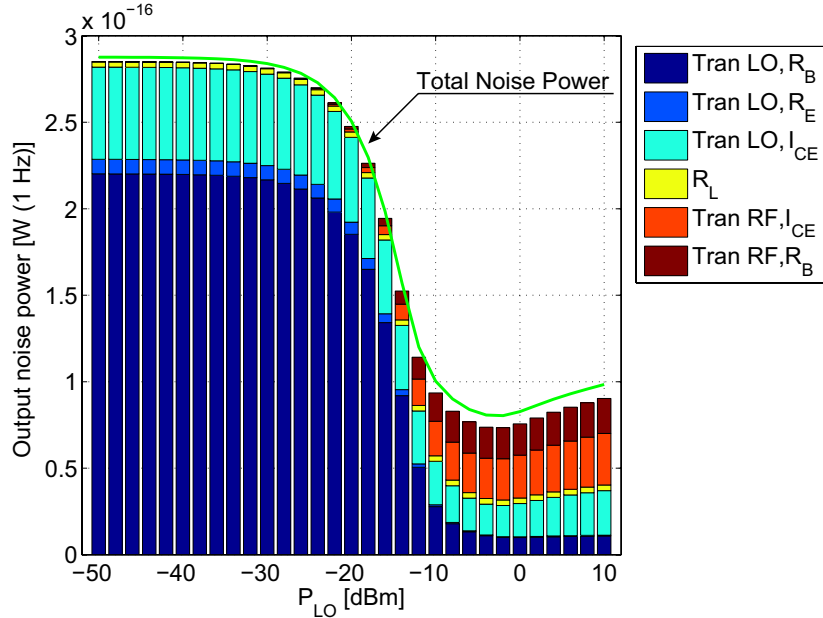


FIGURE 4.15: Absolute noise power referred to $1\ \Omega$ (green line) in 1 Hz bandwidth at the IF port of the mixer depicted in figure 4.2 versus LO power. The abbreviations 'Tran LO' and 'Tran RF' refer to noise from the LO and the RF transistors. Noise from the base resistances is denoted R_B , noise from the emitter resistance R_E . Shot noise due to the collector current is labeled I_{CE} . Contributions from the load resistors are marked R_L .

shown in figure 4.16. Under regular operating conditions, that means the LO power set to an appropriate level, roughly 55% of the total noise power results from shot noise due to the collector currents. The thermal noise of the base and the emitter resistances adds approximately 30%.

The noise at low power levels is dominated by the properties of the transistors in the switching quad. The two differential pairs operate in a linear mode, thus the primary contributor to the output is the amplified thermal noise of the base resistances, R_B . The shot noise due to the base-emitter junction of the LO transistors also adds substantial noise power. The largest values come from the shot noise associated with the collector current.

When the LO transistors of the mixer start to act as switches, which happens at an LO power level of -20 dBm, their impact on the total output noise power gradually decreases. The largest contributor at low LO power levels, which is the noise of the base resistances of the LO transistors, drops from 77% to 11%. Even if the LO transistors switch instantaneously, noise from the base resistances and the shot

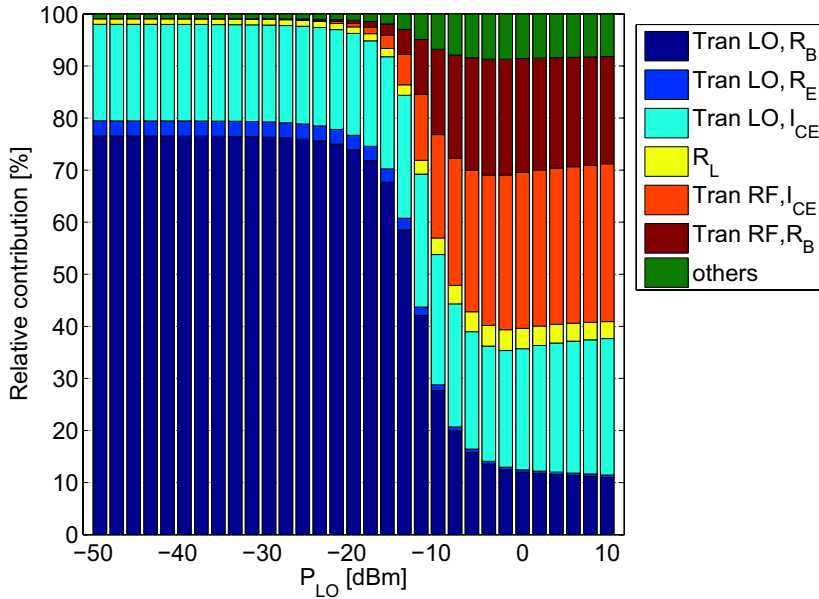


FIGURE 4.16: Largest noise contributors to the total IF noise power depending on the LO power level. Refer to figure 4.15 for the explanation of the entries in the legend. The simulated mixer is the device shown in figure 4.2.

noise contribute to the output. This is a result of the non-negligible impedance at the emitters of the differential pairs, consisting of the collector–substrate and the collector–base capacitance of the RF transistors, and of the base–emitter capacitance of the LO transistors. This non-negligible impedance provides a low ohmic path to ground, since the RF transistors are usually designed with a large size to minimize their thermal noise. For non-ideal switching, the low impedance path to ground is provided by the input impedance seen into the emitter of the second transistor in the differential pair. The absolute value of this impedance is approximately $1/g_m$, thus it is small compared to the impedance associated with the RF pair [Razavi 98]. As a result, even if the effect of the capacitance at the common emitter node is reduced, for example by the use of an inductor, the low impedance path to ground is still present. The impact of the low impedance path to ground via $1/g_m$ can be reduced by increasing the LO voltage swing. This reduces the time during which both transistors are simultaneously ”on”.

With the onset of the switching action of the LO transistors, the noise contribution of the RF transistors rises. At a certain power level, the behavior of the RF transistors dominates the overall performance. Since the RF transistors are optimized for low noise, the total IF output noise power is much less than at low LO power levels. A minimum in noise power is reached at an LO power level of -2 dBm. Beyond this point, the noise power slowly increases. The main cause for this behavior is the DC current through the RF and the LO transistors. It is varied by charge storage in the collector-substrate capacitance, and by current

injection through the base–emitter capacitance of the LO transistors.

A dynamic effect that comes from the modulation of the base–emitter voltage of the RF transistors also changes the DC current. The potential at the emitter of the LO transistors varies with twice the LO frequency due to the rectifying property of the differential pair. As a result, also the base potential of the RF transistor (through C_{BC}) and, subsequently, the base emitter voltage varies, which changes the collector current. Therefore, the rms value rises, which results in additional shot noise. Simulations show that the effects described above rise the rms current per branch from 11 mA at low LO power levels up to 15.5 mA at +10 dBm.

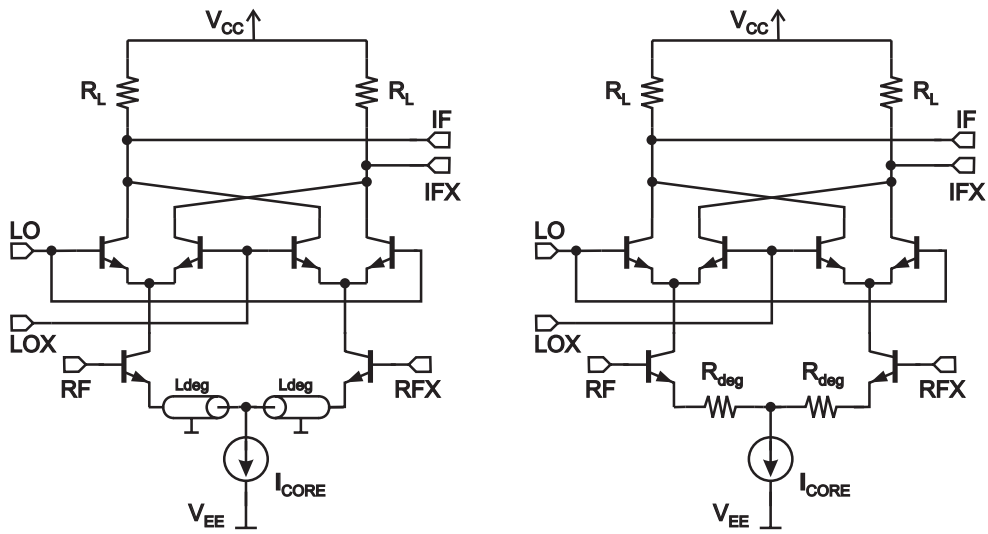
Figure 4.15 shows that the impact of the load resistor’s thermal noise remains unchanged. This is evident, since their transfer function to the output is the same for each operating state of the mixer.

Other contributors to the total noise power at the IF output result from high voltage effects in the LO transistors. Beyond the collector–emitter breakdown voltage of the transistor, the avalanche effect has an additional noise contribution. Although the device can sustain these voltage levels if the base is connected to a low impedance load, noise is generated due to the avalanche effect. This mechanism is not limited to voltage levels above the breakdown voltage [Greenberg 03]. Noise contributors due to this effect are not depicted in figure 4.15 and figure 4.16 since they are not modeled in the used designkit.

Various differential circuit configurations for 77 GHz RF amplifiers were investigated regarding their noise behavior. They were incorporated in a Gilbert mixer to represent the target application. The circuit configurations are a differential common-emitter stage with inductive and resistive degeneration and a differential common-base stage. These configurations are depicted in figure 4.17. The inductors in figure 4.17(a) are implemented as transmission lines that show inductive behavior.

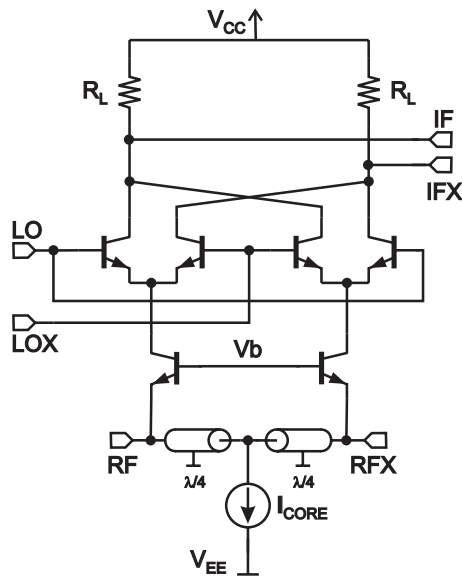
The simulation results of the single-sideband noise figure and the conversion gain are shown in figure 4.18. They are plotted versus the input RF power (in dBm). The LO frequency is set to 77 GHz, the IF frequency is 100 MHz. The LO power is +5 dBm. The RF as well as the LO signals are applied differentially using ideal baluns.

The emitter-coupled pair with inductive degeneration is superior to the resistively degenerated emitter-coupled pair by roughly 2 dB and to the common base stage by roughly 4 dB in terms of noise performance. The differences in conversion gain are at most 1.5 dB, which partly contributes to the differences in noise figure. Since the three configurations exhibit identical behavior regarding the linearity ($P_{in,1dB} = -3$ dBm), the comparison is meaningful.



(a) Inductive degeneration (L_{deg}).

(b) Resistive degeneration (R_{deg}).



(c) Common-base differential pair.

FIGURE 4.17: Investigated mixer circuit configurations. (Biasing details are not shown.)

4.2.3 Stability

The stability of a mixer is a critical point in the design process. Since a differential design is used, the stability in terms of differential as well as common mode behavior must be investigated. Classic stability criteria that can be used for two

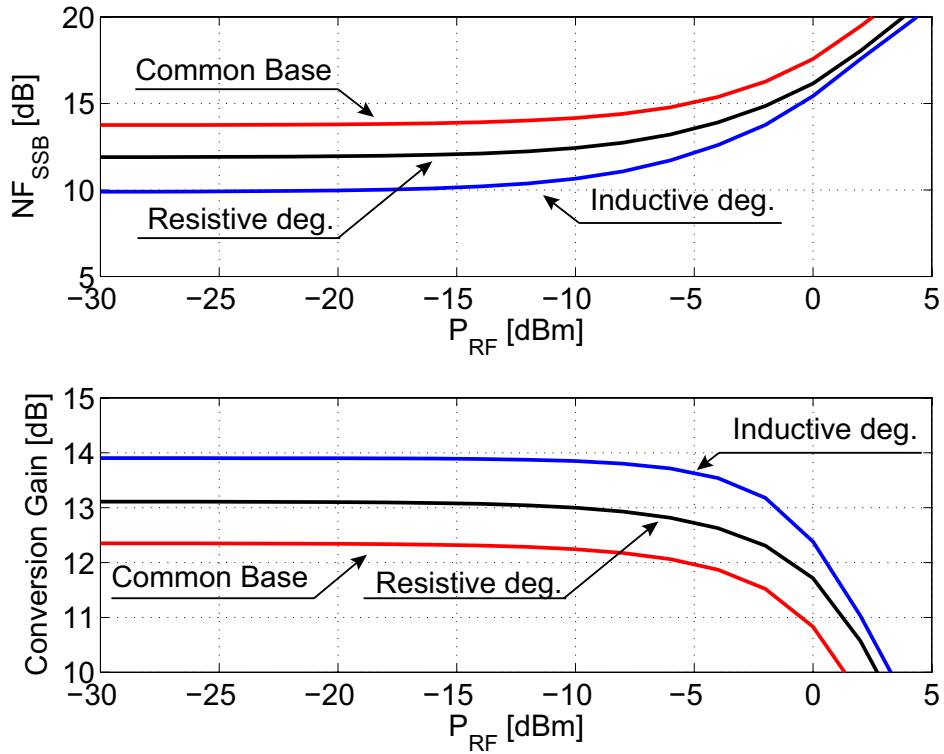


FIGURE 4.18: Comparison of the single-sideband noise figure and the conversion gain of the emitter-coupled pair with inductive and resistive degeneration and the common-base stage. All configurations exhibit the same 1 dB compression point.

port networks, like Rollet’s stability factor and the stability measure, cannot be applied to mixers directly since these methods are based upon linear two ports.

Any circuit is potentially unstable when it does not act as a passive load, that is, when the magnitude of the reflection coefficient at any port is larger than ”1”. This is equivalent to a negative input resistance [Pojar 01]. Similar to oscillators, two conditions must be fulfilled for instability,

- the losses in the resonator must be compensated by the negative resistance of the active device (amplitude condition), and
- the phase shift caused by the resonator and the phase shift caused by the active device must add to a multiple of 2π (phase condition).

For the circuit presented in this work, the resonator consists of the biasing circuit, the balun, and parasitics. Especially the parasitics complicate the investigation of the resonator’s phase. In addition, transmission lines are used extensively throughout the design, so broadband models are necessary to ensure the correct determination of the phase. Therefore, a better way to prevent instability is to

ensure that the input resistance of the circuit remains positive over the whole frequency range which is equal to the magnitude of the input reflection coefficient being smaller than "1".

The differential input impedance of the mixer's differential ports is determined in order to investigate the differential mode stability. Since the large-signal operation of the LO transistors changes the load of the RF differential pair, a harmonic balance analysis yields the most realistic results. The real part of the differential input impedance of the RF port of mixers employing three different RF amplifier configurations is plotted in figure 4.19. The LO power level is +5 dBm. The different amplifiers are depicted in figure 4.17. This plot shows only the real part of the impedance since it primarily determines the stability. The difference in

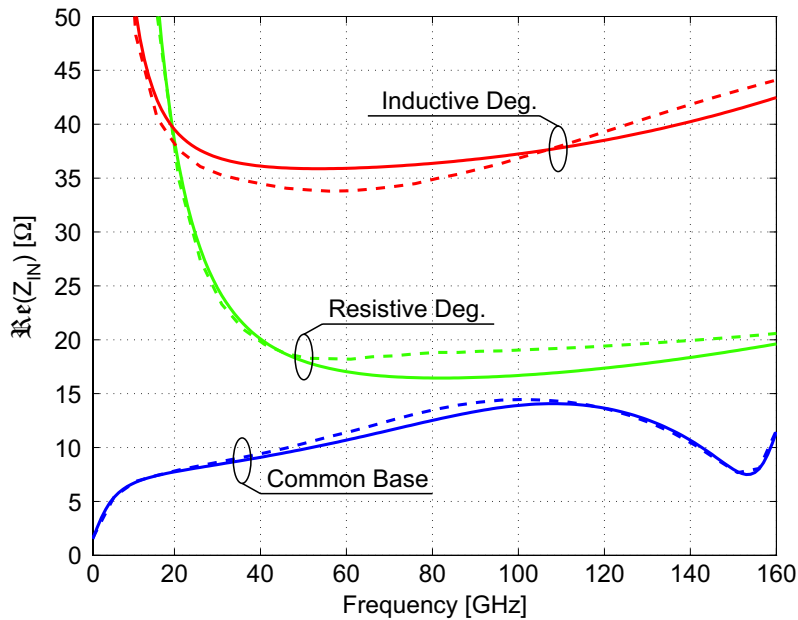


FIGURE 4.19: Simulated (AC – solid line, HB – dashed line) real part of the differential impedance for different circuit configurations (emitter-coupled pair with inductive and resistive degeneration, and differential common base stage). $P_{LO} = +5$ dBm for the HB simulation.

input impedance between small-signal and large-signal analysis is small for the three configurations. The differential input impedance of the LO port is shown in figure 4.20. Figures 4.19 and 4.20 indicate that differential mode instability is unlikely to occur since the real part of the input impedance is far away from becoming negative.

The common mode stability can also be determined by checking the common mode input impedance. This is done by applying the same signal to both pins of the differential amplifier and calculating the input impedance or, equivalently, the input reflection coefficient. This method results in equal source impedances at both inputs of the differential amplifier. An LC balun does not provide equal

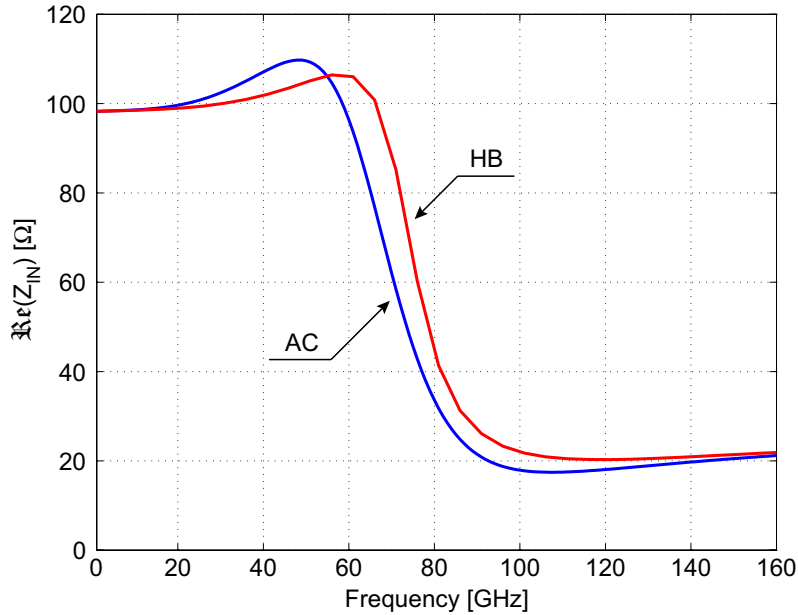


FIGURE 4.20: Simulated (AC and HB) differential input impedance at the LO port ($P_{LO} = +5$ dBm). The impedance is unaffected by the topology of the RF pair.

impedances to these inputs over the whole frequency range. Thus, it is necessary to find the source and load impedances where the differential amplifier is potentially unstable to ensure unconditional stability.

The input impedances of any network depend in general upon the properties of the network itself as well as upon the loads attached to the other ports. Similarly, the input reflection coefficients also depend on the loads. Since the representation by impedances and reflection coefficients are equivalent but the use of reflection coefficients is more convenient, the latter will be used from now on. This theory is only valid for linear and weakly nonlinear systems.

For a two port network, unconditional stability is given for [Gonzales 97]

$$|\Gamma_S| < 1, \quad (4.48)$$

$$|\Gamma_L| < 1, \quad (4.49)$$

$$|\Gamma_{IN}| = \left| S_{11} + \frac{S_{12}S_{21}\Gamma_L}{1 - S_{22}\Gamma_L} \right| < 1, \quad (4.50)$$

$$|\Gamma_{OUT}| = \left| S_{22} + \frac{S_{12}S_{21}\Gamma_S}{1 - S_{11}\Gamma_S} \right| < 1, \quad (4.51)$$

where Γ_S and Γ_L are the source and the load reflection coefficients, respectively. The input and output reflection coefficients of the two port network are represented by Γ_{IN} and Γ_{OUT} . The coefficients S_{ik} are the elements of the S -matrix.

The region where conditions 4.48 – 4.51 are fulfilled can be determined by solving

these equations graphically. The solutions are the stability circles [Gonzales 97]. They represent the regions where the circuit is potentially unstable. These considerations apply to linear or weakly nonlinear systems.

For unconditional stability, only the minimum distance of the stability circle from the $\rho = 0$ point in the Smith chart needs to be known. This distance is given by the μ factor [Edwards 92],

$$\mu = \frac{1 - |S_{11}|^2}{|S_{22} - S_{11}^* \cdot \Delta| + |S_{12}S_{21}|}, \quad (4.52)$$

where the asterisk stands for the complex conjugate, and Δ is the determinant of the S -matrix, $\Delta = |S_{11}S_{22} - S_{12}S_{21}|$. Unconditional stability is given when the stability circles are outside the $\rho = 1$ circle in the Smith chart, which is equivalent to $\mu > 1$.

Equation (4.52) is used to determine the common mode stability of the LO as well as the RF port of the mixer. Referring to figure 4.19 and figure 4.20, the deviations between small-signal and large-signal operation regarding the input impedance are not negligible. Therefore, the results from both analyses are significant for the stability.

Figure 4.21 shows the common mode μ factor of the LO port for small-signal and large-signal excitation. Large-signal excitation makes the circuit more stable at

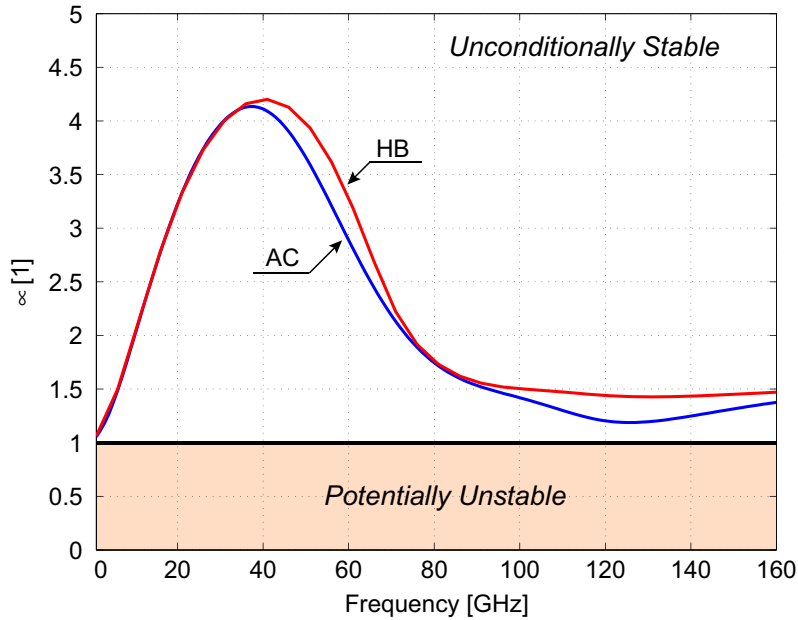


FIGURE 4.21: Simulated common mode μ factor for the LO port of the mixer ($P_{LO} = +5$ dBm). For unconditional stability, μ must be larger than 1. The μ factor of the LO port is independent of the RF section of the mixer.

higher frequencies. This is explained by the dynamic behavior of the emitter fol-

lowers, refer to section 4.1.2. Hence, the LO section of the mixer is unconditionally stable.

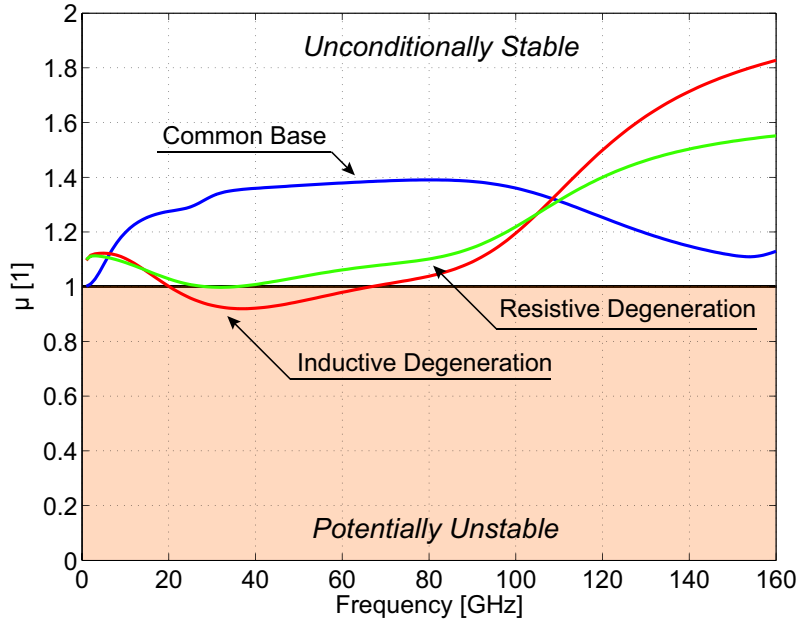


FIGURE 4.22: Simulated (AC) common mode μ factor of the RF port for different circuit configurations (Emitter-coupled pair with inductive and resistive degeneration, and differential common-base stage).

A comparison of the three RF circuit configurations from figure 4.17 regarding their common mode stability is depicted in figure 4.22. While the emitter-coupled pair with inductive degeneration shows the best performance in terms of noise behavior, it is potentially unstable regarding common mode stability. Also the resistively degenerated emitter-coupled pair suffers from stability issues. From the stability point of view, the differential common-base stage is the most robust configuration regarding source impedance variations (the output impedance of the balun) and parasitics.

4.2.4 Local Oscillator Amplitude Noise Suppression

The LO signal usually has non-ideal behavior, described by the phase noise and the amplitude noise. Normally, the spectral density of the phase noise is larger than the spectral density of the amplitude noise in a free running oscillator, and the amplitude noise is neglected. When the phase noise of the oscillator is reduced by a phase-locked loop, the amplitude noise can become dominant.

Since amplitude noise appears like a double-sideband amplitude modulation at the LO, it is down-converted to the IF of the mixer like an RF signal. Therefore, this type of noise is also called AM noise.

The LO transistors of the mixer are operated as switches. As long as the LO power is at a level where variations do not affect the noise figure and the gain, the impact of amplitude noise on the IF output spectrum is quite low. From simulation, the suppression of LO AM components at the IF is 38.8 dB in the target frequency range.

4.2.5 Local Oscillator Leakage

Parasitic paths cause the LO signal to couple to the RF port [Razavi 97]. These paths include substrate coupling or coupling via bond wires for mounted chips. Also paths arising from the system configuration result in a parasitic LO signal at the RF port. In the system example in section 2.2, a mixer is employed in a ratrace coupler which yields a system where one antenna can be used for transmitting and receiving without additional components. The non-ideality of the integrated coupler, described in section 2.2, results in LO components that can be larger than the LO signal reflected from mismatches at the antenna.

Additionally, asymmetries in the layout and in the device fabrication add to parasitic LO coupling. This results in a DC offset at the IF output, and subsequently in noise figure and conversion gain degradation. The DC offset is shown in figure 4.23. The impact of the LO leakage on the noise figure and the conversion gain is depicted in figure 4.24. A cancelation of the DC offset at the IF port does

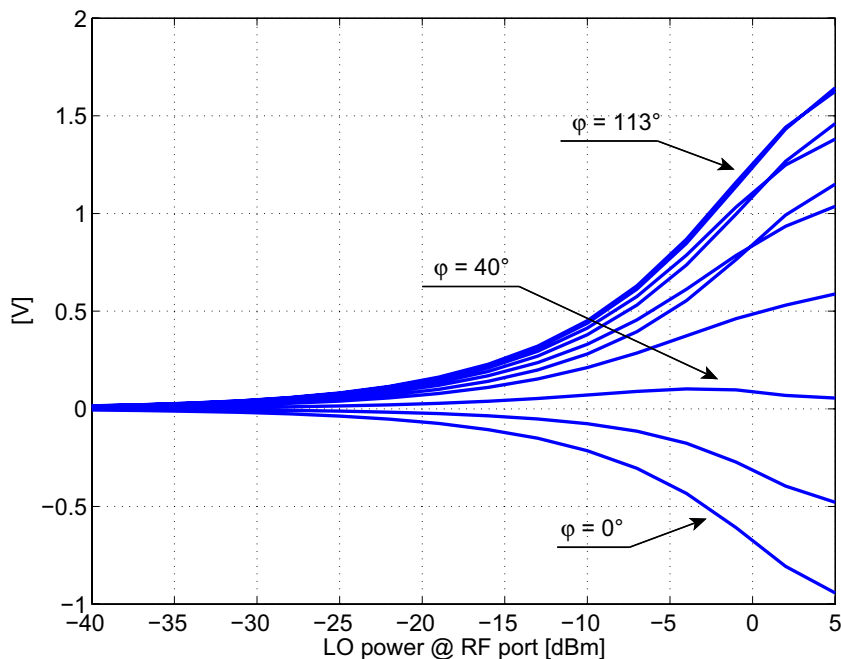


FIGURE 4.23: Simulated DC offset due to LO leakage. The parameter φ gives the phase difference between the LO signal at the LO port and the parasitic LO signal at the RF port. $f_{LO} = 76.5$ GHz, $f_{IF} = 10$ MHz.

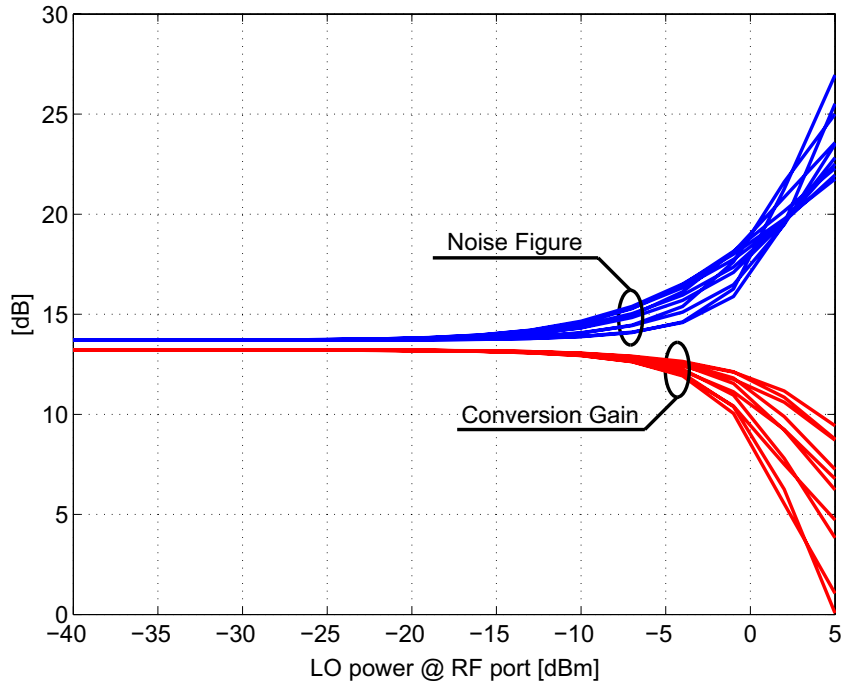


FIGURE 4.24: Simulated conversion gain and noise figure degradation due to LO leakage for different phase shifts between the LO signal at the LO port and the parasitic LO signal at the RF port. $f_{LO} = 76.5$ GHz, $f_{IF} = 10$ MHz.

not cancel the degradation in noise figure and conversion gain.

The figures also show the dependence on the phase of the LO signal coupled to the RF port. This is explained by the multiplication of two cosine signals, representing the local oscillator signal at the LO port (ω_{LO} and φ_{LO}), and the leaked LO signal at the RF port (ω_{LO} and $\varphi_{LO,par}$):

$$\begin{aligned} \cos(\omega_{LO}t + \varphi_{LO}) \cdot \cos(\omega_{LO}t + \varphi_{LO,par}) = \\ \cos((\omega_{LO} + \omega_{LO})t + \varphi_{LO} + \varphi_{LO,par}) + \cos((\omega_{LO} - \omega_{LO})t + \varphi_{LO} - \varphi_{LO,par}), \end{aligned} \quad (4.53)$$

which, after low-pass filtering, results in

$$\cos(\varphi_{LO} - \varphi_{LO,par}). \quad (4.54)$$

The DC offset is largest at a phase difference $\varphi_{LO} - \varphi_{LO,par} = 113^\circ$, which is also the worst phase regarding the noise figure and the conversion gain. As expected, the least degradation of those two parameters occurs where also the DC offset is lowest, which is at a phase difference of 40° . Ideally, this value should be 0° , but the circuit elements that precede the point where the mixing occurs introduce different phase shifts at the RF and the LO branch.

A DC offset between the two IF outputs can be caused by device mismatches in the mixer, too [Kivekäs 01]. These mismatches include transistor size and resistor

tolerances. They cannot be overcome since they are inherent in the production process, but their effect is usually very low (a few millivolts).

The leakage of the local oscillator signal to the IF port can result in unwanted radiations through the bond wires that connect the IF pads. A suppression of this leakage path is inherent when a double balanced mixer type is used, as described in section 4.1. Additionally, an RC low pass consisting of the load resistors ($R_L = 100 \Omega$) and large capacitors (280 fF) is included to further reduce LO to IF leakage.

4.2.6 Sensitivity Analysis

Process variations have an impact on the transistor parameters. This results in variations of the mixer performance. The linear dependence of the single-sideband noise factor, the conversion gain, and the RF and LO matching of the mixer from section 4.1.1 on linear variations in the base resistance R_B , the base-collector capacitance C_{BC} , and the forward transit time τ_F are depicted in figure 4.25. The

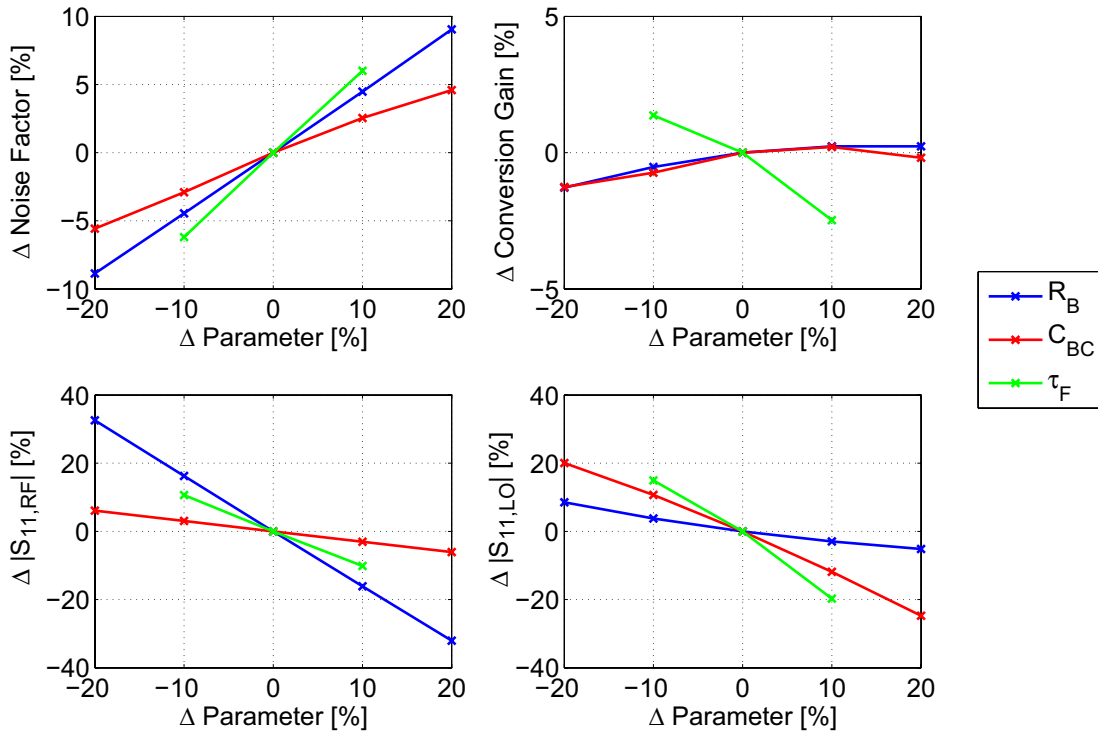


FIGURE 4.25: Simulated sensitivity on a linear scale of single-sideband noise factor, conversion gain, and matching of the RF and the LO port ($|S_{11,RF}|$ and $|S_{11,LO}|$) on linear variations in the transistor's base resistance R_B , base-collector capacitance C_{BC} , and forward transit time τ_F . $P_{LO} = +5$ dBm, $f_{LO} = 77$ GHz, $f_{IF} = 10$ MHz

variation ranges of $\pm 20\%$ for R_B and C_{BC} and $\pm 10\%$ for τ_F are chosen for illustration purposes. The real values are company confidential. Additionally, the effects of the parameter variations are investigated without taking any correlations into account. The largest variation of the noise figure comes from τ_F , which results from the noise figure's dependence on the switching speed of the current commutating transistors (see section 4.2.2). Faster transistors result in faster switching, decreasing the noise figure. The base resistance R_B is the second largest contributor to noise figure variations because of the amplified thermal noise. Larger resistances exhibit higher noise, which also increases the noise figure. A decrease in C_{BC} lowers the noise figure due to the reduced parasitic capacitances at the collectors of the RF transistors (see section 4.2.2). The associated changes of the noise figure due to changes in the matching are not deembedded from these results.

The conversion gain remains almost unaffected by the variations of the three parameters. The strongest impact comes from the speed of the transistors, but the overall variations are lower than $\pm 3\%$. The conversion gain variations result mainly from variations in the input matching of the RF port.

The input matching at the RF port is strongly dependent on the base resistance R_B since this value enters directly into the input impedance of the core cell.

The input impedance of the LO buffer is high compared to the absolute value of R_B . Variations in R_B appear in series to this high impedance so they have a minor impact on the input impedance and therefore on the LO matching ($\pm 5\%$). The C_{BC} of the emitter followers act as a shunt capacitors to V_{CC} . So their value determines the input impedance of the buffer directly. The impedance transformation process of the emitter follower is dependent on the current gain, thus changes in τ_F result in the largest variations of the input impedance and, therefore, in the matching.

4.3 Measurement Results

A photograph of the fabricated mixer chip is shown in figure 4.26. The LO input is on the left hand side, and the RF input on the right hand side. This is the largest possible separation of the two ports, which is important to decrease the parasitic coupling from the LO to the RF input. Especially when the chip is mounted, the mutual inductance of the bond wires results in unwanted emissions over the antenna on the one hand, and in blocking of the RF input on the other hand. Ground pads are placed to the left and the right of the signal pads. This enables to use Ground-Signal-Ground (GSG) probes when measuring the chip on-wafer. Probes with this configuration have a lower insertion loss than probes with single ground contacts (GS or SG configuration), increasing the accuracy of the measurement (see section 4.3.1). The differential output is taken from the pads labeled IF and IFX. The layout offers three pads to connect the positive

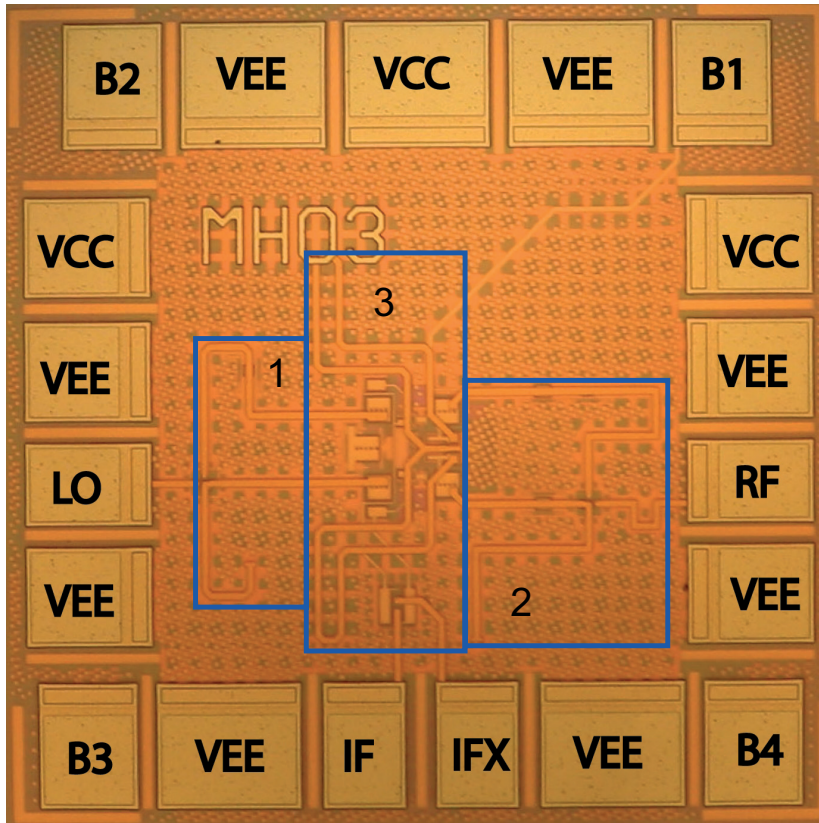


FIGURE 4.26: Die photograph of the highly linear mixer. Three components are marked: The LO balun (1), the RF balun (2), and the mixer core including the LO buffer (3). Die size is $700 \times 700 \mu\text{m}^2$. $V_{CC} = 5.5 \text{ V}$, $I_{EE} = 75 \text{ mA}$.

supply, labeled V_{CC} . The pad labeled B1 is connected to the tail current source of the mixer core cell. This enables an external control of the core current. The other three bias pads, B2-B4, are not connected.

Figure 4.27 shows an overview of the measurement setup for the noise figure and the conversion gain measurement. All measurements were done with probes. The power was also supplied via probes, except for the measurement of the matching. The on-wafer measurement setup for the determination of the noise figure and the conversion gain is depicted in figure 4.28(a). A detailed view of the probe connections is shown in figure 4.28(b). Here, the LO section is connected from the left hand side, while the RF connections are on the right hand side.

The setup consists of the following devices:

Noise figure meter HP's 8970B noise figure meter automatically measures the noise figure and the conversion gain of the mixer. The meter also acts as the system master, controlling the noise source and the synthesizer. It can measure down to 10 MHz. Its internal noise figure is 7 dB. It is capable of

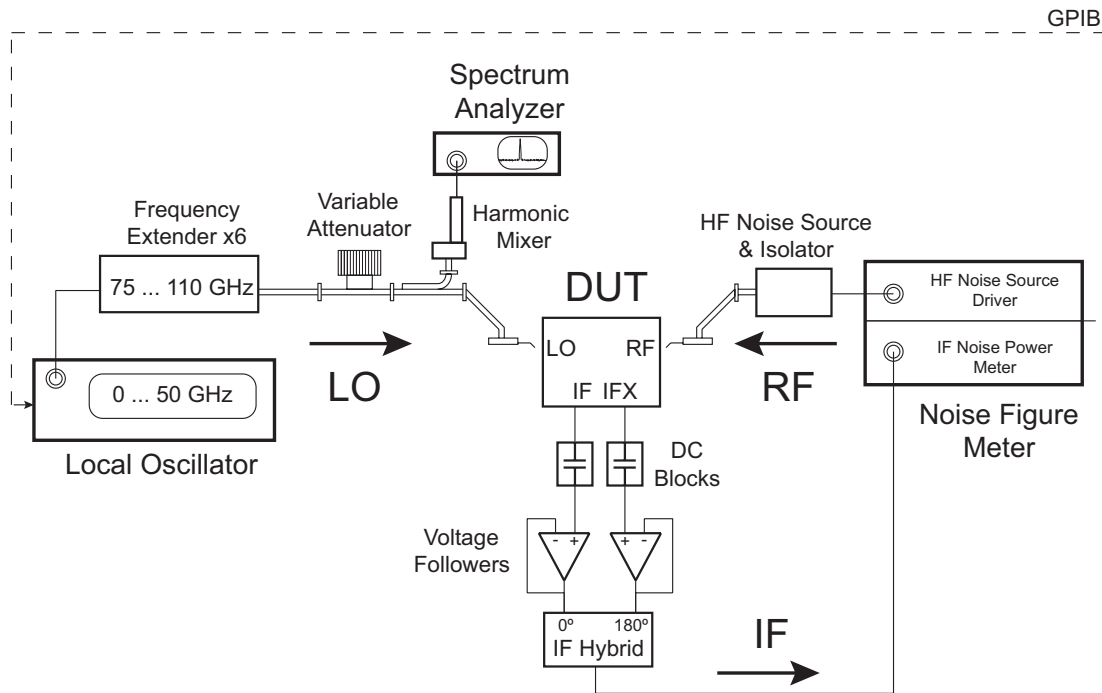


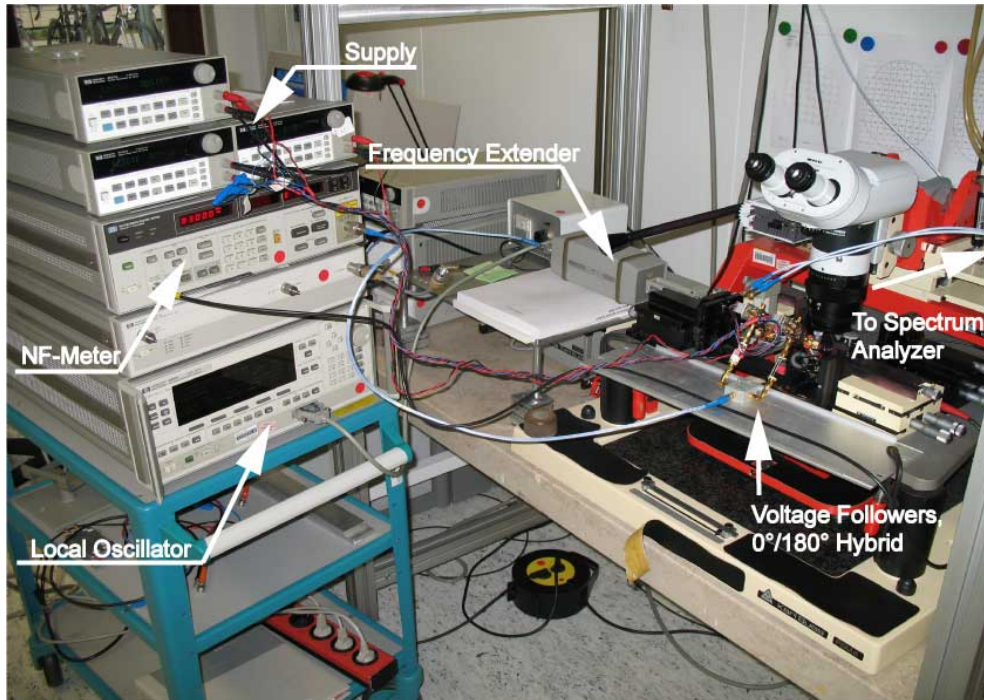
FIGURE 4.27: Block diagram of the measurement setup for the determination of the conversion gain and the noise figure.

measuring noise figures in the range of 0...30 dB.

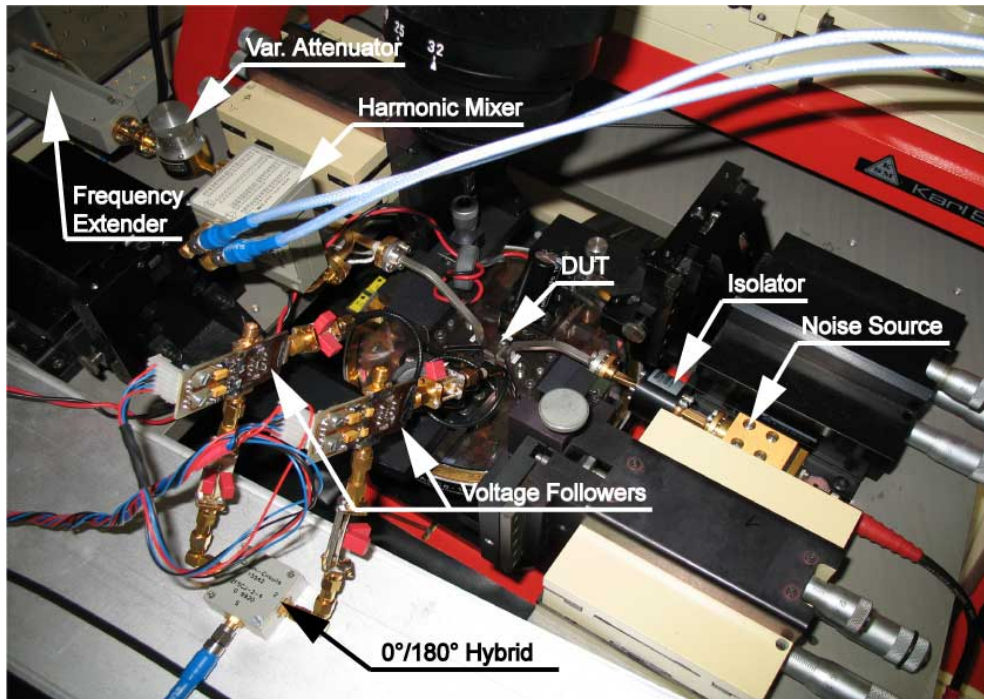
Noise Source The W-band noise source NC 5110 and the V-band noise source NC 5115, both from NoiseCom, were used as RF sources for the measurements. The large impedance difference of the sources in the "ON" and "OFF" state results in a ripple in the measurement results. Thus, an isolator (QIF-W00000 from Quinstar) had to be used. This measure additionally reduces the measurement uncertainty.

LO source The local oscillator is provided by HP's 83650A frequency synthesizer. Due to its limited frequency range (max. 50 GHz), appropriate frequency extenders (83557A and 83558A for the V- and W-band, respectively) are used. A comparison of the delivered output power with the value set on the synthesizer showed unsatisfactorily large differences, therefore an adjustable attenuator, a 20 dB directional coupler, and a harmonic mixer were used to set and to monitor the power delivered to the DUT.

Thermal chuck This device (ERS Waferterm SP 53 A) keeps the backside temperature of the wafer at a defined level. The wafer temperature can be set from -10°C to $+140^{\circ}\text{C}$. The temperature for all measurements was set to 25°C . Due to the lack of a thermal chamber, temperature sweeps were carried out down to $+10^{\circ}\text{C}$ only. Neither the chuck nor the control unit can be seen in figure 4.28(a).



(a) Setup for the measurement of the noise figure and the conversion gain.



(b) Detailed view of the noise figure measurement setup. The devices on the left hand side, including the $\times 6$ frequency extender, the variable attenuator, the directional coupler (QDC-HW20000 from Quinstar), and the GS probe, supply the LO. The noise source and the isolator on the right hand side supply the RF signal.

FIGURE 4.28: Photographs of the measurement setup for the determination of the conversion gain and the noise figure.

IF Buffer The output of the DUT is designed for high impedance external loads. Therefore, voltage followers with an input impedance of $100\text{ k}\Omega$ were employed as IF Buffers. Low-noise operational amplifiers (OPA620 from Burr Brown / Texas Instruments) were chosen to ensure that their impact on the noise figure measurement is small. The outputs of the buffers are matched to the $50\text{ }\Omega$ measurement environment. The input to the noise figure meter is single-ended, so a low-frequency $0^\circ/180^\circ$ hybrid from Minicircuits was used to combine the differential IF outputs.

4.3.1 Noise Figure and Conversion Gain

The noise figure of any device, building block, or system can be determined in several ways. The most common methods are the *direct noise measurement method*, the *signal generator method*, and the *Y-factor method*.

The *direct noise measurement method* uses a known signal at the input. It is assumed that also the noise floor at the input is known. The thermal noise is usually taken as a reference, resulting in a noise floor of

$$P_{N,\text{In}} = 10 \log_{10}(kT) + 30 = -174 \text{ dBm/Hz}. \quad (4.55)$$

The gain of the device is determined by measuring the signal power (in dBm) at the output and relating this value to the input,

$$G = P_{S,\text{Out}} - P_{S,\text{In}} \quad [\text{dB}]. \quad (4.56)$$

Then, the noise floor (in dBm, 1 Hz bandwidth) at the output is measured and the noise figure calculated using

$$\text{NF} = P_{N,\text{Out}} - P_{N,\text{In}} - G \quad [\text{dB}]. \quad (4.57)$$

The *signal generator method* uses a signal source at the input of the device, and a power meter at the output [Battle 07]. First, the 3 dB bandwidth is determined by sweeping the frequency. Then, with the signal source turned off, the noise power level at the output is measured,

$$P_{N,\text{Out}} = FG_{\text{av}}kT_0B, \quad (4.58)$$

Next, the signal source is turned on and tuned to the frequency of maximum gain. The absolute value of the gain is not needed. The input power level is adjusted such that the output power reads exactly $2 \times P_{N,\text{Out}}$, that is, $P_{N,\text{In}}$ and $P_{S,\text{In}}$, which are uncorrelated, contribute in equal parts to $P_{S,\text{Out}}$. Therefore,

$$G_{\text{av}}P_{S,\text{In}} = FG_{\text{av}}kT_0B, \quad (4.59)$$

and

$$F = \frac{P_{S,\text{In}}}{kT_0B}. \quad (4.60)$$

These two methods can be applied to DUTs independent of their noise figure. Especially DUTs with high noise figures can be accurately characterized. The disadvantages are the need for a separate measurement of the bandwidth, and the dependence of the noise figure on the determination of the signal gain using the direct noise measurement method. Moreover, both methods are not well suited for automatic measurements.

The *Y-factor method* does not need a measurement of the DUT's gain or the bandwidth. A graphical description of this method is depicted in figure 4.29. The noise

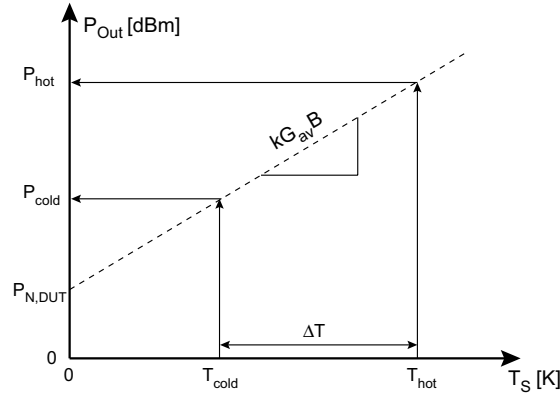


FIGURE 4.29: Determination of the noise figure using the Y-factor method.

powers at two different input temperatures, T_{cold} and $T_{\text{hot}} = T_{\text{cold}} + \Delta T$, are measured. Then, the noise figure is determined from the slope and the intercept with the y-axis of an extrapolated line that connects both noise temperature / output noise power pairs.

This procedure can be derived by rearranging equation (4.40), which yields

$$F = 1 + \frac{P_{N,DUT}}{kT_0 B G_{av}}. \quad (4.61)$$

The output powers referring to the "cold" and the "hot" state are

$$P_{\text{cold}} = kG_{av} B(T_{\text{cold}}) + P_{N,DUT} \quad (4.62)$$

and

$$P_{\text{hot}} = kG_{av} B(T_{\text{cold}} + \Delta T) + P_{N,DUT}. \quad (4.63)$$

Dividing equation (4.63) by equation (4.62) results in

$$\frac{P_{\text{hot}}}{P_{\text{cold}}} = 1 + \frac{kG_{av} \Delta T B}{kG_{av} T_{\text{cold}} B + P_{N,DUT}}, \quad (4.64)$$

which after rearrangement yields

$$F = \frac{\Delta T / T_{\text{cold}}}{P_{\text{hot}} / P_{\text{cold}} - 1}. \quad (4.65)$$

The fraction in the denominator, $P_{\text{hot}}/P_{\text{cold}}$, is called the Y-factor. The fraction in the numerator, $T_{\text{hot}}/T_{\text{cold}}$, is a property of the noise source. The value that is provided by noise source manufacturers is the excess noise ratio (ENR). It is defined by the ratio of noise powers delivered to a $50\ \Omega$ load. This is not equal to the temperature ratio since the expressions derived above always refer to available powers. These are different from the actually delivered ones since the input impedance of the DUT usually differs from $50\ \Omega$. The error introduced by taking the ENR as the temperature ratio is therefore very small for matched loads.

Equation (4.65) shows the benefits of the Y-factor method: Neither the bandwidth B nor the gain of the DUT, $G_{\text{av,DUT}}$ need to be determined. In addition, this method uses ENR values and power level measurements only, therefore it is well suited for automatic measurements.

The gain of the DUT is a property that is also of interest. It is also obtained from the Y-factor measurement using

$$G_{\text{DUT}} = \frac{\frac{P_{\text{hot}} - P_{\text{cold}}}{T_{\text{hot}} - T_{\text{cold}}}}{\frac{P_{\text{hot,cal}} - P_{\text{cold,cal}}}{T_{\text{hot,cal}} - T_{\text{cold,cal}}}}, \quad (4.66)$$

where the index "cal" refers to the values obtained during calibration, that is, without the DUT.

All of these measurement methods usually do not provide the noise figure and the gain of the DUT, but the system noise figure and the system gain. The DUT and the measurement equipment make up a cascaded system, and both properties, NF_{DUT} and G_{DUT} , need to be deembedded from the measured results. The noise factor F_{total} of a cascaded system is determined using Friis' formula [Friis 44],

$$F_{\text{total}} = F_1 + \frac{F_2 - 1}{G_1} + \frac{F_3 - 1}{G_1 G_2} + \dots \quad (4.67)$$

In this equation, the index refers to the number of the stage in the chain. Note that any losses in front of the DUT directly deteriorate the noise figure. The gain of the DUT is obtained by subtracting the gain and the losses of the measurement setup.

Automated noise figure measurement systems, such as the noise figure meter HP 8970B, offer calibration to get precise measurement results. Thus, no deembedding of the equipment's noise figure needs to be done by hand. Regarding the overall measurement setup, a calibration is only possible if the operating frequency of the DUT is entirely covered by the input frequency range of the measurement system. This is usually not the case when millimeter wave mixers are characterized. In this scenario, only the low frequency losses at the IF and the noise figure meter's internal noise figure can be deembedded automatically. All other losses need to be deembedded from the measurement results by hand.

The measured noise figure and conversion gain are shown in figure 4.30, together with the simulated results. Two extenders (V- and W-band) were used to cover

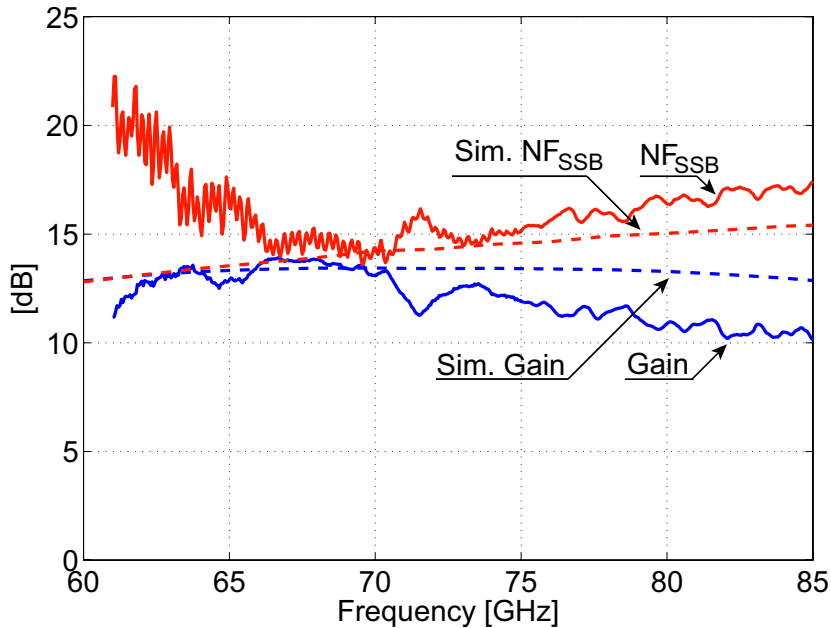


FIGURE 4.30: Single-sideband noise figure (red) and conversion gain (blue). The solid lines represent the measured values, the dashed lines are the simulated results. LO Power was set to +7 dBm. The measurement uncertainty of the noise figure is ± 0.58 dB (3σ), and the conversion gain has an uncertainty of ± 0.61 dB (3σ).

the frequency range from 60 GHz to 85 GHz. All losses have been deembedded from the measurements. Both the measured noise figure and conversion gain show good agreement with simulations.

The precision of the measurement procedure is determined by several uncertainties:

Losses before DUT: Losses in the measurement setup that appear between the noise source and the DUT deteriorate the measurement result. As long as they are not present during calibration, their impact can be derived in two ways. Either Friis' formula, equation (4.67), shows that the total noise figure rises by the losses before the DUT since passive devices have a noise figure equal to their losses. A more precise formula that also accounts for the temperature T_L of the lossy parts before the DUT is given by [Agilent Tech 07,b]

$$F_{\text{total}} = 1 + \frac{T_{\text{DUT}}}{T_0} \frac{1}{L} - \frac{(L-1)}{L} \frac{T_L}{T_0}, \quad (4.68)$$

where L represents the losses on a linear scale, and T_L stands for the temperature of the lossy device. The error that arises when Friis's formula is used instead of this one is depicted in figure 4.31. The changes in noise figure

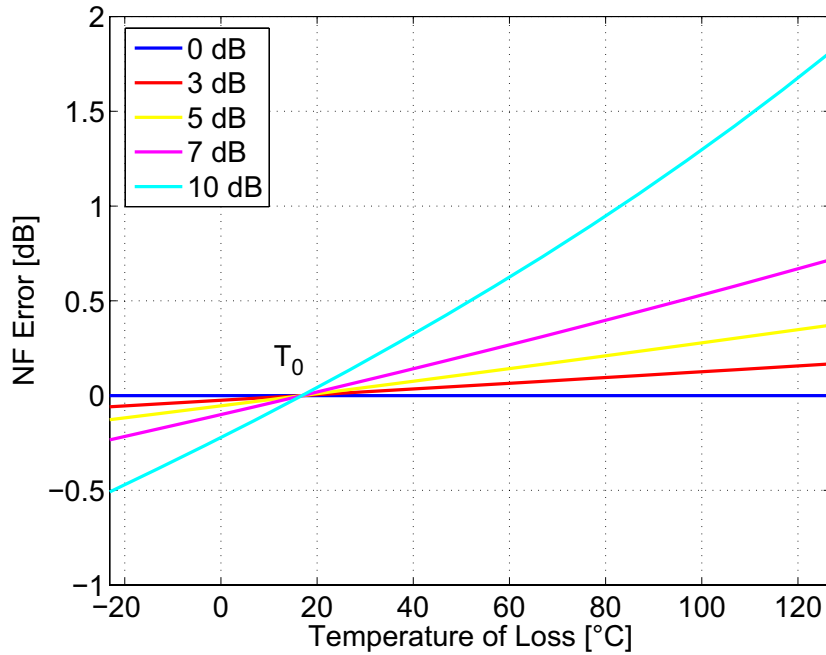


FIGURE 4.31: Error (in dB) in noise figure measurement when the temperature of the lossy parts before the DUT is not accounted for. The parameter is the loss in dB.

are small as long as the insertion losses are moderate or their temperature is close to T_0 .

In the measurements that are presented later in this chapter, an isolator and a measurement probe are placed between the noise source and the DUT. The overall loss of this configuration is 3.2 dB (2 dB from the isolator and 1.2 dB from the probe, both values are obtained from datasheets). The error that is made when the temperature of these devices is not accounted for stays lower than 0.15 dB up to a temperature of 120°C. Therefore, Friis' formula was used to deembed these losses.

Losses after DUT / Second stage contribution According to Friis' formula, the overall noise figure will be mostly determined by the noise figure of the DUT alone if its gain is high compared to the noise figure of the second device in the chain. The second term in equation (4.67) is called second stage contribution. Regarding the noise figure, losses after the DUT do not enter strongly into the measured noise figure since a low noise IF amplifier was used. These considerations do not apply for the gain, which must be corrected according to the actual gain or losses after the DUT.

Mismatches The interfaces between the noise source and the DUT, between the noise source and the noise figure meter (during calibration), and between the DUT and the noise figure meter are not perfectly matched. In addition,

the output impedance of the noise source changes when it is switched from the 'hot' to the 'cold' state. To reduce effects related to changing impedance ratios at the interface between the noise source and the DUT, an isolator was used. Impedance changes result in a ripple on the measured parameters versus frequency if the DUT is not well matched.

ENR of noise source The actual ENR of the noise source deviates from the value in the data sheet by a given uncertainty that is usually provided by the manufacturer. A source of error are unknown changes in the ENR due to aging. Furthermore, the ENR depends on the load impedance. This uncertainty is reduced by using an isolator between the noise source and the DUT.

External interferers Interfering signals picked up from the measurement setup or from the power supply of the DUT result in wrong measurement results. Since these spurs are usually located in a narrow frequency band, their impact can be eliminated by monitoring the spectrum during the measurement and changing the center frequency.

Noise figure meter The device that actually measures the parameters has an uncertainty in determining the noise figure and the gain. These values can be obtained from the manual.

The uncertainty in noise figure measurement is determined by the total differential of Friis' formula for a three stage system that consists of the DUT, the isolator, and the noise figure meter. The measured noise figure is given by

$$F_{\text{meas}} = F_{\text{ISO}} + \frac{F_{\text{DUT}} - 1}{G_{\text{ISO}}} - \frac{F_{\text{NFM}} - 1}{G_{\text{ISO}}G_{\text{DUT}}}, \quad (4.69)$$

where $F_{\text{ISO}} = 1/G_{\text{ISO}}$ is the noise figure of the isolator (G_{ISO} is the gain of the isolator). The noise factor of the noise figure meter and the measured noise factor are denoted F_{NFM} and F_{meas} , respectively. The noise factor and the conversion gain of the DUT are labeled F_{DUT} and G_{DUT} . Rearranging equation (4.69) yields

$$F_{\text{DUT}} = F_{\text{meas}}G_{\text{ISO}} - \frac{F_{\text{NFM}} - 1}{G_{\text{DUT}}} \quad (4.70)$$

of which the total differential is given by

$$\delta F_{\text{DUT}} = \frac{\partial F_{\text{DUT}}}{\partial F_{\text{meas}}} \delta F_{\text{meas}} + \frac{\partial F_{\text{DUT}}}{\partial G_{\text{ISO}}} \delta G_{\text{ISO}} + \frac{\partial F_{\text{DUT}}}{\partial F_{\text{NFM}}} \delta F_{\text{NFM}} + \frac{\partial F_{\text{DUT}}}{\partial G_{\text{DUT}}} \delta G_{\text{DUT}}. \quad (4.71)$$

The partial derivatives are denoted $\frac{\partial}{\partial x}$. Insertion of the derivatives yields

$$\delta F_{\text{DUT}} = G_{\text{ISO}} \delta F_{\text{meas}} + F_{\text{meas}} \delta G_{\text{ISO}} - \frac{1}{G_{\text{DUT}}} \delta F_{\text{NFM}} + \frac{F_{\text{NFM}} - 1}{G_{\text{DUT}}^2} \delta G_{\text{DUT}}. \quad (4.72)$$

The noise figure and the gain are usually given in dB, so this equation is converted to a logarithmic scale, resulting in

$$\delta\text{NF}_{\text{DUT}} = \frac{\text{G}_{\text{ISO}}\text{F}_{\text{meas}}}{\text{F}_{\text{DUT}}}(\delta\text{NF}_{\text{meas}} + \delta\text{G}_{\text{ISO,dB}}) - \frac{\text{F}_{\text{NFM}}}{\text{F}_{\text{DUT}}\text{G}_{\text{DUT}}}\delta\text{NF}_{\text{NFM}} + \frac{\text{F}_{\text{NFM}} - 1}{\text{F}_{\text{DUT}}\text{G}_{\text{DUT}}}\delta\text{G}_{\text{DUT,dB}}. \quad (4.73)$$

Note that the values for NF and G_{dB} are in dB, while the values for F and G are in a linear scale. The sources of uncertainty are uncorrelated, so the overall uncertainty is obtained from the combination of each uncertainty (the δ terms) by the root sum of squares (RSS),

$$\delta\text{NF}_{\text{DUT}} = \sqrt{\left(\frac{\text{G}_{\text{ISO}}\text{F}_{\text{meas}}}{\text{F}_{\text{DUT}}}\right)^2 (\delta\text{NF}_{\text{meas}}^2 + \delta\text{G}_{\text{ISO,dB}}^2) + \left(\frac{\text{F}_{\text{NFM}}}{\text{F}_{\text{DUT}}\text{G}_{\text{DUT}}}\delta\text{NF}_{\text{NFM}}\right)^2 + \left(\frac{\text{F}_{\text{NFM}} - 1}{\text{F}_{\text{DUT}}\text{G}_{\text{DUT}}}\delta\text{G}_{\text{DUT,dB}}\right)^2}. \quad (4.74)$$

The individual uncertainty terms are the RSS of the uncertainties of their contributors. Therefore, $\delta\text{G}_{\text{ISO}}$ can be included in $\delta\text{NF}_{\text{meas}}$, yielding

$$\delta\text{NF}_{\text{meas}}^2 = \delta\text{NS}_{\text{HF,ISO}}^2 + \delta\text{ISO,DUT}^2 + \delta\text{DUT,NFM}^2 + \delta\text{ENR}_{\text{HF}}^2 + \delta\text{MU}_{\text{NF}}^2 + \delta\text{G}_{\text{ISO,dB}}^2, \quad (4.75)$$

where $\delta_{\text{X,Y}}$ refers to uncertainties resulting from impedance mismatches at the interface between X and Y, and $\delta\text{MU}_{\text{NF}}$ is the noise figure measurement uncertainty of the noise figure meter. The uncertainty in the ENR of the noise source is termed $\delta\text{ENR}_{\text{HF}}$ for the HF range. For the calibration, $\delta\text{ENR}_{\text{LF}}$ refers to the low frequency noise source; it is included in

$$\delta\text{NF}_{\text{NFM}}^2 = \delta\text{NS}_{\text{LF,NFM}}^2 + \delta\text{ENR}_{\text{LF}}^2 + \delta\text{MU}_{\text{NF}}^2, \quad (4.76)$$

which accounts for uncertainties of the calibration process. The last term in equation (4.74) reflects the uncertainty in the determination of the conversion gain. It is the term that is most sensitive to any uncertainties in the the setup,

$$\delta\text{G}_{\text{DUT,dB}}^2 = \delta\text{NS}_{\text{HF,ISO}}^2 + \delta\text{ISO,DUT}^2 + \delta\text{DUT,NFM}^2 + \delta\text{ENR}_{\text{HF}}^2 + \delta\text{G}_{\text{ISO,dB}}^2 + \delta\text{MU}_{\text{Gain}}^2. \quad (4.77)$$

The last term, $\delta\text{MU}_{\text{Gain}}^2$, refers to the gain measurement uncertainty of the noise figure meter.

Figure 4.32 shows the sensitivity of the noise figure uncertainty on the parameters causing the largest changes. In figure 4.33, the same considerations are depicted for the uncertainty in the conversion gain. Changing the input matching (VSWR) of the noise source (HF Noise Source in figure 4.32), or the input matching of

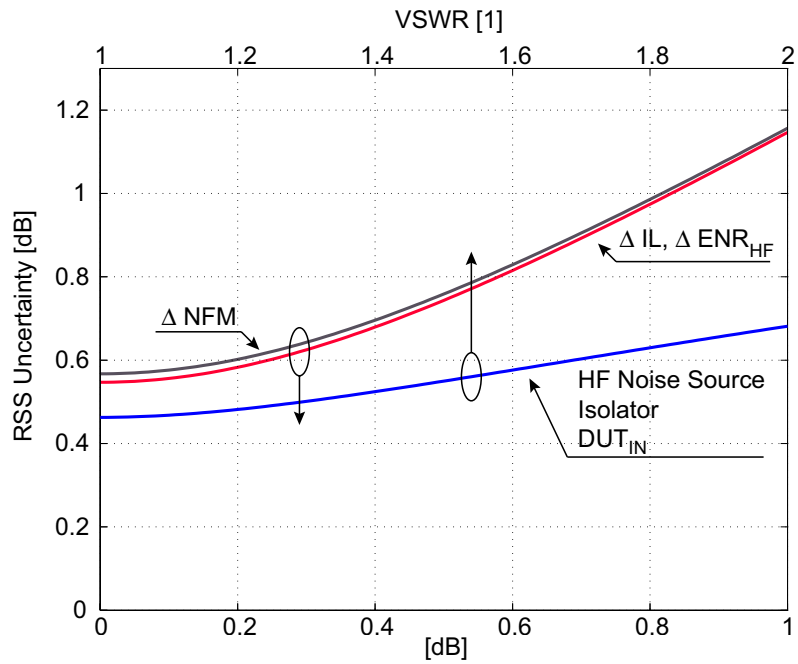


FIGURE 4.32: Dependence of the total uncertainty of the noise figure measurement on certain parameters. Only one parameter was swept at a time.

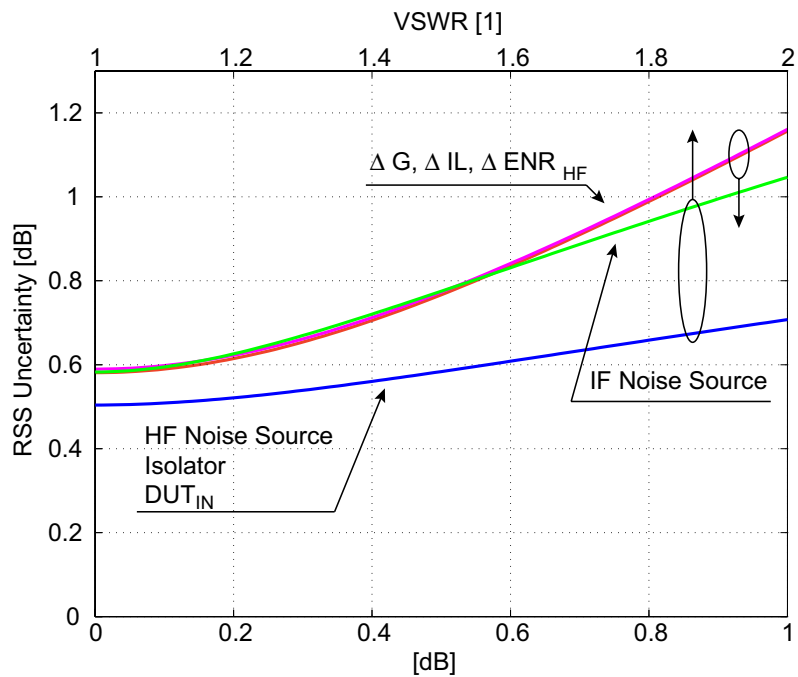


FIGURE 4.33: Dependence of the total uncertainty of the conversion gain measurement on components of the measurement setup. Only one parameter was swept at a time.

the DUT (DUT_{IN}), or either input or output matching of the isolator from 1:1 to 2:1 results in a degradation of the total measurement uncertainty from 0.46 dB to 0.68 dB. Regarding the gain uncertainty, figure 4.33, the RSS value increases from 0.51 dB for $\text{VSWR} = 1:1$ to 0.71 dB for $\text{VSWR} = 2:1$. Thus, any mismatches in the HF section of the measurement setup degrade the noise figure and the gain uncertainty. Uncertainties in the insertion loss of the isolator (ΔIL) and in the ENR of the HF noise source ($\Delta \text{ENR}_{\text{HF}}$) account to the overall noise figure and gain uncertainty equally. This is evident since the isolator and the HF noise source can be regarded as an entity. The uncertainty of the noise figure meter itself in measuring the noise figure enters directly into the overall noise figure measurement uncertainty (ΔNFM). The same applies to the uncertainty of the noise figure meter in determining the gain (ΔG). The last parameter that enters into the overall gain uncertainty is the VSWR of the IF noise source ('IF Noise Source' in figure 4.33). This is explained by errors that are introduced during calibration, and therefore show up in the final result.

All other components of the measurement setup, especially the noise figure and the gain of the DUT, do not have a large impact on the overall uncertainty. Also the noise figure of the noise figure meter is of minor importance for the uncertainty of the measurement, as long as it stays lower than the noise figure of the DUT. Table 4.1 lists all uncertainty contributors. The measured mixer and the IF buffer

TABLE 4.1: Contributors to the overall measurement uncertainty. All parameters are specified values, except for the DUT. $f_{\text{HF}} = 77 \text{ GHz}$, $f_{\text{IF}} = 10 \text{ MHz}$.

<i>HF Noise Source</i>	VSWR	1.6:1
	$\Delta \text{ENR} (3\bar{\sigma})$	0.18 dB
<i>IF Noise Source</i>	VSWR	1.15:1
	$\Delta \text{ENR} (3\bar{\sigma})$	0.1 dB
<i>Isolator</i>	$\Delta \text{Insertion Loss} (3\bar{\sigma})$	0.18 dB
	Input VSWR	1.4:1
	Output VSWR	1.4:1
<i>Device Under Test</i>	Input VSWR	1.665:1
	Noise Figure	15.75 dB
	Conversion Gain	11.5 dB
	Output VSWR	1:1
<i>Noise Figure Meter</i>	Input VSWR	1.8:1
	Noise Figure	7.03 dB
	NF measurement uncertainty ($3\bar{\sigma}$)	0.1 dB
	Gain measurement uncertainty ($3\bar{\sigma}$)	0.15 dB

are regarded as an entity, so the value for the output VSWR of the DUT refers to the output of the IF buffer. The total uncertainty of the setup regarding the

measurement of the noise figure is ± 0.58 dB. The uncertainty in measuring the conversion gain is ± 0.61 dB.

Noise Figure and Conversion Gain vs. LO Power

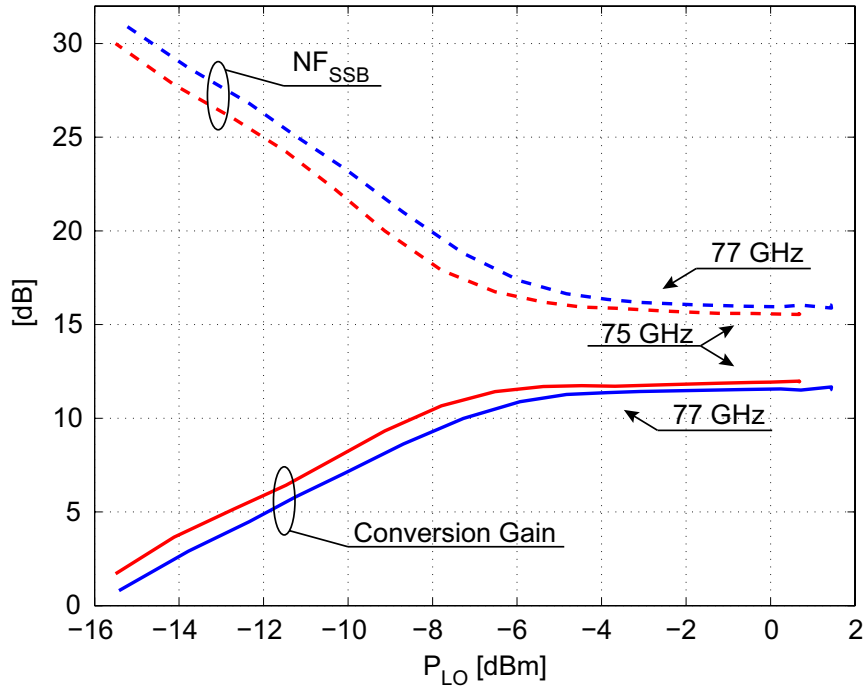


FIGURE 4.34: Dependence of single-sideband noise figure and conversion gain on the LO Power.

The noise figure and the conversion gain of the mixer depend on the LO power. The plot of this measurement is shown in figure 4.34 for two frequencies, 75 GHz and 77 GHz. At 75 GHz, the mixer needs -6 dBm to operate properly. More LO power is needed at 77 GHz, -4 dBm. This difference is explained by the characteristic of the LO buffer. It provides more gain at 75 GHz than at 77 GHz, see figure 4.5.

Noise Figure vs. IF

The behavior of the noise figure versus the IF is an important property of mixers in direct conversion receivers. In general, the $1/f$ noise degrades the noise figure, limiting the usability of the mixer in such systems.

The IF dependent noise figure was measured manually using the noise marker function of a spectrum analyzer (HP 4448A). As with the automatic measurement, the Y-factor method was used to calculate the noise figure from the measured noise floor.

The phase noise of the LO has an impact on the measured noise-floor approaching DC. Therefore, a dielectric resonant oscillator (Raditek RDRO-B-19.5G-9d5v) that shows good phase noise and a $\times 4$ frequency multiplier were used. This combination results in a phase noise of -78 dBc (1 Hz) at 10 kHz offset at a frequency of 78 GHz. Figure 4.35 plots the measured and simulated noise figure as a function

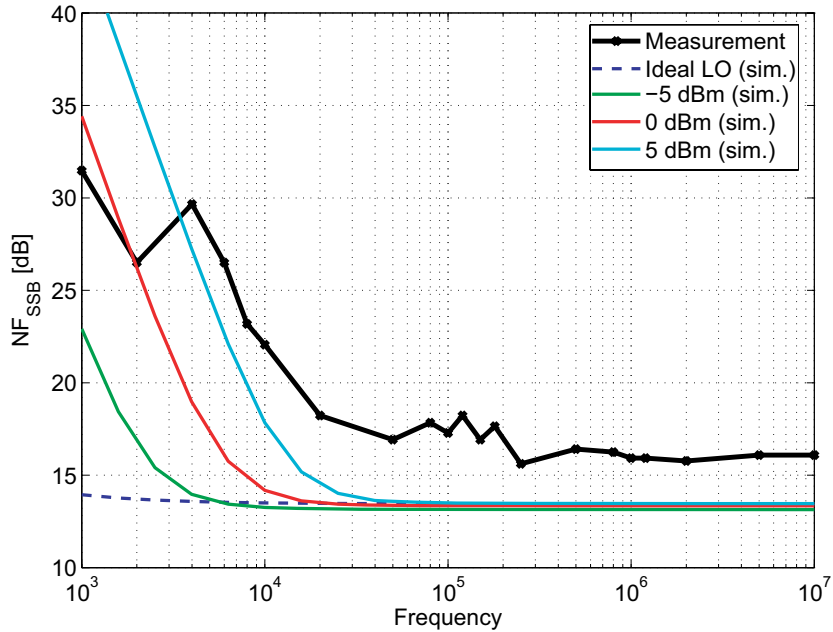


FIGURE 4.35: Measured noise figure versus IF ($f_{LO} = 78$ GHz, $P_{LO} = 3$ dBm). The simulated traces depict ideal (dashed trace) and non-ideal LO sources (with phase noise according to the used DRO) with different LO power levels.

of the IF. The simulations show that the impact of the oscillator's phase noise on the noise figure measurement rises with increasing LO power. Therefore, the impact of the DRO on the measurement cannot be neglected, and only an upper bound for the onset of the $1/f$ noise can be stated, $f_c = 42$ kHz.

4.3.2 1 dB Compression Point

The measurement of the 1 dB compression point was done using a $\times 4$ multiplier (from Spacek Labs Inc.) and a variable attenuator instead of the noise source at the RF port. Due to the insufficient output power at higher frequencies, the compression point had to be determined at 75 GHz. Figure 4.36 shows the result. On the y-axis, the differential peak-to-peak output voltage is depicted instead of the output power because of the high impedance input of the IF buffer. The measured 1 dB compression point is at an input level of -0.3 dBm. The corresponding output level is 10.7 dBV_{pp}, which is equal to 3.43 V_{pp}.

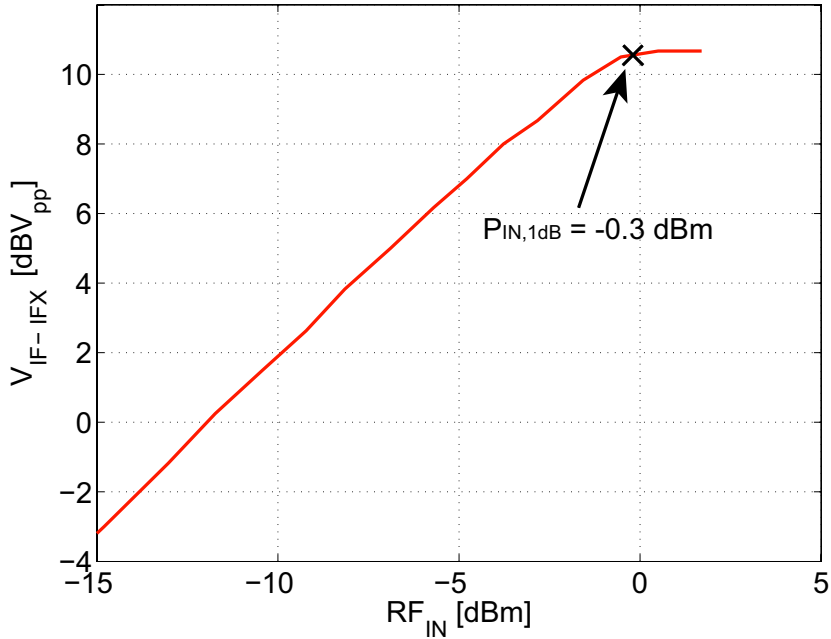


FIGURE 4.36: Measured 1 dB compression point of the mixer. The LO frequency is 75 GHz, the IF frequency is 10 MHz.

4.3.3 Third-Order Intercept Point

The third-order intercept point was measured using two RF sources (the $\times 4$ multiplier and the W-band source from Agilent), set to the frequencies $f_{\text{RF},1} = 76.5$ GHz and $f_{\text{RF},2} = f_{\text{RF},1} + 200$ kHz. The LO frequency was $f_{\text{LO}} = 76.499$ GHz, provided by the V-band frequency extender that was operated out of the specified frequency range. The RF signals were combined using a directional coupler. An isolator was used additionally to decouple the two sources. This prohibits the unwanted generation of harmonics, caused by one source and generated in the highly-nonlinear frequency multiplier of the other one. At the output of the combiner, the power of both signals was adjusted using a variable attenuator. The signal power was monitored by a second directional coupler and a harmonic mixer. The setup was calibrated using a power meter prior to measurement.

The output of the mixer was first amplified by an instrumentation amplifier and then fed into a spectrum analyzer. The output power of the fundamental tones as well as the output power of the components at the frequencies of the third-order IF components are plotted in figure 4.37. The input referred third-order intercept point is at +6.5 dBm. This is in excellent agreement with the simulated value, +7.5 dBm in figure 4.10.

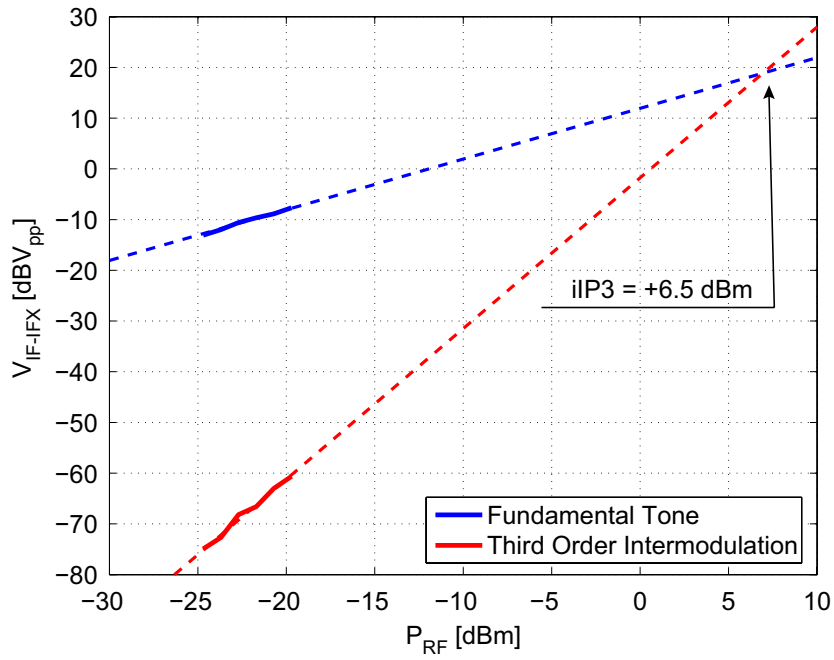


FIGURE 4.37: Measured input referred third-order intercept point. The IF frequencies of the fundamental tones are 1 MHz and 1.2 MHz.

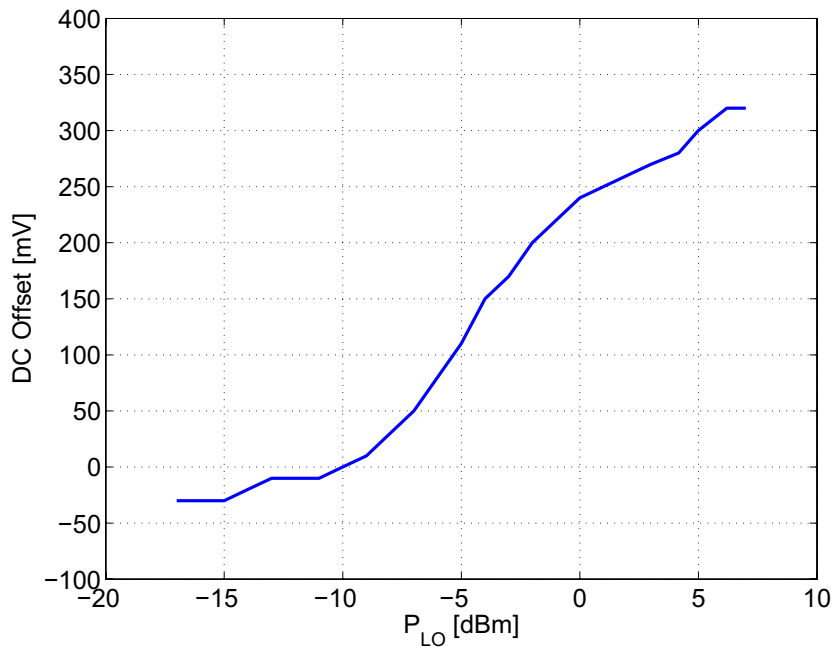


FIGURE 4.38: Measured differential DC offset at the IF ports of the mixer versus LO power. The LO frequency was set to 77 GHz. The maximum DC offset is 320 mV.

4.3.4 DC Offset

Figure 4.38 shows the measured DC offset at the IF output of the mixer versus the LO power. The LO power was swept using a variable attenuator. A directional coupler and a harmonic down-conversion mixer (Agilent 11950W) together with a spectrum analyzer (Agilent 8595EC) were employed to monitor the LO power. To get a reference level for the actual power transferred to the LO port of the mixer, a power meter was attached instead of the probe, and the power levels from the spectrum analyzer and the power meter were compared. Additionally, the loss of the probe was subtracted from the measured input power. At the IF port of the mixer, two multimeters were used to measure the voltage difference.

4.3.5 Matching and Isolation

The matching of the RF as well as the LO port both have an impact on various performance parameters. Usually, the term 'matching' refers to impedance matching, which defines the amount of input power that is transferred to the succeeding stage or reflected back to the source. Generally speaking, a return loss of roughly 10 dB, which corresponds to a Voltage Standing Wave Ratio (VSWR) of 2 : 1, is the minimum value where a circuit is called matched.

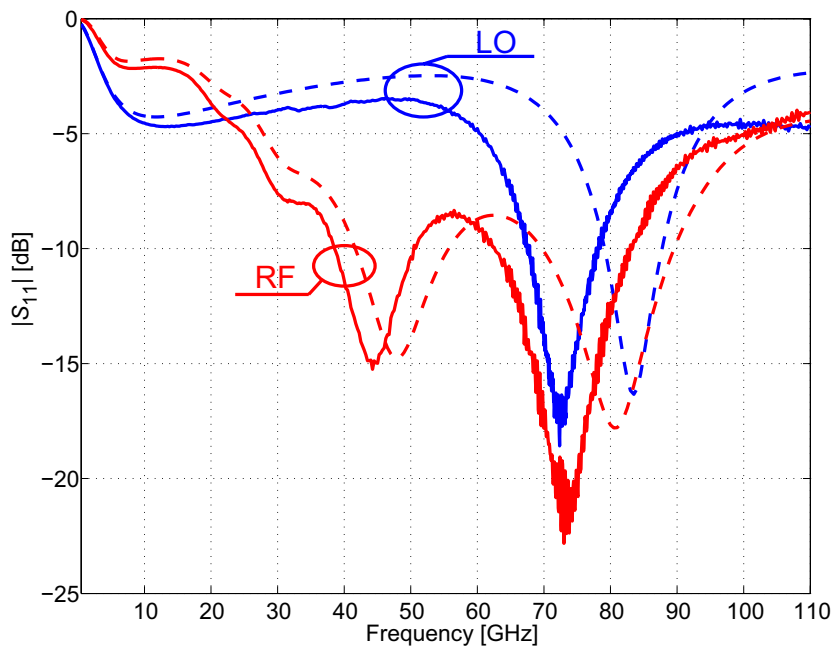


FIGURE 4.39: Measured small-signal matching of the RF and the LO port. The simulated curves are plotted as dashed lines.

Figure 4.39 illustrates the matching at both ports from an S -parameter measure-

ment⁶. The plotted magnitudes are equivalent to the return loss.

The same figure shows the comparison between the simulated and the measured data. The qualitative behavior of both curves matches well. The differences between the curves are explained by the narrow-band model for the transmission lines, see section 3.4.

The frequency range covered by the measurements, 0 to 110 GHz, is much broader than the frequency band of the application, 76 to 77 GHz. This is important especially for the investigation of stability issues.

The determination of the isolation between the LO and the RF port by an S -parameter measurement yields only a rough estimate. The reason for this is that the LO port of the mixer is operated in large-signal mode. These power levels are usually not provided by a network analyzer. Therefore, the mixer is not mixing and the measured value can deviate substantially from the value achieved under normal operating conditions.

4.3.6 Temperature Behavior

The temperature behavior of the mixer's noise figure and the conversion gain is an important performance parameter. Due to packaging and self-heating, the mixer will not be operated at room temperature. On the other hand, additional cooling measures are not welcome since each additional component should be avoided to reduce costs. The noise figure and the conversion gain versus temperature are plotted in figure 4.40. The temperature is the backside temperature of the chip, which was held at a constant level during the measurement by the thermal chuck.

Up to 75 °C, the noise figure rises with a slope of 0.04 dB / °C, while the gain is approximately temperature-independent. Above that temperature, the increase in noise figure is larger which is a result of a lack in LO power (see subsection 4.3.1). This explains the decrease in gain, too. Therefore, the values for the noise figure and the conversion gain above 75 °C are not representative.

Figure 4.41 shows a comparison between the measured and the simulated single-sideband noise figure and conversion gain versus temperature.

4.3.7 Measurement Repeatability

The measurement result of the noise figure and the conversion gain across the wafer is depicted in figure 4.42. This plot gives information about the steadiness of the experiment and the homogeneity of the processed wafer. By this result, the measurement reliability is confirmed. The average value of the noise figure, μ_{NFSSB} , is 15.78 dB, and the average value of the conversion gain, μ_{Gain} , is 11.5 dB.

⁶Strictly speaking, S_{11} is equal to the return loss only for unilateral devices. Taking S_{11} as the return loss results in a negligible error for the circuits presented here.

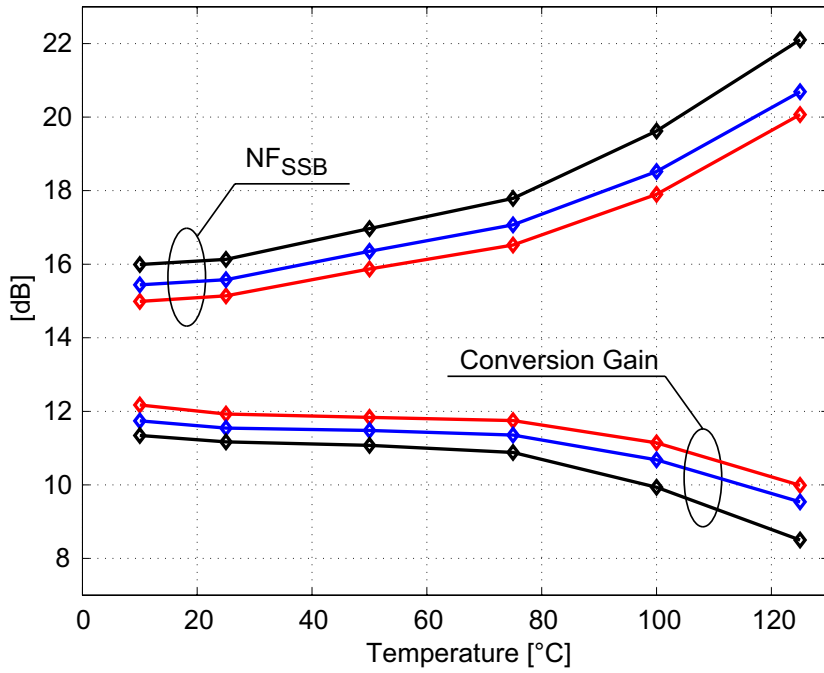


FIGURE 4.40: Measured temperature dependence of the single-sideband noise figure and the conversion gain on the temperature. The red, blue, and black curves represent LO frequencies of 75, 77, and 79 GHz, respectively.

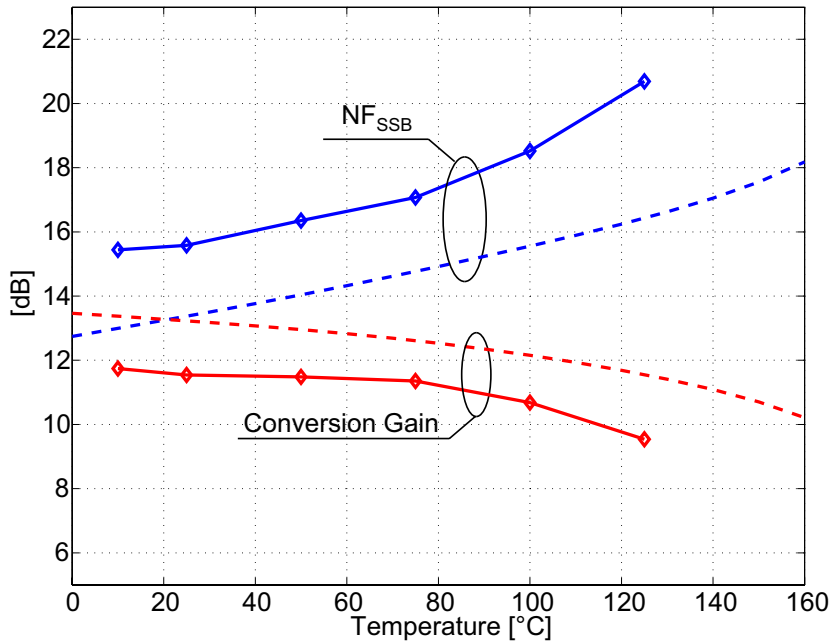


FIGURE 4.41: Comparison of measured and simulated temperature dependence of the noise figure and the conversion gain. $f_{LO} = 77$ GHz, $f_{IF} = 10$ MHz.

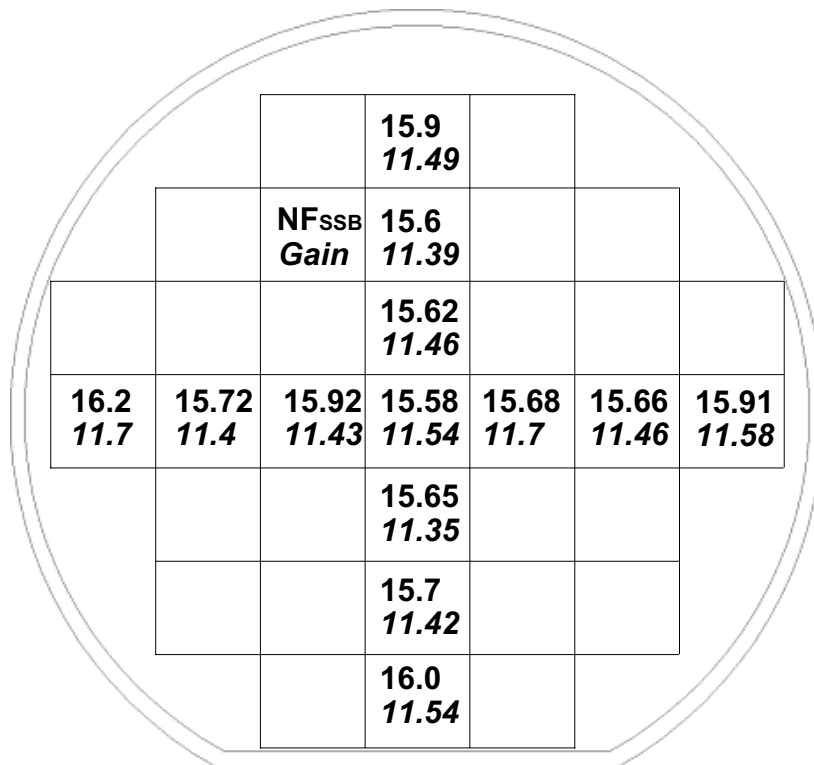


FIGURE 4.42: Noise figure and conversion gain over the wafer (in dB). The LO frequency is 77 GHz, the IF is at 10 MHz.

4.4 Summary

Design considerations for millimeter-wave down-conversion mixers were presented in this chapter. These considerations were followed for the implementation of a 77 GHz down-conversion mixer in SiGe technology for automotive radar applications. After a short review about the characterization of the most important mixer properties, the measurement results were reported. The measurement uncertainties regarding the noise figure and the conversion gain of the mixer were calculated.

A comparison of the fabricated mixer with state-of-the-art millimeter-wave down-conversion mixers at 77 GHz is shown in table 4.2. This table focuses on the most important parameters, which are the noise figure, the conversion gain, the compression point, and the power consumption. Only direct-conversion mixers with the same architecture (homodyne receiver) in SiGe technology are compared. Publications about implementations in other technologies, like in GaAs [Bryant 04], can also be found. Also passive subharmonic mixers (GaAs [Shimura 98], SiGe [Hung 05]) are reported. Since the proposed architecture in this work and the implementation in SiGe offer huge possibilities, a comparison with the results from other technologies or other architectures is regarded unfair and therefore omitted.

The mixer presented in this work shows superior properties regarding linearity. Its noise figure is comparable to state-of-the-art. The potential regarding noise figure when inductive degeneration is used is an option to lower the noise figure. With this configuration, the need for sophisticated methods like precise EM simulations and parasitics extraction becomes apparent to avoid instability. In terms of power consumption, the mixer consumes more than other implementations. Possibilities to decrease the power consumption include a decrease in current in the LO buffer amplifier and in the Gilbert cell. Lowering the current in the Gilbert cell also decreases linearity, so different circuit implementations must be considered.

TABLE 4.2: State-of-the-art millimeter-wave down-conversion mixers at 77 GHz.

	NF _{SSB} [dB]	iCP _{1dB} [dBm]	Conversion Gain [dB]	IF Buffer	Supply Voltage [V]	Power Consumption [mW]
[Reynolds 06]	12.8	-14.7	20	Yes	3	360
[Perndl 04,b]	14	-20	24	Yes	-5	300
[Wang 06]	18.4	-12	13.4	Yes	4.5	176
[Hartmann 06]	16	-3	15.5	No	5.5	187
<i>This work</i> [Dehlink 06,b]	16.5	0	11	No	5.5	413

Chapter 5

80 GHz Quadrature Receiver Front-End

A receiver front-end for sensing and communication applications in the frequency range from 75 to 86 GHz is presented in this chapter. The front-end converts a single-ended RF input signal to a differential in-phase (0°) and a differential quadrature (90°) IF output signal. The output frequency of the front-end ranges from frequencies close to DC up to 2 GHz. The quadrature generation is accomplished on-chip by passive components.

The general considerations about the design of frequency-converting devices elaborated in chapter 4 also apply to the I/Q receiver front-end. This chapter therefore starts with detailed analyses of the implemented circuits. Measurement results are reported at the end of this chapter. The achievements are finally summarized and compared to state-of-the-art.

5.1 Receiver Front-End Design

The quadrature receiver front-end implemented is shown in figure 5.1. It has single-ended RF and LO interfaces and differential IF outputs that are in quadrature. The RF signal is amplified by a single-ended three-stage low-noise amplifier (LNA). The benefit of a single-ended design for the amplifier at this stage of the receiver chain is the resulting low system noise figure, see section 4.1. After amplification, the RF signal is distributed to two branches by an RF splitter and converted from a single-ended to a differential signal using an LC balun. This type of balun was presented in detail in section 4.1.3, the only differences regarding its implementation are the component values. The differential RF signal is fed to the RF pair of the Gilbert cell. On the LO side, the in-phase/quadrature (I/Q) generation is accomplished by a branchline coupler [Pozar 01]. The same type of LC balun as in the RF path is used for the single-ended to differential conversion, but with different component values. An LO buffer is implemented

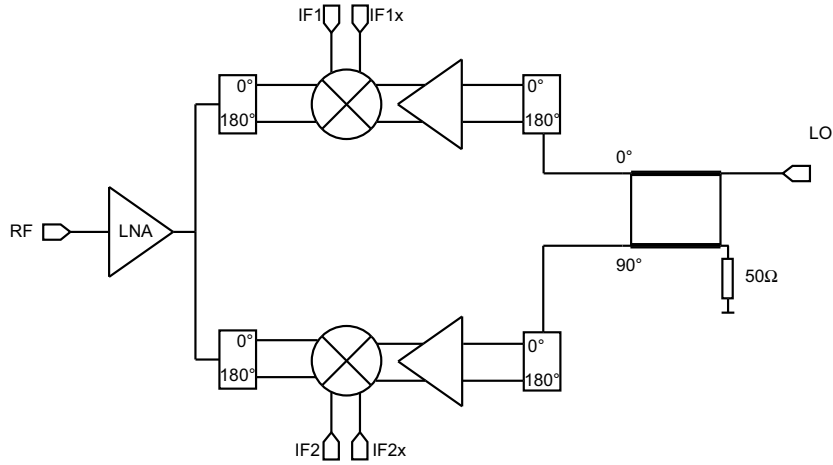


FIGURE 5.1: Overview of the implemented I/Q receiver front-end.

to overcome the losses of the branchline coupler and to guarantee low LO input power levels. The amplified LO signal is then applied to the switching transistors of the Gilbert cell. The I/Q receiver front-end works from a supply voltage of 5.5 V.

5.1.1 Low-Noise Amplifier

The LNA is the first stage in the receiver chain. According to Friis' formula [Friis 44], it dominates the system noise figure if its gain is high enough to make the noise contributions of the subsequent stages negligible.

A single-ended design was implemented. It consists of three amplifier stages. The schematic of the LNA is depicted in figure 5.2. The three stages have similar topologies. The differences between them are the decoupling of the biasing from the signal path and the impedance transformation ratio that determines the load of the transistors in common-emitter configuration, Q_{1-3} in figure 5.2. The first stage is analyzed in detail to explain the functionality of the circuit. The schematic of the first stage is depicted in figure 5.3. The LC network C_2 and T_2 transforms the input impedance of the succeeding stage to the load impedance of Q_1 . The short transmission line T_2 is shorted for high frequencies by the bypass capacitor $C_3 = 3$ pF, therefore it shows inductive behavior. The lengths of the transmission lines between the first and the second stage is $65 \mu\text{m}$, the transmission line between the second and the third stage has a length of $61 \mu\text{m}$. The capacitor values for C_2 are 55 fF between the first and the second stage, and 435 fF between the second and the third stage. The load impedance of the LNA, 50Ω , is transformed to the load impedance of the last transistor by the parasitic pad capacitance C_{pad} , an open stub $T_{\text{stub,out}}$, and a series transmission line ($T_{\text{ser,out}}$). The input of the LNA is matched to 50Ω in the same way.

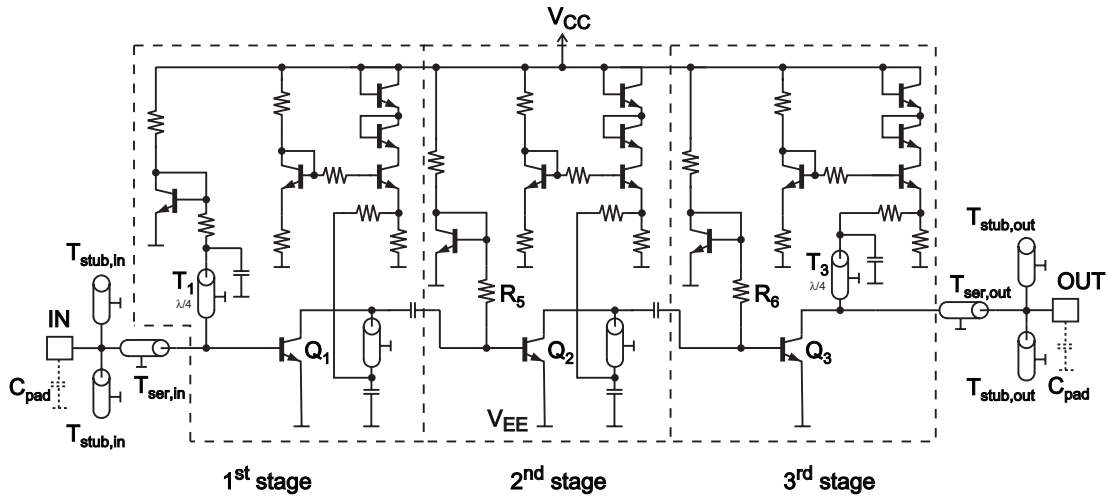


FIGURE 5.2: Schematic of the implemented LNA. $V_{CC} = 5.5 \text{ V}$, $I_{EE} = 32 \text{ mA}$.

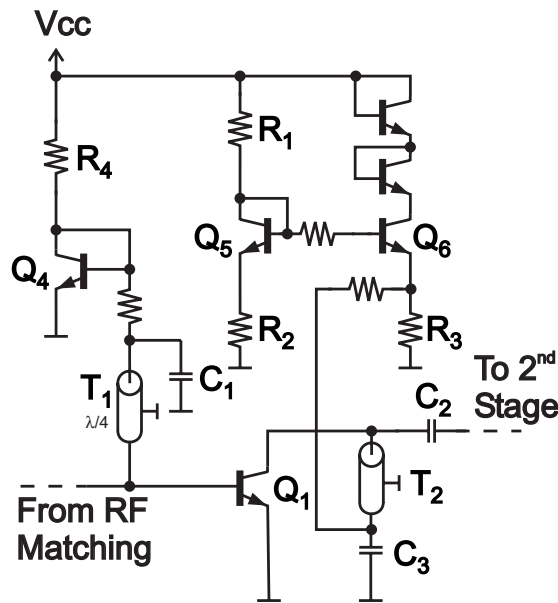


FIGURE 5.3: Schematic of the first stage of the LNA.

The collector potential of Q_1 is held at a constant level of 1.4 V that is deduced from the resistive voltage divider $R_1 = 2800 \Omega$ and $R_2 = 1400 \Omega$. Transistor Q_5 is in diode configuration and serves as a temperature compensation. The collector current of transistor Q_1 is provided by emitter follower Q_6 and fed to Q_1 via T_2 . In the last stage, T_2 is replaced by a shorted $\lambda/4$ (at 80 GHz) transmission line, T_3 in figure 5.2. The collector current is 6.38 mA in the first stage, and 6.54 mA in the second and the third stages.

Transistors Q_1 and Q_4 are in a current mirror configuration that provides the

base bias current. Transmission line T_1 decouples the biasing network from the signal path. The length of this transmission line is $\lambda/4$ at 80 GHz, $480 \mu\text{m}$. This line is shorted for high frequencies by capacitor $C_1 = 4 \text{ pF}$. In the second and the third stage, T_1 is replaced by 500Ω resistors, R_5 and R_6 in figure 5.2. A quarter-wavelength transmission line is used in the first stage because of its superior noise performance. A transmission line injects negligible thermal noise, and capacitor C_1 additionally shunts high-frequency noise components from the biasing. The current in the reference branch of the current mirror is 1.41 mA in all three stages. The three-stage LNA as shown in figure 5.2 works from a supply voltage of 5.5 V and consumes 32 mA .

Input and Output Matching

A tradeoff between power matching and noise matching must be found for the design of the LNA's matching network. The impedance levels for maximum power transfer and minimum noise factor are usually different. While power matching requires complex conjugate input load impedance and output source impedance, noise matching necessitates a source admittance equal to the optimum source admittance for noise matching $Y_{s,\text{opt}} = G_{s,\text{opt}} + jB_{s,\text{opt}}$, given by [Haus 60],

$$G_{s,\text{opt}} = \sqrt{\frac{G_u + R_n G_\gamma^2}{R_n}}, \quad (5.1) \quad \text{and} \quad B_{s,\text{opt}} = -B_\gamma. \quad (5.2)$$

The equivalent noise conductance G_u determines the equivalent noise current fluctuations. The equivalent noise current fluctuations and the equivalent noise voltage fluctuations, determined by the noise resistance R_n ¹, are not correlated. The admittance $Y_\gamma = G_\gamma + jB_\gamma$ connects the correlated noise currents and voltages of the LNA.

A general source admittance $Y_s = G_s + jB_s$ results in a noise factor [Haus 60]

$$F = F_{\min} + \frac{R_n}{G_s} |Y_s - Y_{s,\text{opt}}|^2, \quad (5.3)$$

where F_{\min} is the minimum noise factor. This equation shows that different source admittances result in the same noise factor if the magnitude of their deviation from the optimum source admittance for noise matching is the same. These admittances therefore lie on circles in the Smith-chart.

A general expression for the minimum noise factor of a bipolar transistor is given by [Niu 05]

$$F_{\min} = 1 + \frac{1}{\beta} + \sqrt{\frac{2g_m R_n}{\beta} + \frac{2R_n(\omega C_i)^2}{g_m} \left(1 - \frac{1}{2g_m R_n}\right)}, \quad (5.4)$$

¹The mean equivalent noise current is given by $\overline{i^2} = 4kT_0 B G_u$, the mean equivalent noise voltage by $\overline{v^2} = 4kT_0 B R_n$

where $C_i = C_{BE} + C_{BC}$. This equation shows that the minimum achievable noise figure does not scale directly with the size of the transistor. An increase in transistor size results on the one hand in a reduction of the base resistance, r_b , thus in a decrease of $R_n = r_b + \frac{1}{2g_m}$. On the other hand, capacitances C_{BE} and C_{BC} are increased. Therefore, the factor that determines the minimum achievable noise figure is the technology. Here, SiGe has many advantages, since large current gains β , small transit times (equal to a small C_i), and small base resistances r_b can be realized simultaneously.

The simulated minimum noise figure of the LNA is 5.27 dB at 79 GHz for an optimum input impedance of $Z_{s,opt} = (10.34 + j10.33) \Omega$. This corresponds with an input admittance $Y_{s,opt} = (0.048 + j0.048) S$. Figure 5.4 shows the circles of constant noise figure. It is shown in [Yau 06] that the value for minimum noise

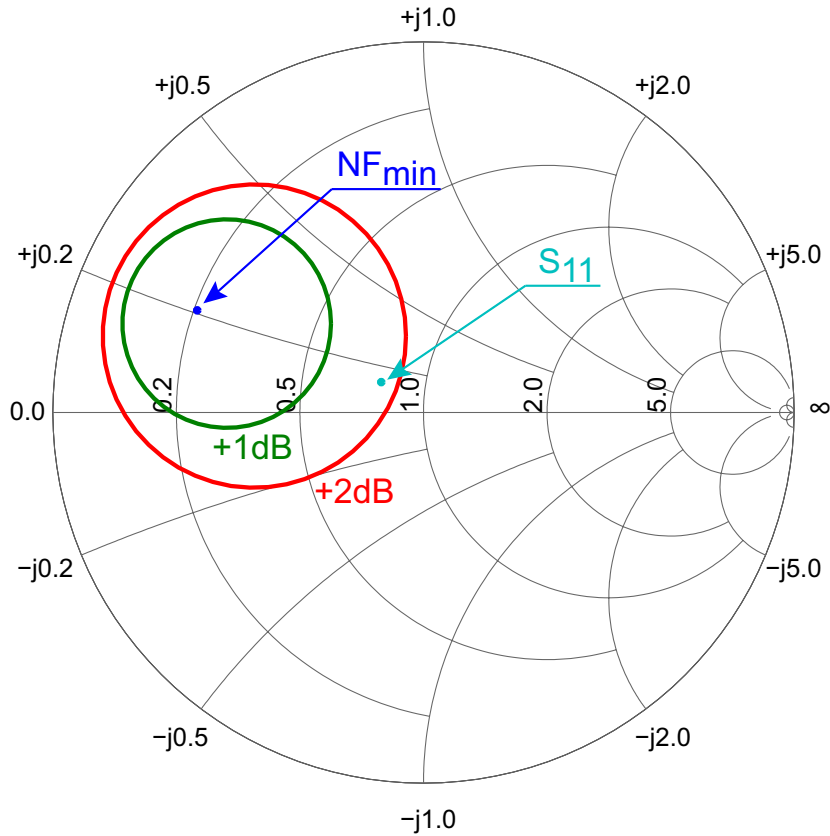


FIGURE 5.4: Circles of constant noise figure ($NF_{min} + 1$ dB, $NF_{min} + 2$ dB) for the LNA without input matching elements at 79 GHz. $NF_{min} = 5.27$ dB, $Y_{s,opt} = (0.048 + j0.048) S$. S_{11} shows the input impedance of the implemented LNA (including matching elements and pad parasitics), $(39.27 + j6.58) \Omega$.

figure received from classic noise models is too pessimistic for high frequencies. High operational frequencies necessitate to account for the correlation between the shot noise associated with base current and the shot noise associated with

collector current in the transistor. In the cited paper, the limit where noise correlation must be accounted for is 18 GHz for a process with an f_T and an f_{\max} of 160 GHz in each case. This correlation is not included in the transistor model of the used technology.

The approach presented in [Yau 06] to determine the minimum noise figure and optimum source admittance for noise matching is unverified for the technology the circuits are implemented in. Thus, the circuit is matched more closely to the power-matching impedance, $50\ \Omega$, than to the simulated noise-matching impedance. The simulated input impedance of the LNA including matching elements and pad parasitics is $(39.27 + j6.58)\ \Omega$ at 79 GHz, labeled S_{11} in figure 5.4.

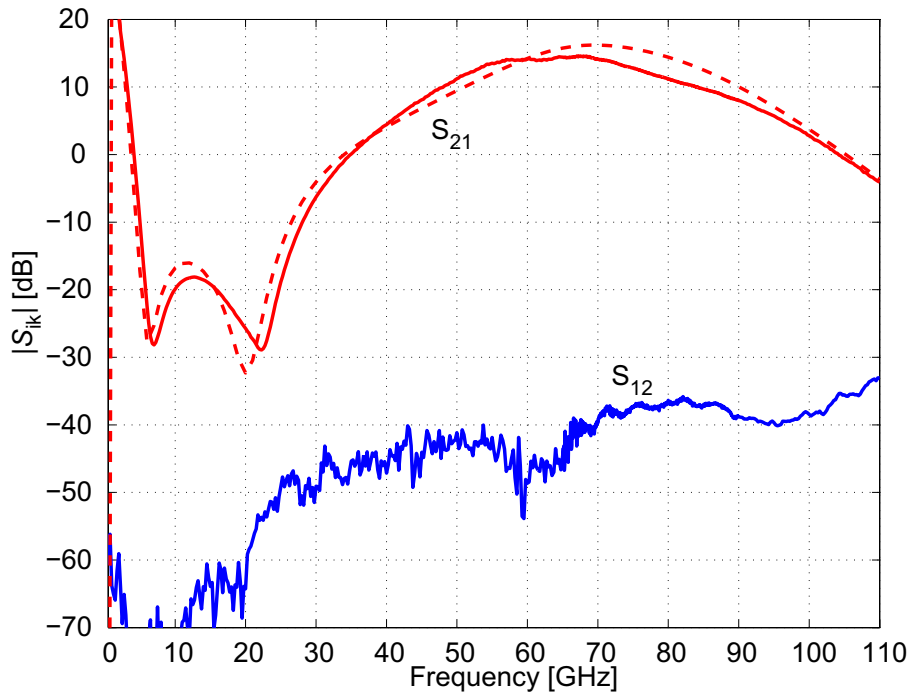
The output impedance of the LNA is designed for power matching since reflections at this interface deteriorate the overall gain of the front-end. The simulated output impedance of the LNA including matching elements and pad parasitics is $(41.16 + j5.8)\ \Omega$ at 79 GHz.

***S*-Parameters**

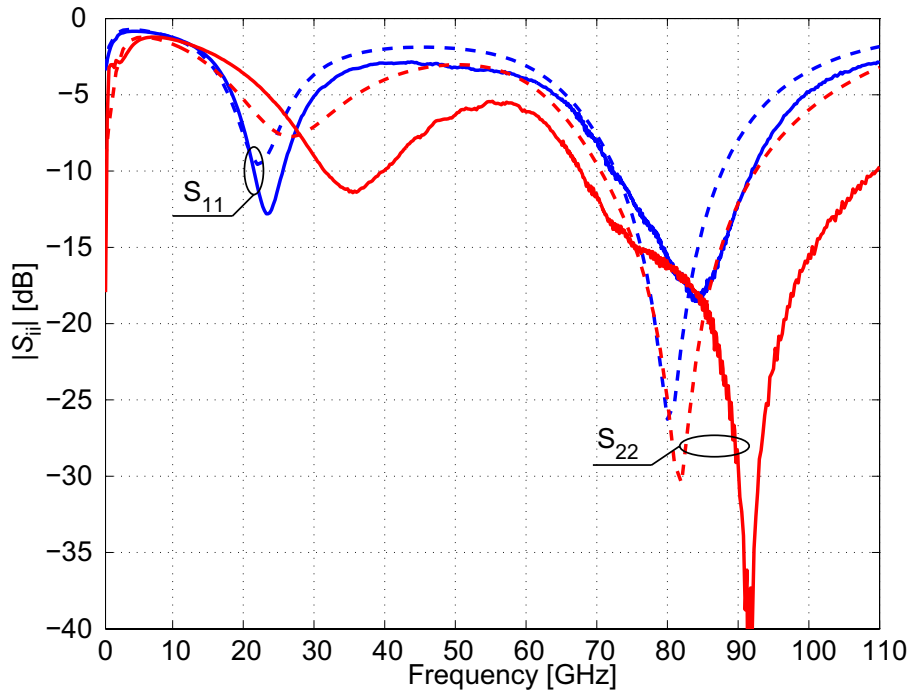
A stand-alone version of the LNA was implemented on a separate chip. This LNA was characterized by *S*-parameter measurements. The results are used to verify the simulation results of input and output matching, gain, and stability.

For the *S*-parameter measurement of the LNA, the chip was glued on a Rogers 4003[®] substrate. The power supply pads were wedge-wedge bonded to the metalization because the *S*-parameter prober station does not have space for biasing probes. The signal pads were contacted with probes directly, so no deembedding of bond wires or other parasitic elements (transmission lines, vias, etc.) had to be done. Due to the lack of on-wafer calibration elements, a SOLT calibration with millimeter-wave standards on a ceramic was performed. The measured *S*-parameters of the stand-alone three-stage LNA are depicted in figure 5.5. The simulated results are shown in the same plots as dashed lines. The measured gain of the LNA in the target frequency band, 77 to 86 GHz, lies between 12 and 9.5 dB. Figure 5.5(a) shows excellent agreement between the simulations and the measurement. The largest discrepancy between measurement and simulations is 3 dB at 80 GHz. The isolation, S_{12} , is determined by parasitic coupling effects, like substrate coupling or coupling over the supply. This could not be simulated with acceptable efforts, so only measurement results are shown. The isolation is better than 35 dB over the whole measurement range.

The measured input and output matching of the LNA, $|S_{11}|$ and $|S_{22}|$, are shown in figure 5.5(b). The measured and the simulated S_{11} are in good agreement. Taking $S_{11,22} < -10$ dB as the matching condition, which is equivalent to a VSWR of 2 : 1, the LNA is matched at the input from 72 to 92 GHz, and at the output from 68 up to 100 GHz. The measured output matching deviates substantially from the simulated results. The causes for this behavior are unknown. Since the matching of the output is better than -14 dB over the target frequency range,



(a) Gain (S_{21}) and isolation (S_{12}).



(b) Input (S_{11}) and output (S_{22}) matching.

FIGURE 5.5: Measured (solid lines) and simulated (dashed lines) S -parameters of the stand-alone LNA. Figure 5.5(a) shows the gain and the isolation, and figure 5.5(b) the input and output matching.

reflections between the output of the LNA and the RF interface of the I/Q mixer are not to be expected. No deviation of the front-end's noise figure or conversion gain from the simulated results should arise from this interface.

Stability

An indicator for the stability of a circuit is Rollet's K-factor and the stability measure.

The K-factor of a linear two-port is defined as [Rollett 62]

$$K = \frac{1 - |S_{11}|^2 - |S_{22}|^2 + |\Delta|^2}{2|S_{12}S_{21}|} \quad (5.5)$$

where $\Delta = S_{11}S_{22} - S_{12}S_{21}$ is the determinant of the S -matrix. The stability measure is

$$B = 1 + |S_{11}|^2 - |S_{22}|^2 - |\Delta|^2 \quad (5.6)$$

The necessary and sufficient conditions for unconditional stability are that the stability factor is larger than unity and the stability measure is positive. A single expression for unconditional stability was introduced in subsection 4.2.3. The μ factor gives the minimum distance of the stability circle from the origin of the Smith-chart [Edwards 92].

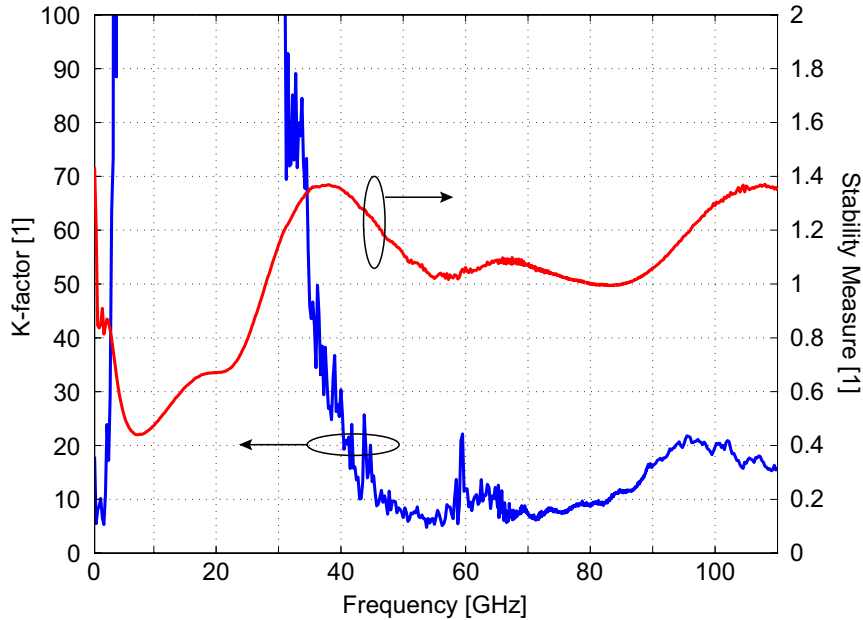


FIGURE 5.6: Rollet's K-factor and the stability measure of the LNA. For unconditional stability, K must be larger than 1 and the stability measure must be positive over the entire frequency range.

The Rollet factor and the stability measure are calculated from the S -parameter measurement of the stand-alone version of the LNA. The results are depicted in figure 5.6. The LNA is unconditionally stable from DC to 110 GHz.

5.1.2 I/Q Mixer

A detailed block diagram of the I/Q mixer is shown in figure 5.7. The paths of

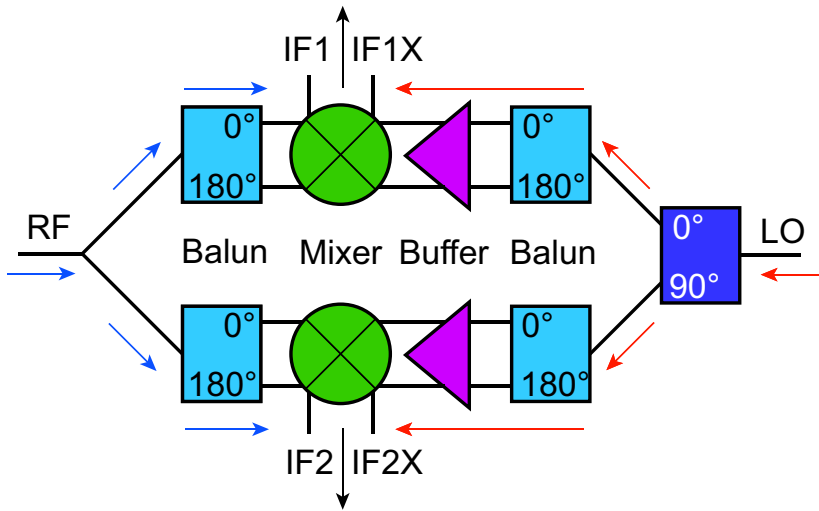


FIGURE 5.7: Block diagram of the implemented I/Q mixer.

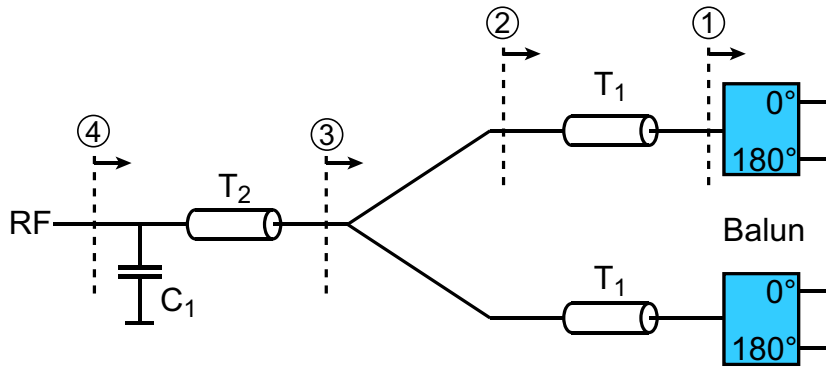
the RF and the LO signals are marked by blue and red arrows, respectively. At the RF port of the mixer, the single-ended signal is first split to two branches of equal power. The resulting two RF signals are converted to differential signals using the same types of LC balun as described in section 4.1.3.

The LO signal is fed to an I/Q generator that consists of a branchline coupler. The single-ended in-phase and quadrature signals are then converted to differential signals using LC baluns. A differential LO buffer amplifies the LO signal and provides DC biasing for the switching transistors of the Gilbert cell.

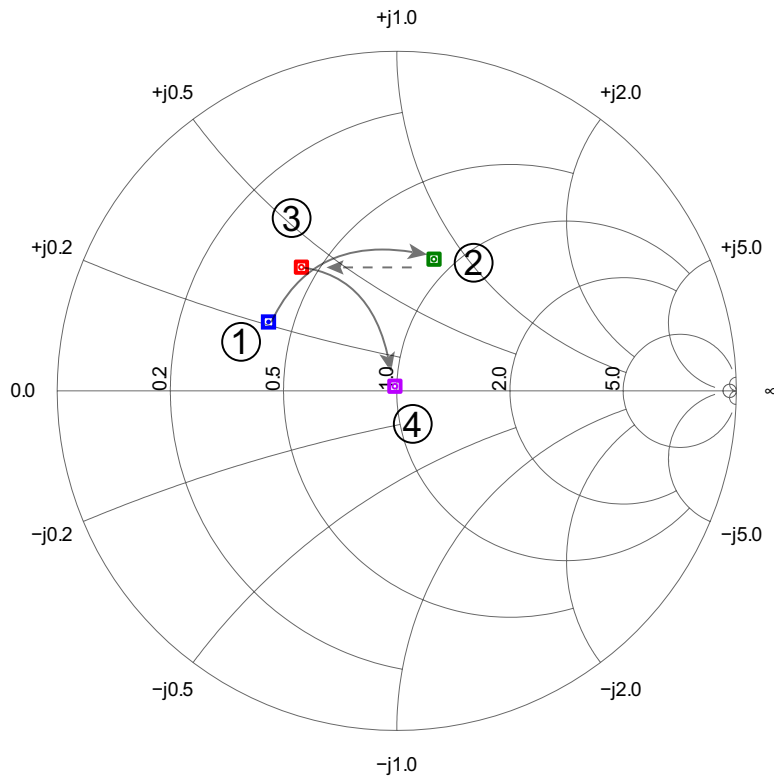
The down-conversion block is implemented as a Gilbert-type mixer core. The IF output signals are differential.

RF Interstage Matching

The RF signal is fed to both in-phase and quadrature mixers by splitting the RF path into two branches of equal impedance. This procedure is illustrated in figure 5.8 for a frequency of 80 GHz. The starting point of the matching procedure is the input impedance of the RF LC balun, $(20.13 + j10.51) \Omega$. This point is marked by ① in figure 5.8. Transmission line T_1 transforms this impedance to



(a) RF power splitting and interstage matching.



(b) Smith-chart representation of the interstage matching. The reference impedance is $Z_0 = 50 \Omega$, and $f_{RF} = 80 \text{ GHz}$.

FIGURE 5.8: RF signal distribution to the in-phase and the quadrature down-conversion mixers.

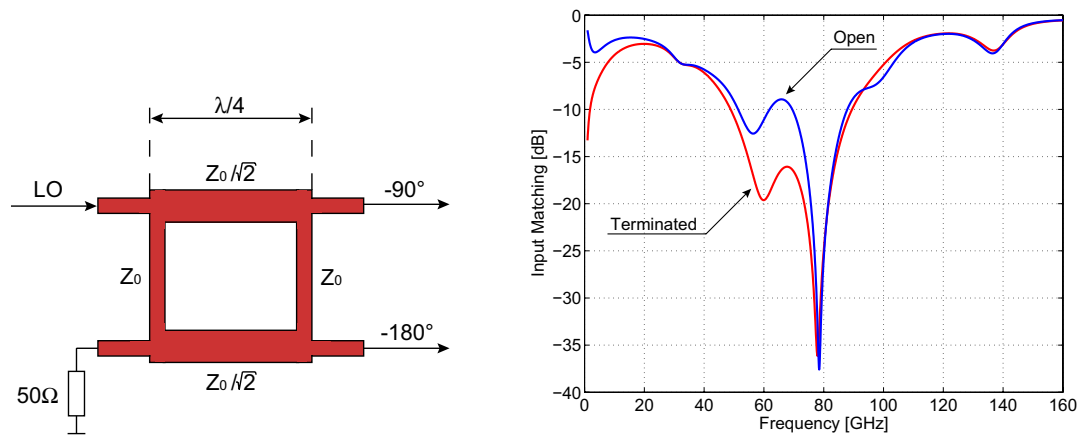
the value $(42.71 + j41.77) \Omega$ at point ②. The parallel connection of both branches results in half the value of these impedances, $(21.35 + j20.89) \Omega$ at point ③. This point is now matched to the 50Ω output impedance of the LNA by an LC matching network. The exact input impedance value at point ④ is $(50.09 + j3.76) \Omega$.

This type of RF splitting is preferred to conventional power splitting using a Wilkinson divider because it occupies less space. The largest components are

the two transmission lines T_1 with lengths of $220\ \mu\text{m}$ each. For comparison, a Wilkinson power divider incorporates two transmission lines with lengths of $\lambda/4 = 480\ \mu\text{m}$ (at $80\ \text{GHz}$) each. In addition, the isolation of the two RF mixer ports that is provided by a Wilkinson divider is not needed.

I / Q Generation

A branchline coupler is used to generate the LO signals that are 90° out-of-phase [Pozar 01]. This type of coupler is depicted in figure 5.9(a). The single-ended LO



(a) Branchline coupler. $Z_0 = 50\ \Omega$, $Z_0/\sqrt{2} = 35.3\ \Omega$, $\lambda/4 = 480\ \mu\text{m}$ at $f_{\text{RF}} = 80\ \text{GHz}$.

(b) Impact of the termination of the isolated port on the input matching at the LO port.

FIGURE 5.9: I / Q generator.

signal is fed to the port labeled LO at the left-hand side. The I / Q output ports are on the right-hand side of the coupler. The remaining port on the left-hand side is isolated from the input signal. Under ideal circumstances, which means no signal is reflected from the ports on the right-hand side of the coupler, this port can be left open. For real implementations, this port should be terminated with the characteristic impedance of the branchline coupler ($50\ \Omega$ for the presented system). Taking again $-10\ \text{dB}$ as the matching condition, the bandwidth of the coupler's input matching is thereby greatly enhanced, from $18.5\ \text{GHz}$ without termination to $42\ \text{GHz}$ with termination. This is illustrated in figure 5.9(b). The plot shows the simulated matching of the LO port in the receiver front-end with the isolated port left open and terminated with $50\ \Omega$.

The branchline coupler was designed using a lumped model for the transmission lines. This model is based on the physical properties of the transmission line. It uses the effective dielectric constant, ϵ_{eff} , and the attenuation coefficient, α . Details on this model are described in section 3.4. Neither T-junctions nor corners or parasitic coupling were modeled. They can be neglected in the design process

since the width w of the transmission lines is much smaller than their length l , $w \ll l$.

Any imbalances in the output I/Q signals, like phase errors or conversion gain inequalities of the two differential IF outputs, can be traced back to mismatches in the branchline coupler. The implemented circuits, like the LO buffers or the mixers, are perfectly symmetric, and process variations are usually negligible on the same die.

LO Buffer

The LO Buffer amplifier lowers the minimum LO power level needed to operate the mixer. It also provides the biasing for the switching transistors in the Gilbert cell. A schematic of the buffer amplifier is depicted in figure 5.10. The topology

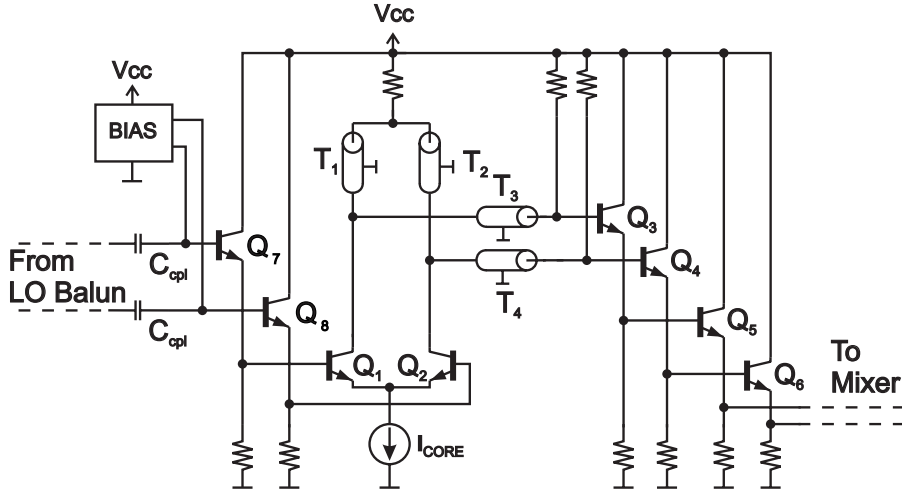


FIGURE 5.10: Schematic of the LO buffer amplifier. $V_{CC} = 5.5$ V, $I_{EE} = 60$ mA.

of the amplifier is fully differential. It consists of emitter followers Q_{3-8} and an emitter-coupled pair, $Q_{1,2}$ in figure 5.10. Emitter followers $Q_{7,8}$ provide a high-impedance load to the balun. They drive the differential pair that consists of transistors $Q_{1,2}$. Transistors $Q_{1,2}$ operate on a tuned load that is a parallel resonant circuit. Transmission lines $T_{3,4}$ (length = $314 \mu\text{m}$ each) transform the differential input impedance of the first emitter follower stage $Q_{3,4}$, $(125.45 - j207.73) \Omega$ at 80 GHz, to $(23.96 - j18.05) \Omega$. The shunt transmission lines $T_{1,2}$ (length = $120 \mu\text{m}$ each) exhibit a differential input impedance of $(3.34 + j42.13) \Omega$ at 80 GHz. Both branches in parallel result in an impedance of $(34.56 + j4.28) \Omega$. In addition, a resistor of 100Ω (not shown in the figure) is included between the collectors of the differential amplifier to prevent instability. This resistor, its parasitic capacitance, and the parasitic capacitances at the collectors of transistors $Q_{1,2}$ contribute to the load of the differential pair, which is $(26.92 + j2.27) \Omega$.

Another option for the implementation of the LO buffer is a differential pair in cascode configuration. Compared with the tuned load, the cascode has the advantage of a broader bandwidth. Since the bandwidth requirements are equivalently fulfilled by the implementation using a tuned load, this option was chosen.

Figure 5.11 shows the simulated voltage gain of the LO buffer amplifier including the balun. The output of the amplifier is the differential voltage at the switching transistors of the Gilbert cell and the input is the single-ended signal at the input of the balun. The amplifier also serves as a limiter for high LO power levels

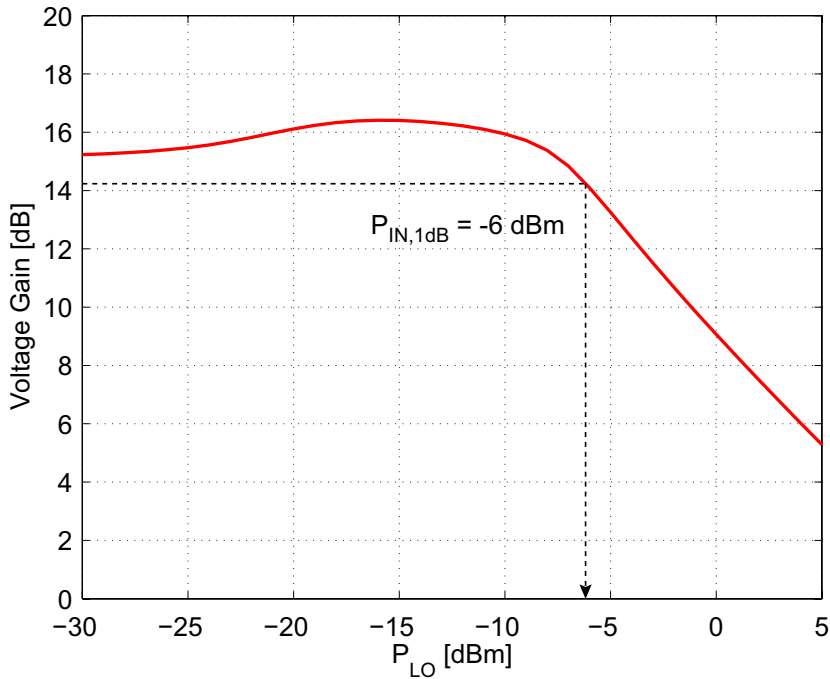


FIGURE 5.11: Simulated voltage gain of the LO buffer amplifier including the balun. $f_{LO} = 80$ GHz.

that would deteriorate the linearity of the front-end, see section 4.2.1. Therefore, the combination of the amplifier and the balun exhibit an input-referred 1 dB compression point of -6 dBm.

Measurements show that the minimum LO power level for constant single-sideband noise figure and conversion gain of the I/Q receiver front-end is -7 dBm.

Mixer Circuit Design

The down-conversion mixers are implemented using standard Gilbert-type mixer cores. The schematic of one mixer is depicted in figure 5.12. Emitter-coupled pairs ($Q_{5,6}$) are used for the RF differential amplifiers. No degeneration is necessary due to the relaxed linearity requirements. The tail current $I_{CORE} = 6$ mA is

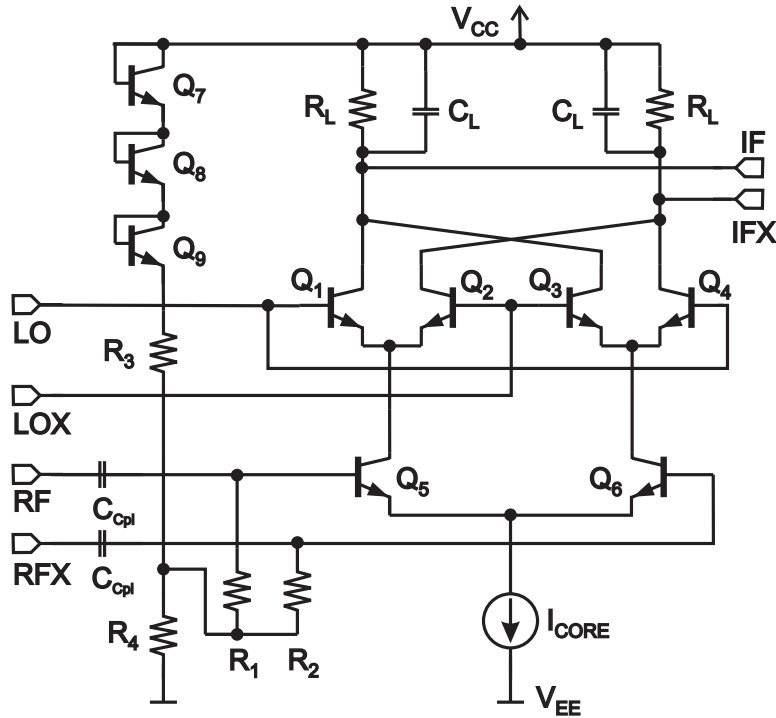


FIGURE 5.12: Schematic of the Gilbert-type down-conversion mixer. $V_{CC} = 5.5\text{ V}$, $I_{EE} = 8\text{ mA}$.

provided by a current mirror. The biasing of the RF transistors consists of three level-shifting transistors in diode configuration (Q_{7-9}) and a resistive voltage divider ($R_3 = 320\ \Omega$, $R_4 = 1200\ \Omega$). It is decoupled from the RF signal path by $500\ \Omega$ resistors per path ($R_{1,2}$). The biasing of the LO switching transistors (Q_{1-4} in figure 5.12) is provided by the LO buffer amplifier, see section 5.1.2. Obeying the considerations presented in section 4.1, the speed of the switching transistors mainly determines the overall performance of the mixer. Therefore they are operated at the current density that results in highest f_T , $7\text{ mA}/\mu\text{m}^2$. In the target application, the front-end will be followed by an A/D converter with an input impedance much higher than the internal load of the mixer. Thus, the load impedance of the Gilbert cell consists of the internal combination of the load resistors R_L ($2 \times 400\ \Omega$) and the blocking capacitors C_L ($2 \times 200\ \text{fF}$) only. This results in an upper frequency limit for the IF of 1.99 GHz.

5.2 Measurement Results

The I/Q receiver front-end was fabricated in the technology presented in chapter 3. A chip photograph is depicted in figure 5.13. The RF input is on the left-hand side. It is a ground-signal-ground (GSG) configuration. This enables the use of GSG probes with low insertion loss (1.2 dB) which results in higher

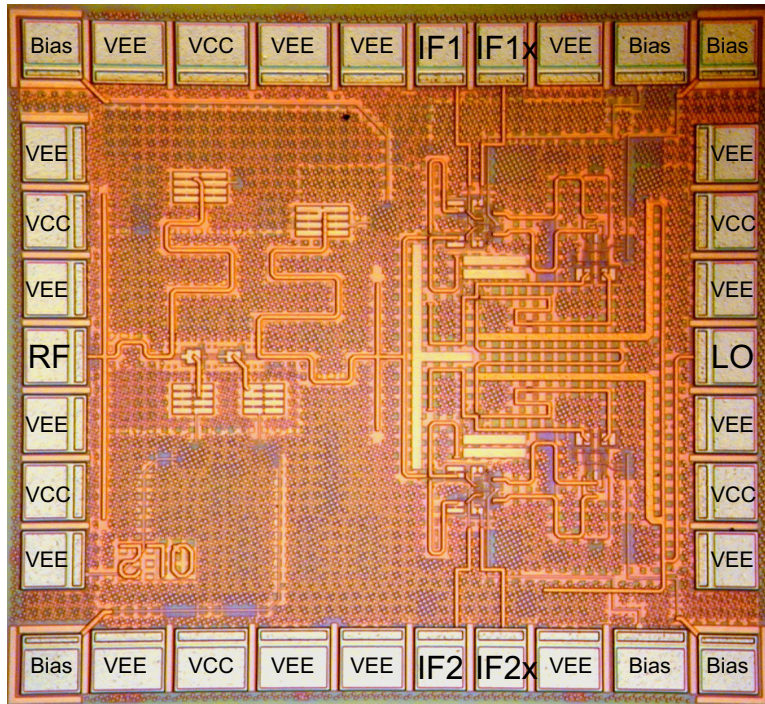


FIGURE 5.13: Die photograph of the implemented I/Q receiver front-end. The chip size is $1000 \times 1100 \mu\text{m}^2$. $V_{CC} = 5.5 \text{ V}$, $I_{EE} = 192 \text{ mA}$.

accuracy for the determination of noise figure and conversion gain than using GS probes. The LO input is located at the right-hand side. Several supply pins, labeled V_{CC} and V_{EE} , facilitate the connection of the power supply. The $0^\circ/90^\circ$ output is taken from the IF/IFX pins at the top and at the bottom of the chip. The current in all stages of the LNA and the current in the mixer cells can be controlled externally by contacting the pins labeled "Bias". For the measurement results presented here, these pins were left open.

The entire left-hand side of the chip is occupied by the LNA. Especially large signal components from the LO buffers are kept away from the LNA by this measure. On the right-hand side, the folded branchline coupler can be clearly identified (thick L-shaped transmission lines). The I/Q mixer is symmetrical about an imaginary horizontal axis through the LO and the RF pins.

Since the frequency range of the receiver front-end and the highly-linear down-conversion mixer presented in chapter 4 is roughly the same, the same measurement setups were used. Refer to section 4.3 for details about the individual setups.

5.2.1 Noise Figure and Conversion Gain

The single-sideband noise figure as well as the conversion gain of the receiver front-end are depicted in figure 5.14. The conversion gain stays between 33 dB at

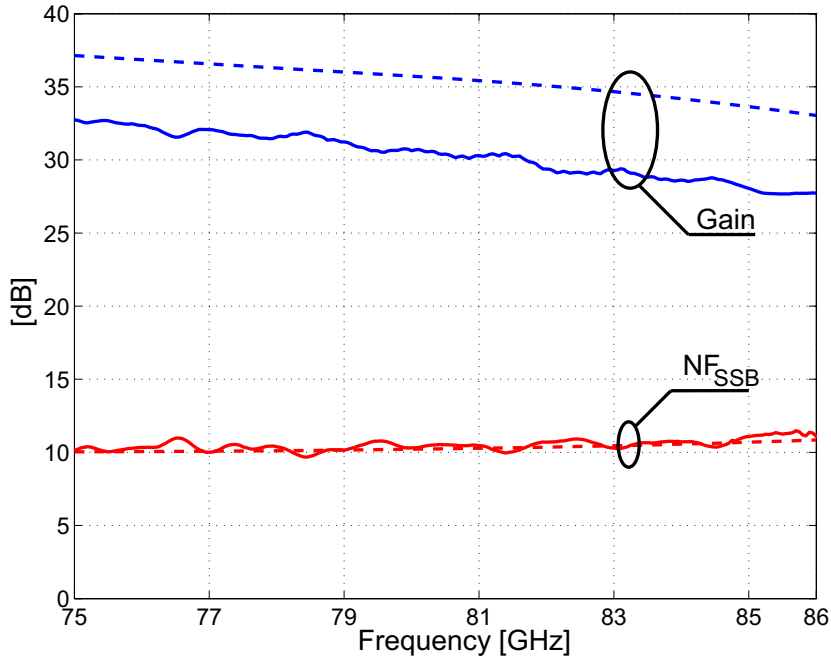


FIGURE 5.14: Measured single-sideband noise figure and conversion gain of the I/Q receiver front-end versus frequency. The noise figure measurement uncertainty is 0.5 dB, the uncertainty in gain measurement 0.54 dB. $P_{LO} = +5$ dBm, $f_{IF} = 10$ MHz.

75 GHz and 28 dB at 86 GHz, the single-sideband noise figure is at most 12 dB at 86 GHz, and reaches 10 dB in the rest of the frequency range. The same plot shows the simulated results, marked by dashed curves. The measured conversion gain deviates by 4 dB from the simulated one over the whole frequency range. Figure 5.5(a) in section 5.1.1 shows that 3 dB are attributed to the LNA. The reason for this behavior is to be found partly in parasitics that have an impact on the impedance transformation process in the LNA. The noise figure from the measurement matches the simulation results quite well. This shows that, according to Friis' formula, the gain of the LNA is still large enough to make the noise contributors from the following stages negligible.

The uncertainty in determination of the single-sideband noise figure and the conversion gain are, according to the formulas derived in section 4.3.1, 0.5 dB and 0.54 dB, respectively. These values are derived from the specifications (3σ) provided in the datasheets of the used components.

The dependence of the noise figure and the conversion gain on the LO power was also determined by measurement. At 79 GHz, the mixer operates from a minimum LO power of -7 dBm.

5.2.2 Linearity

The linearity of the receiver front-end is quantified by the 1 dB compression point and the third-order intercept point.

1 dB Compression Point

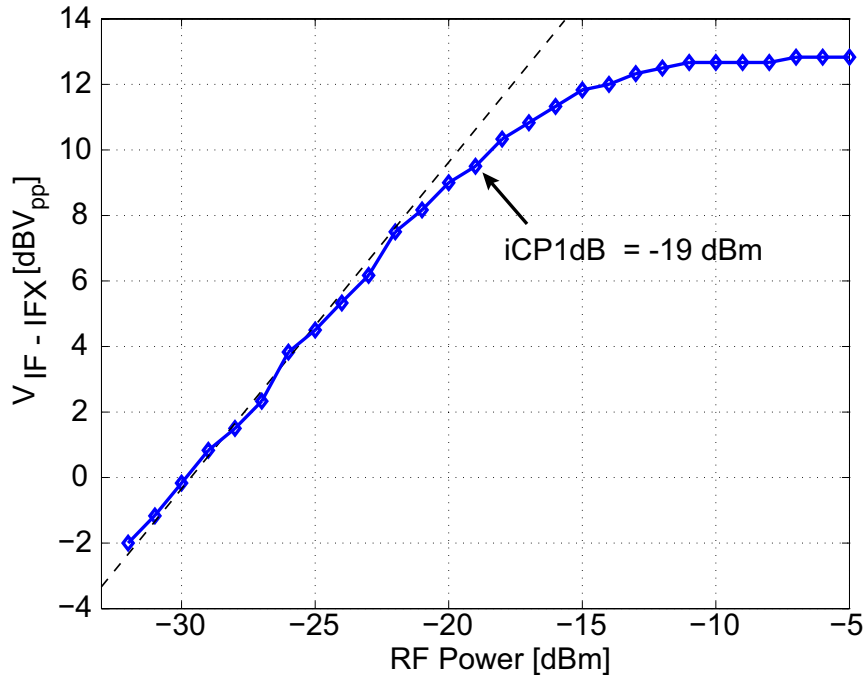


FIGURE 5.15: Measured input-referred 1 dB compression point. $f_{LO} = 79$ GHz, $f_{IF} = 10$ MHz

Figure 5.15 reports on the measured 1 dB compression point. The input-referred 1 dB compression point is -19 dBm. This value is high enough for the intended applications (communication systems and short-range automotive radar). The measurement was performed at the center frequency of short-range automotive radar applications. At higher frequencies, the 1 dB compression point is expected to rise by the same rate as the gain drops, refer to figure 5.14.

Third-Order Intercept Point

The third-order intercept point, IP_3 , was measured at an RF frequency of 80 GHz and an IF frequency of 10 MHz. The second tone for the measurement had a spacing of 200 kHz from the first tone. The measured output voltage levels at the fundamental IF frequency and at the third-order IF frequency versus input power are shown in figure 5.16. The extrapolated lines intersect at the input-referred

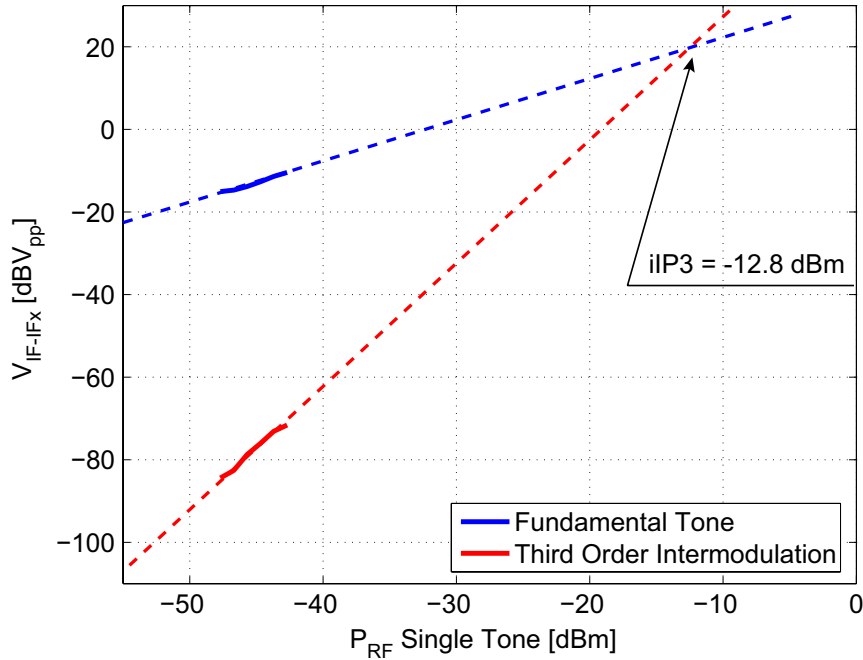


FIGURE 5.16: Measured input-referred third-order intercept point. $f_{LO} = 79.999$ GHz, $f_{RF,1} = 80$ GHz, $f_{RF,2} = f_{RF,1} + 200$ kHz.

IP_3 , which is -12.8 dBm. This value is in good agreement with the simulated result, -10.5 dBm.

5.2.3 I / Q Mismatch

Mismatches in the I / Q output of the front-end have different impacts on the system performance [Razavi 97]:

- In image-rejection architectures, mismatches in the gain and the phase difference result in reduction of image rejection ratio.
- When receiver front-ends are incorporated in communication systems that use higher-order modulation schemes², deviations in phase result in a skewed constellation diagram, thus in increased symbol errors.
- Using higher-order modulation schemes, deviations in conversion gain produce stretched/compressed constellation diagrams, which can also increase the symbol errors.

Although symmetry was kept high throughout the design and the physical implementation, the I / Q generator causes deviations between the simulated and the

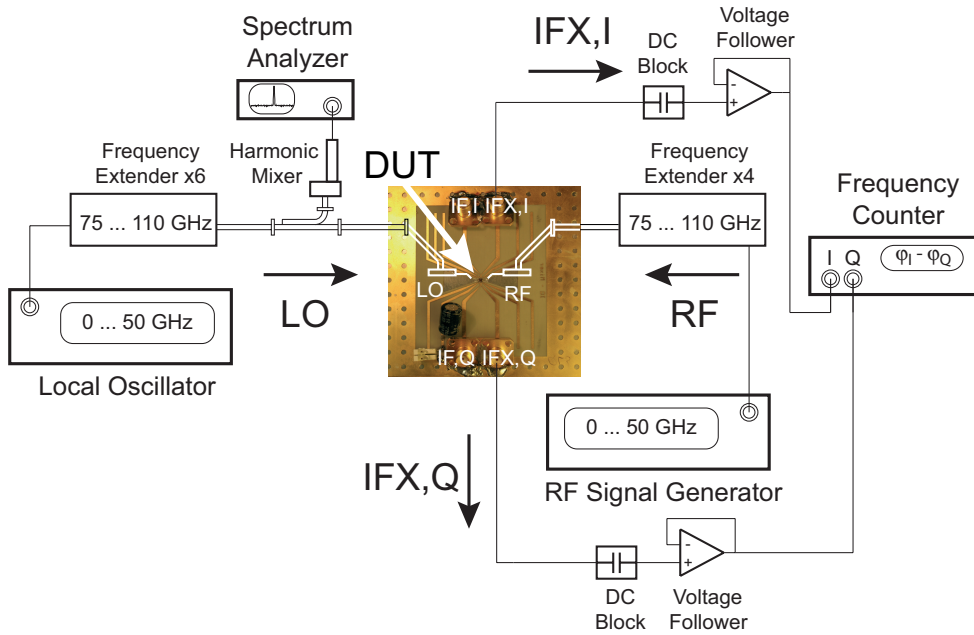


FIGURE 5.17: Setup for the measurement of the I / Q phase difference.

measured results. Figure 5.17 shows the measurement setup for the determination of the I / Q phase imbalance. The receiver front-end was mounted on a PCB for this measurement. The supply pins and the IF outputs were wedge-wedge bonded and connected to on-board SMA connectors. One single-ended output of each I and Q component were fed to a frequency counter with phase measurement capability (Agilent 53132A). The RF and the LO signals were supplied by probes. The measured and the simulated phase difference of the differential I / Q outputs are depicted in figure 5.18. The phase difference stays within $90^\circ \pm 8^\circ$ over the entire frequency range. A total number of 500 measurements was performed per frequency spot. The measured standard deviation of the measured phase difference is $\bar{\sigma} = 1.3^\circ$ per frequency spot. The discrepancy between the measured and the simulated data arises from the used 2D transmission line model. Neither coupling nor corners or junctions of the folded branchline coupler are modeled. Especially coupling is regarded as the cause for the shape of the measured data around 83 GHz.

The ratio of the conversion gain and the single-sideband noise figure of the I and the Q outputs is depicted in figure 5.19. This plot is a result of sequential noise figure and gain measurements. The noise figure ratio of the I and the Q signals is below ± 0.1 dB from 75 to 85 GHz. The gain ratio is lower than ± 0.7 dB over the same frequency range. Regarding the overall measurement uncertainty (roughly 0.5 dB for both noise figure and conversion gain), no significant inequality of either noise figure or conversion gain results from the receiver front-end.

²Higher-order schemes modulate both amplitude and phase of the RF signal.

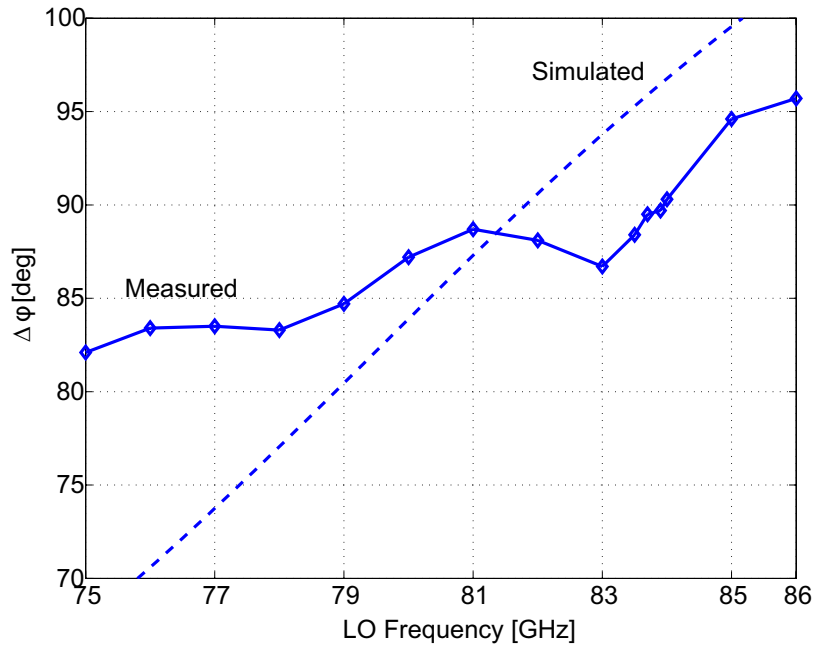


FIGURE 5.18: Phase difference at the I/Q outputs versus input RF frequency. $P_{LO} = +5$ dBm, $f_{IF} = 10$ MHz, 500 averages per frequency, $\bar{\sigma} = 1.3^\circ$.

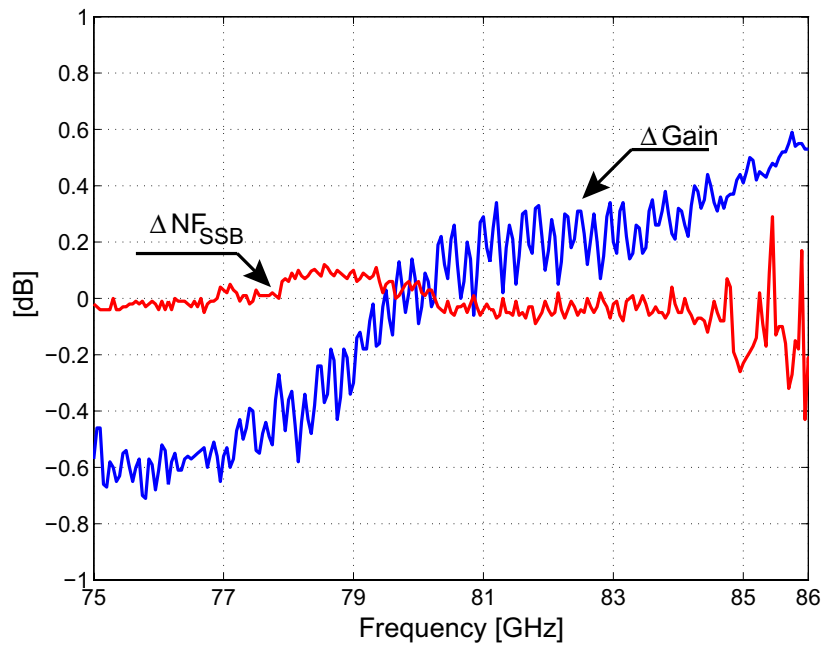


FIGURE 5.19: Measured difference in single-sideband noise figure (ΔNF_{SSB}) and conversion gain ($\Delta Gain$) of the I/Q outputs versus frequency. $P_{LO} = +5$ dBm, $f_{IF} = 10$ MHz.

5.2.4 Temperature Behavior

A plot of the single-sideband noise figure and the conversion gain at 79 GHz versus temperature is shown in figure 5.20. At this frequency, the noise figure rises from

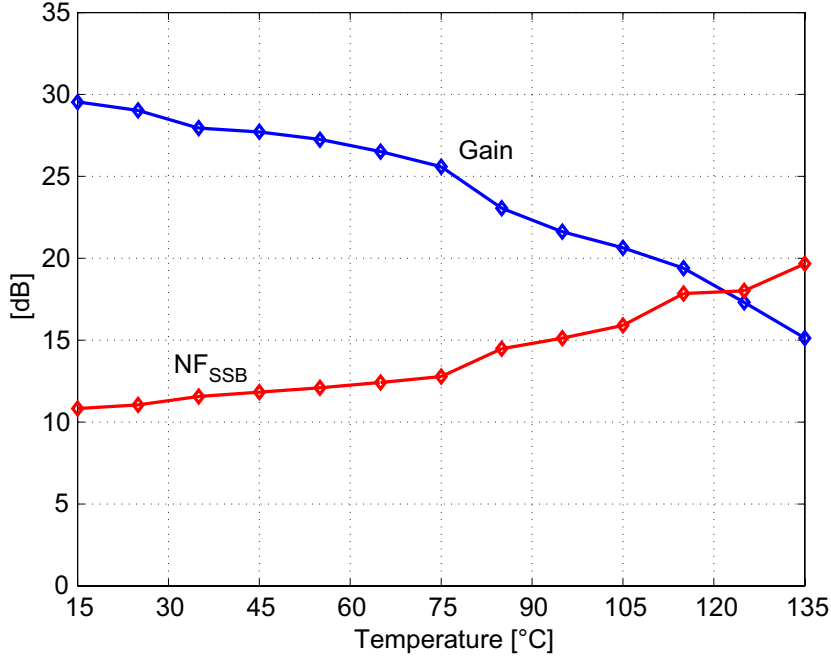


FIGURE 5.20: Dependence of the single-sideband noise figure and the conversion gain on the backside temperature of the chip. $f_{LO} = 79$ GHz, $P_{LO} = +5$ dBm, $f_{IF} = 10$ MHz.

11 dB at 15°C to 20 dB at 135°C. This behavior is explained by the increasing noise figure (refer to equation (5.4)) and the decreasing gain of the transistors over temperature. Due to the decreased gain, the noise contributions from the stages following the LNA become significant. The conversion gain of the LNA at 79 GHz decreases from 30 dB to 15 dB. This is also explained by the decreased gain of the transistors. If thermal compensation were used for the biasing, especially of the LNA, the degradation of the noise figure and the conversion gain could be partly compensated.

5.2.5 Matching and Isolation

The return loss from an S -parameter measurement³ of the RF and the LO ports is depicted in figure 5.21. Taking -10 dB as the boundary for matching, the RF port is matched from 75 to 89 GHz. The matching at the LO port is much broader,

³Strictly speaking, S_{11} is equal to the return loss only for unilateral devices. Taking S_{11} as the return loss results in a negligible error for the circuit presented here.

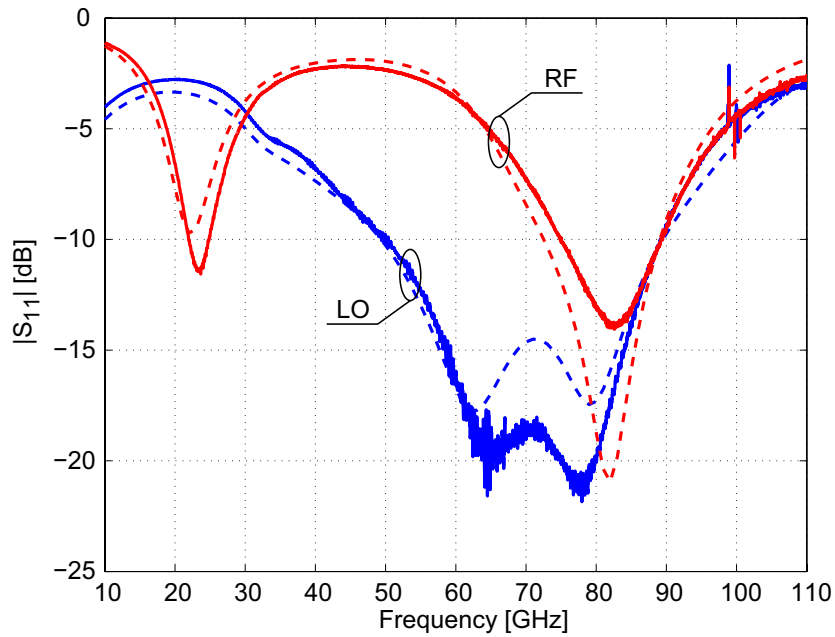


FIGURE 5.21: Return loss at the RF and the LO port of the I/Q receiver front-end. The solid lines represent the measurements, the dashed lines the simulation results.

from 50 to 89 GHz, which is a result of the branch line coupler's properties and the $50\ \Omega$ termination of the isolated port.

The isolation of the RF port from the LO port can also be obtained from S -parameter measurements. An error is made because the LO port is not operated with large signals. From small-signal measurements, the isolation is better than 48 dB in the frequency range 75 to 92 GHz.

TABLE 5.1: State-of-the-art millimeter-wave receiver front-ends.

	Frequency Range [GHz]	NF _{DSB} [dB]	Conversion Gain [dB]	iCP _{1dB} [dBm]	iIP ₃ [dBm]	I/Q Generation	Power Consumption [W]
[Floyd 05]	57–65	13.3	18.6	-17	-7	on-chip	0.149
[Razavi 06]	60	12.5	28	-22.5	–	off-chip	0.009
[Gunnarsson 05]	47–67	–	-8.5	9	19	on-chip	0
[Kaleja 01]	76–77	–	-10	–	–	on-chip	–
<i>This work</i> [Dehlink 06,a]	75–86	9	30	-19	-12.8	on-chip	1.056

5.3 Summary

A quadrature receiver front-end for communication and sensing applications in the 80 GHz frequency range was developed and characterized. The receiver front-end consists of a low-noise amplifier, two down-conversion mixers including LO buffer amplifiers, and an on-chip I/Q generator. The most important performance parameters of the front-end are summarized in table 5.1 and compared to published state-of-the-art I/Q receiver front-ends. The presented front-end shows superior than state-of-the-art performance in terms of noise figure. The conversion gain as well as the linearity are comparable to other publications. The use of 5.5 V, which is a demand from a system architecture point of view, results in a power dissipation much higher than other work. Future developments of the front-end can tackle this problem.

Chapter 6

Conclusion and Outlook

The design, implementation, and characterization of two integrated receiver circuits in SiGe bipolar technology for applications around 80 GHz have been elaborated. The circuits are a single down-conversion mixer and a quadrature receiver front-end. While the intended application of the first IC is a low-cost long-range automotive radar system, the usability of the second IC ranges from communication systems to different implementations of short-range automotive radar systems. The outstanding linearity and the single-sideband noise figure of the down-conversion mixer ($i\text{CP}_{1\text{dB}} = 0 \text{ dBm}$, $\text{NF}_{\text{SSB}} = 16.5 \text{ dB}$), as well as the overall electric properties of the quadrature receiver front-end are superior to published state-of-the-art.

Future work covers, from a circuit design point of view, the reduction of power consumption. A great leap forward is taken by reducing the supply voltage, which necessitates new designs. In addition, the power consumption is reduced in case of the highly-linear down-conversion mixer from chapter 4 by replacing the emitter followers with a differential amplifier, for example, which saves current. The power consumption of the quadrature receiver front-end, chapter 5, is also reduced by improving the LO buffers. From a system point of view, the integration of the receivers and the transmitter on a single chip is the next logical step. Since the simultaneous integration of components with high output power and highly-sensitive components is critical, new challenges will be faced.

A success of the automotive radar business will result in increased interference of the individual systems. This factor can be minimized changing the architecture to spread-spectrum systems. Adding a correlator, a next-generation 79 GHz short-range automotive radar transceiver demonstrator can be built using the spread-spectrum transmitter presented in [Trotta 07,b] together with the quadrature receiver front-end presented in this work.

Bibliography

- [Abidi 03] A.A. Abidi, “General Relations Between IP₂, IP₃, and Offsets in Differential Circuits and the Effects Of Feedback”, *IEEE Transactions on Microwave Theory and Techniques*, vol. 51, pp. 1610–1612, May 2003.
- [Agilent Tech 07,a] Agilent Technologies, *Application Note 57–1: Fundamentals of RF and Microwave Noise Figure Measurements*, available at <http://www.home.agilent.com/>, accessed on 10.02.2007.
- [Agilent Tech 07,b] Agilent Technologies, *Application Note 57–2: Noise Figure Measurement Accuracy – The Y-Factor Method*, available at <http://www.home.agilent.com/>, accessed on 10.02.2007.
- [Agilent Tech 07,c] Agilent Technologies, *Gummel-Poon Bipolar Model: Model Description, Parameter Extraction*, available at <http://eesof.tm.agilent.com/>, accessed on 22.05.2007.
- [Aparin 99] V. Aparin, and C. Persico, “Effect Of Out-Of-Band Terminations On Intermodulation Distortion in Common-Emitter Circuits”, in *International Microwave Symposium (IMS)*, volume 3, pp. 977–980. IEEE, June 1999.
- [Audi AG 07] Audi AG, *Audi Lexikon: Adaptive Cruise Control*, <http://www.audi.de/>, accessed on 23.05.2007.
- [Babkhani 06] A. Babkhani, X. Guan, A. Komijani, A. Natarajan, and A. Hajimiri, “A 77GHz 4-Element Phased Array Receiver with On-Chip Dipole Antennas in Silicon: Transmitter and Local LO-Path Phase Shifting”, *IEEE Journal of Solid-State Circuits (JSSC)*, vol. 41, pp. 2795–2806, Dec. 2006.
- [Bakalski 02] W. Bakalski, W. Simbürger, H. Knapp, H.-D. Wohlmuth, and A.L. Scholtz, “Lumped and distributed lattice-type LC-baluns”, in *International Microwave Symposium (IMS)*, volume 1, pp. 209–212. IEEE, 2002.

- [Barton 98] D.K. Barton, and S.A. Leonov, *Radar Technology Encyclopedia*, Artech House, 1998.
- [Battle 07] L.P. Battle, “Lecture 6 - Noise and Shielding”, in *Lecture Notes EL307*, <http://faculty.capitol-college.edu/>, accessed on 24.05.2007. Capitol College, Maryland, USA.
- [BMW AG 07] BMW AG, *Accessories: Active Cruise Control*, <http://www.bmw.de/>, accessed on 23.05.2007.
- [Böck 04] J. Böck, H. Schäfer, K. Aufinger, R. Stengl, S. Boguth, R. Schreiter, M. Rest, H. Knapp, M. Wurzer, W. Perndl, T. Böttner, and T.F. Meister, “SiGe Bipolar Technology for Automotive Radar Applications”, in *Bipolar/BiCMOS Circuits and Technology Meeting (BCTM)*, pp. 84–87. IEEE, December 2004.
- [Bryant 04] D.T. Bryant, R.A. Eye, J.M. Carroll, and D. Allen, “Integrated LNA-sub-harmonic mixer for 77 GHz automotive radar applications using GaAs pHEMT technology”, in *Compound Semiconductor Integrated Circuit (CSIC) Symposium*, pp. 257 – 259. IEEE, October 2004.
- [Centerline 07] Technologies Centerline, *Materials Properties Chart*, Centerline Technologies; <http://www.centerlinetech-usa.com/pdf/MaterialsPropSing.pdf> (accessed on 30.05.2007), 2007.
- [Citroën 07] Automobiles Citroën, *Lane Departure Warning System - LDWS*, <http://www.citroen.com/CWW/en-US/TECHNOLOGIES/SECURITY/AFIL/>, accessed on 23.05.2007.
- [Cuthbertson 85] A. Cuthbertson, and P. Ashburn, “Self-Aligned Transistors with Polysilicon Emitters for Bipolar VLSI”, *IEEE Journal of Solid-State Circuits*, vol. 20, pp. 162–167, February 1985.
- [DaimlerChrys 07] DaimlerChrysler AG, *Abstandsregeltempomat DISTRONIC PLUS inklusive Bremsassistent BAS PLUS und Parkassistent*, <http://www.mercedes-benz.de/>, accessed on 23.05.2007.
- [Dehlink 05] B. Dehlink, H.-D. Wohlmuth, K. Aufinger, T.F. Meister, J. Böck and A.L. Scholtz “A Low-Noise Amplifier at 77 GHz in SiGe:C Bipolar Technology”, in *Compound Semiconductor Integrated Circuit (CSIC) Symposium*, pp. 287–290, Palm Springs, USA, Oct – Nov 2005. IEEE.

- [Dehlink 06,a] B. Dehlink, H.-D. Wohlmuth, K. Aufinger, F. Weiss, and A.L. Scholtz “An 80 GHz SiGe Quadrature Receiver Frontend”, in *Compound Semiconductor Integrated Circuit (CSIC) Symposium*, pp. 197–200, San Antonio, USA, Nov 2006. IEEE.
- [Dehlink 06,b] B. Dehlink, H.-D. Wohlmuth, H.P. Forstner, H. Knapp, S. Trotta, K. Aufinger, T.F. Meister, J. Böck and A.L. Scholtz, “A Highly Linear SiGe Double-Balanced Mixer for 77 GHz Automotive Radar Applications”, in *Radio Frequency Integrated Circuits (RFIC) Symposium*, pp. 205–208. IEEE, Jun 2006.
- [Dehlink 07] B. Dehlink, M. Engl, K. Aufinger, and H. Knapp “Integrated Bandpass Filter at 77 GHz”, *IEEE Microwave and Wireless Components Letters*, vol. 17, pp. 346–348, May 2007.
- [Edwards 92] M.L. Edwards, and J.H. Sinsky, “A New Criterion for Linear 2-Port Stability Using a Single Geometrically Derived Parameter”, *IEEE Transactions on Microwave Theory and Techniques*, vol. 40, pp. 2303–2311, December 1992.
- [Electronic 07] Telemeter Electronic, *Microstrip Antenna 76 GHz for Automotive Radar (Electron Scanning)*, D-86609 Donauwörth, <http://www.telemeter.de/>, accessed on 24.05.2007.
- [ERC 07] European Radiocommunications Committee ERC, “The European Table of Frequency Allocations and Utilisations covering the frequency range 9 kHz to 275 GHz”, in *www.ero.dk/eca-change*, accessed on 21.05.2007.
- [FCC 02] FCC, “Ultra-Wideband Transmission Systems”, in *Federal Register*, pp. 34852 – 34860. Federal Communications Commission (FCC), National Archives and Records Administration (NARA), May 2002.
- [Filimon 00] V. Filimon, and J. Buechler, “A Pre-Crash Radar Sensor System Based on Pseudo-Noise Coding”, in *International Microwave Symposium (IMS)*, pp. 1415 – 1418. IEEE, June 2000.
- [Floyd 05] B.A. Floyd, S.K. Reynolds, U.R. Pfeiffer, T. Zwick, T. Beukema, and B. Gaucher, “SiGe bipolar transceiver circuits operating at 60 GHz”, *IEEE Journal of Solid-State Circuits (JSSC)*, vol. 40, pp. 156 – 167, January 2005.

- [Fong 98] K.L. Fong, and R.G. Meyer, “High-Frequency Nonlinearity Analysis of Common-Emitter and Differential-Pair Transconductance Stages”, *IEEE Journal of Solid-State Circuits (JSSC)*, vol. 33, pp. 548–555, Apr 1998.
- [Friis 44] H.T. Friis, “Noise Figures of Radio Receivers”, *Proceedings of the IRE*, vol. 32, pp. 419–422, July 1944.
- [Fujushima 06] M. Fujushima, B.B.M. Wasanthamala Badalawa, A. Öncü, and T. Wang, “22-29 GHz CMOS Pulse Generator for Ultra-Wideband Radar Application”, in *European Solid State Circuits Conference (ESSCIRC)*, pp. 279–282. IEEE, Sept. 2006.
- [Gilbert 68] B. Gilbert, “A precise four-quadrant multiplier with subnanosecond response”, *IEEE Journal of Solid-State Circuits (JSSC)*, vol. 3, pp. 365–373, Dec. 1968.
- [Gilbert 95] B. Gilbert, “Mixer Fundamentals and Active Mixer Design”, in *RF IC Design for Wireless Communication Systems*, Lausanne, CH, July 1995. MEAD Education.
- [Gilbert 06] B. Gilbert, “Fundamental Noise Mechanisms in BJT Circuits”, in *Low-Noise Analog IC Design*, Lausanne, CH, September 2006. MEAD Education.
- [Gonzales 97] G. Gonzales, *Microwave Transistor Amplifiers - Analysis and Design, Second Edition*, Prentice Hall, 1997.
- [Gray 01] P.R. Gray, P.J. Hurst, S.H. Lewis, and R.G. Meyer, *Analysis and Design of Analog Integrated Circuits, Fourth Edition*, John Wiley & Sons, Inc., 2001.
- [Greenberg 03] D. Greenberg, S. Sweeney, G. Freeman and D. Ahlgren “Low-Noise Performance Near BVCEO in a 200 GHz SiGe Technology at Different Collector Design Points”, in *Radio Frequency Integrated Circuits (RFIC) Symposium*, pp. 113 – 116, Philadelphia, June 2003. IEEE.
- [Gresham 01] I. Gresham, N. Jain, T. Budka, A. Alexanian N. Kinayman B. Ziegner, S. Brown, and P. Staecker “A Compact Manufacturable 76–77-GHz Radar Module for Commercial ACC Applications”, *IEEE Transactions on Microwave Theory and Techniques*, vol. 49, pp. 44 – 57, January 2001.
- [Gresham 04] I. Gresham, A. Jenkins, R. Egri, C. Eswarappa, N. Kinayman, N. Jain, R. Anderson, F. Kolak, R. Wohlert,

- S.P. Bawell, J. Bennet, and J.-P. Lanteri, “Ultra-Wideband Radar Sensors for Short-Range Vehicular Applications”, *IEEE Transactions on Microwave Theory and Techniques*, vol. 52, pp. 2105 – 2122, September 2004.
- [Grubert 03] J. Grubert, J. Heyen, C. Metz, L.C. Stange, and A.F. Jacob, “Planar millimeter wave radar frontend for automotive applications”, *Advances in Radio Science*, vol. , pp. 125 – 129, 2003.
- [Gunnarsson 05] S.E. Gunnarsson, and H. Zirath “A 60 GHz MMIC Dual-Quadrature Mixer in pHEMT technology for Ultra Wideband IF Signals and High LO to RF Isolation”, in *International Microwave Symposium (IMS)*, pp. 1991–1994. IEEE, June 2005.
- [Hall 02] L. Hall, H. Hansen, and D. Abbott, “Rotmann lens for mm-wavelengths”, *Proceedings of SPIE*, vol. 4935, pp. 215–221, 2002.
- [Hammerstad 80] E. Hammerstad, and O. Jensen, “Accurate Models for Microstrip Computer-Aided Design”, in *Microwave Symposium Digest*, pp. 407–409, 1980.
- [Hartmann 06] M. Hartmann, C. Wagner, K. Seemann, J. Platz, H. Jäger, and R. Weigel, “A Low-Power Micromixer with High Linearity for Automotive Radar at 77 GHz in Silicon-Germanium Bipolar Technology”, in *Topical Meeting on Silicon Monolithic Integrated Circuits in RF Systems (SiRF)*, pp. 237–240. IEEE, January 2006.
- [Haus 60] H.A. Haus, W.R. Atkinson, G.M. Branch, W.B. Davenport, W.H. Fonger, W.A. Harris, S.W. Harrison, W.W. McLeod, E.K. Stodola, and T.E. Talpey, “Representation of Noise in Linear Twoports”, *Proceedings of the IRE*, vol. 48, pp. 69–74, January 1960.
- [Hoffmann 83] R.K. Hoffmann, *Integrierte Mikrowellenschaltungen*, Springer Verlag Berlin, 1983.
- [Hull 93] C.D. Hull, and R.G. Meyer, “A Systematic Approach to the Analysis of Noise in Mixers”, *IEEE Transactions on Circuits and Systems – I: Fundamental Theory and Applications*, vol. 40, pp. 909–919, December 1993.
- [Hung 05] J.J. Hung, T.M. Hancock, and G.M. Rebeiz, “A 77 GHz SiGe Sub-Harmonic Balanced Mixer”, *IEEE Journal of Solid*

- State Circuits (JSSC)*, vol. 40, pp. 2167–2173, November 2005.
- [Infineon 05] Infineon and Lucent, *Abschlussbericht zum BMBF-Verbundprojekt –HiSpeed– ”Höchstperformante SiGe-Technologien für High-Speed-Kommunikationsnetze” (01M3139A)*, Bundesministerium für Bildung und Forschung (BMBF), 2005.
- [Johnson 28] J.B. Johnson, “Thermal agitation of electricity in conductors”, *Phys. Rev.*, vol. 32, pp. 97, Jul 1928.
- [Johnson 01] H. Johnson, “Slow-wave mode”, *Electronics Design, Strategy, News (EDN) Magazine*, vol. , November 2001.
- [Kaden 74] H. Kaden, “Advances in Microstrip Theory”, *Siemens Forschungs- und Entwicklungsberichte*, vol. 3, pp. 115–124, December 1974.
- [Kaleja 01] M.M. Kaleja, A.J. Herb, R.H. Rasshofer, and E.M. Biebl, “An I-Q Mixer at 76.5 GHz using flip-chip mounted silicon Schottky Diodes”, in *International Microwave Symposium (IMS)*, volume 3, pp. 1653–1656. IEEE, 2001.
- [Kim 02] J. Kim, and Y. Kwon, “Intermodulation Analysis of Dual-Gate FET Mixers”, *IEEE Transactions on Microwave Theory and Techniques*, vol. 50, pp. 1544–1555, June 2002.
- [Kirk 62] C.T. Kirk, “A Theory of Transistor Cutoff Frequency (f_T) Falloff at High Current Densities”, *IRE Transactions on Electron Devices*, vol. , pp. 164–174, March 1962.
- [Kivekäs 01] K. Kivekäs, A. Pärssinen, and K.A.I. Halonen, “Characterization of IIP2 and DC-Offsets in Transconductance Mixers”, *IEEE Transactions on Circuits and Systems – II: Analog and Digital Signal Processing*, vol. 48, pp. 1028–1038, November 2001.
- [Knapp 07] H. Knapp, B. Dehlink, H.P. Forstner, E. Kolmhofer, K. Aufinger, J. Böck, and T.F. Meister, “SiGe Circuits for Automotive Radar”, in *Topical Meeting on Silicon Monolithic Integrated Circuits in RF Systems (SiRF)*, pp. 231–236, Long Beach, CA, January 2007. IEEE.
- [Kolak 01] F. Kolak, and C. Eswarappa, “A low profile 77 GHz three beam antenna for automotive radar”, in *International Microwave Symposium (IMS)*, pp. 1107–1110, Phoenix, AZ, June 2001. IEEE.

- [Kozikowski 64] J.L. Kozikowski, “Analysis and Design of Emitter Followers at High Frequencies”, *IEEE Transactions on Circuit Theory*, vol. , pp. 129–136, Mar. 1964.
- [Krishnaswamy 07] H. Krishnaswamy, and H. Hashemi, “A Fully Integrated 24 GHz 4-Channel Phased-Array Transceiver in 0.13 μm CMOS Based on Variable-Phase Ring Oscillators and PLL Architecture”, in *International Solid State Circuits Conference (ISSCC)*, pp. 124–126. IEEE, Feb. 2007.
- [Lexus 07] Lexus, *Radartechnik und Infrarotkameran zur Unfallvermeidung: Advanced Pre Crash Safety im Lexus LS 460*, <http://www.lexus.de/>, accessed on 23.05.2007.
- [Li 04] H. Li, H.-M. Rein, T. Suttorp, and J. Böck, “Fully integrated SiGe VCOs with powerful output buffer for 77-GHz automotive Radar systems and applications around 100 GHz”, *IEEE Journal of Solid State Circuits (JSSC)*, vol. 39, pp. 1650–1658, Oct 2004.
- [Lotfi 95] A. Lotfi, and F. Lee, “Two Dimensional Skin Effekt in Power Foils for High-Frequency Applications”, *IEEE Trans. on Magnetics*, vol. 31, pp. 1003–1006, March 1995.
- [Maas 92] S.A. Maas, B.L. Nelson, and D.L. Tait, “Intermodulation in Heterojunction Bipolar Transistors”, *IEEE Transactions on Microwave Theory and Techniques*, vol. 40, pp. 442–448, Mar 1992.
- [Mayr 07] P. Mayr, C. Weyers, and U. Langmann, “A 90 GHz 65 nm CMOS Injection-Locked Frequency Divider”, in *International Solid State Circuits Conference (ISSCC)*, pp. 198–199. IEEE, Feb. 2007.
- [Mende 99] R. Mende, *Radarsysteme zur automatischen Abstandregelung in Automobilen*, PhD Thesis, Technical University Carolo-Wilhelmina at Brunswick, 1999.
- [Meyer 77] R.G. Meyer, and P.R. Gray, *Analysis and Design of Analog Integrated Circuits*, John Wiley & Sons, Inc., 1977.
- [Meyer 86] R.G. Meyer, “Intermodulation in High-Frequency Bipolar Transistor Integrated-Circuit Mixers”, *IEEE Journal of Solid-State Circuits (JSSC)*, vol. 21, pp. 534–537, Aug 1986.
- [Müller 89] R. Müller, *Rauschen*, Springer-Verlag Berlin, 1989.

- [Natarajan 06] A. Natarajan, A. Komijani, X. Guan, A. Babakhani, Y. Wang, and A. Hajimiri, “A 77GHz Phased-Array Transmitter with Local LOPath Phase-Shifting in Silicon”, *IEEE Journal of Solid-State Circuits (JSSC)*, vol. 41, pp. 2807 – 2819, Dec. 2006.
- [Niu 99] G. Niu, J.D. Cressler, W.E. Ansley, C.S. Webster, B.A. Raghunadha, and N. King, “Intermodulation Characteristics of UHV/CVD SiGe HBT’s”, in *Bipolar/BiCMOS Circuits and Technology Meeting (BCTM)*, pp. 50–54. IEEE, September 1999.
- [Niu 05] G. Niu, “Noise in SiGe HBT RF Technology: Physics, Modeling, and Circuit Implementations”, *Proceedings of the IEEE*, vol. 93, pp. 1583–1597, September 2005.
- [NTIA 07] National Telecommunications & Information Administration NTIA, “U.S. Frequency Allocation Chart”, in *www.ntia.doc.gov/osmhome/allochrt.pdf*, accessed on 21.05.2007.
- [Nyquist 28] H. Nyquist, “Thermal agitation of electric charge in conductors”, *Phys. Rev.*, vol. 32, pp. 110–113, Jul 1928.
- [Peeters 97] E.J. Peeters, M.S. Steyaert and W. Sansen, “High-Frequency Measurement Procedure for Fully Differential Building Blocks”, *IEEE Transactions on Instrumentation and Measurement*, vol. 46, pp. 1039–1043, Aug 1997.
- [Perndl 04,a] W Perndl, “Monolithic Microwave Integrated Circuits in SiGe:C Bipolar Technology”, in *Doctorate thesis*. Vienna University of Technology, Institute of Communications and Radio-Frequency Engineering, Austria, November 2004.
- [Perndl 04,b] W. Perndl, H. Knapp, M. Wurzer, K. Aufinger, T.F. Meister, J. Böck, W. Simbürger, and A.L. Scholtz, “A low-noise, and high-gain double-balanced mixer for 77 GHz automotive radar front-ends in SiGe bipolar technology”, in *Radio Frequency Integrated Circuits (RFIC) Symposium*, pp. 47–50. IEEE, June 2004.
- [Pozar 01] David M. Pozar, *Microwave Engineering, Second Edition*, John Wiley & Sons, Inc., 2001.
- [Qin 07] G. Qin, N. Jiang, G. Wang, and Z. Ma, “SiGe HBT linearity comparison between CE and CB configurations”, *Semiconductor Science and Technology*, vol. 22, pp. 216–220, January 2007.

- [Razavi 97] B. Razavi, “Design Considerations for Direct-Conversion Receivers”, *IEEE Transactions on Circuits and Systems – II: Analog and Digital Signal Processing*, vol. 44, pp. 428–435, June 1997.
- [Razavi 98] B. Razavi, *RF microelectronics*, Prentice Hall, 1998.
- [Razavi 06] B. Razavi, “A 60-GHz CMOS Receiver Front-End”, *IEEE Journal of Solid-State Circuits (JSSC)*, vol. 41, pp. 17 – 22, January 2006.
- [Rein 96] H.-M. Rein, and M. Möller, “Design Considerations for Very-High-Speed Si-Bipolar ICs Operating up to 50 Gb/s”, *IEEE Journal of Solid-State Circuits (JSSC)*, vol. 31, pp. 1076–1090, August 1996.
- [Reisch 02] M. Reisch, *High-Frequency Bipolar Transistors*, Springer-Verlag Berlin, 2002.
- [Reynolds 06] S.K. Reynolds, and J.D. Powell, “77 and 94-GHz Down-conversion Mixers in SiGe BiCMOS”, in *Asian Solid State Circuits Conference (ASSCC)*, pp. 191–194. IEEE, November 2006.
- [Rollett 62] J.M. Rollett, “Stability and Power-Gain Invariants of Linear Twoports”, *IRE Transactions on Circuit Theory*, vol. , pp. 29–32, Mar. 1962.
- [Royal School 04,a] Royal School of Artillery, *Principles of Pulsed Doppler Radar*, pp. H03–1 – H03–16, Basic Science & Technology Section (BST), May 2004.
- [Royal School 04,b] Royal School of Artillery, *The Radar Range Equation*, pp. H06–1 – H06–8, Basic Science & Technology Section (BST), May 2004.
- [Samelis 92] A. Samelis, and D. Pavlidis, “Mechanisms Determining Third Order Intermodulation Distortion in AlGaAs/GaAs Heterojunction Bipolar Transistors”, *IEEE Transactions on Microwave Theory and Techniques*, vol. 40, pp. 2374–2380, December 1992.
- [Sansen 73] W. Sansen, and R.G. Meyer, “Distortion in Bipolar Transistor Variable-Gain Amplifiers”, *IEEE Journal of Solid-State Circuits (JSSC)*, vol. 8, pp. 275–282, Aug 1973.
- [Sansen 99] W. Sansen, “Distortion in Elementary Transistor Circuits”, *IEEE Transactions on Circuits and Systems-II*, vol. 46, pp. 315–325, Mar 1999.

- [Schwerd 03] M. Schwerd, M. Seck, T. Huttner, T. Böttner, S. Drexl, B. Hasler, A. Mitchell, H. Helneder, H. Körner, V. Kubrak, M. Schrenk, and R. Lachner “A Manufacturable $0.35\ \mu\text{m}$ 150 GHz f_T SiGe:C Bipolar RF Technology”, in *Topical Meeting on Silicon Monolithic Integrated Circuits in RF Systems (SiRF)*, pp. 10–13. IEEE, April 2003.
- [Sheng 03] L. Sheng, and L.E. Larson, “An SiSiGe BiCMOS Direct-Conversion Mixer With Second-Order and Third-Order Non-linearity Cancellation for WCDMA Applications”, *IEEE Transactions on Microwave Theory and Techniques*, vol. 51, pp. 2211–2220, November 2003.
- [Shimura 98] T. Shimura, Y. Kawasaki, Y. Ohashi, K. Shirakawa T. Hirose, S. Aoki, H. Someta, K. Makiyama, and S. Yokokawa, “76 GHz Flip-Chip MMICs for Automotive Radars”, in *Radio Frequency Integrated Circuits (RFIC) Symposium*, pp. 25–28. IEEE, 1998.
- [Strohm 05] K.M. Strohm, H.-L. Bloecher, R. Schneider, and J. Wenger, “Development of Future Short Range Radar Technology”, in *European Microwave Week*, pp. 165 – 168. EUMA, EUMW Technical Digest, October 2005.
- [Terrovitis 00] M.T. Terrovitis, and R.G. Meyer, “Intermodulation Distortion in Current-Commutating CMOS Mixers”, *IEEE Journal of Solid-State Circuits (JSSC)*, vol. 35, pp. 1461–1473, Oct 2000.
- [Trotta 06] S. Trotta, H. Knapp, K. Aufinger, T.F. Meister, J. Böck, W. Simbürger, and A.L. Scholtz, “An 84 GHz Bandwidth and 20 dB Gain Broadband Amplifier in SiGe Bipolar Technology”, in *Compound Semiconductor Integrated Circuit (CSIC) Symposium*, pp. 21–24, San Antonio, USA, Nov 2006. IEEE.
- [Trotta 07,a] S. Trotta, B. Dehlink, H. Knapp, K. Aufinger, T.F. Meister, J. Böck, W. Simbürger, and A.L. Scholtz, “SiGe Circuits for Spread Spectrum Automotive Radar (Invited)”, in *accepted at International Conference on Ultra-Wideband (ICUWB)*, Singapore, Sep. 2007. IEEE.
- [Trotta 07,b] S. Trotta, H. Knapp, D. Dibra, K. Aufinger, T.F. Meister, J. Böck, W. Simbürger, and A.L. Scholtz, “A 79 GHz SiGe-Bipolar Spread-Spectrum TX for Automotive Radar”, in *International Solid-State Circuits Conference (ISSCC)*, pp. 430 – 431, San Francisco, USA, Feb. 2007. IEEE.

- [Vizmuller 95] P. Vizmuller, *RF Design Guide: Systems, Circuits, and Equations*, Artech House, Inc., 1995.
- [Vytla 06] R.K. Vytla, T.F. Meister, K. Aufinger, D. Lukashevich, S. Boguth, H. Knapp, J. Böck, H. Schäfer, and R. Lachner, “Simultaneous Integration of SiGe High Speed Transistors and High Voltage Transistors”, in *Bipolar/BiCMOS Circuits and Technology Meeting (BCTM)*. IEEE, October 2006.
- [Wambacq 98] P. Wambacq, and W. Sansen, *Distortion Analysis of Analog Integrated Circuits*, Kluwer Academic Publishers, 1998.
- [Wang 06] L. Wang, R. Kraemer, and J. Borngraeber, “An Improved Highly-Linear Low-Power Down-Conversion Micromixer for 77 GHz Automotive Radar in SiGe Technology”, in *International Microwave Symposium (IMS)*, pp. 1834–1837. IEEE, June 2006.
- [Weinrichter 91] H. Weinrichter, and F. Hlawatsch, *Stochastische Grundlagen Nachrichtentechnischer Signale*, Springer-Verlag Berlin, 1991.
- [Weiss 04] F. Weiss, “Modeling of Monolithic Integrated Transmission Lines”, in *Diploma thesis*. Vienna University of Technology, Institute of Communications and Radio-Frequency Engineering, Austria, September 2004.
- [Welch 99] R. Welch, T. Jenkins, K. Kehias, C. Bozada, C. Cerny, G. DeSalvo, R. Dettmer, J. Ebel, J. Gillespie, K. Nakano, C. Pettiford, T. Quach, J. Sewell, D. Via, and R. Anholt “The Effects of Feedback Capacitance on Thermally Shunted Heterojunction Bipolar Transistors Linearity”, in *International Conference on Compound Semiconductor Manufacturing Technology*. GaAs MANTECH, 1999.
- [WGSE 05] Working Group ”Spectrum Engineering” WGSE, “Radio Frequency Channel Arrangements for Fixed Service Systems Operating in the Bands 71–76 GHz and 81–86 GHz”, in *ECC Recommendation (05)07*, pp. 1–6, 2005.
- [WHO 07] World Health Organization WHO, “Road safety: A public health issue”, in http://www.who.int/features/2004/road_safety/en/, accessed on 21.05.2007.

[Yau 06]

K.H.K. Yau, and S.P. Voinigescu, “ Modeling and extraction of SiGe HBT noise parameters from measured Y-parameters and accounting for noise correlation”, in *Topical Meeting on Silicon Monolithic Integrated Circuits in RF Systems (SiRF)*, pp. 226–229. IEEE, January 2006.

Curriculum Vitae

Personal Details

Name: **Bernhard Dehlink**
Date & Place of Birth: 06.10.1979 in Mödling / Austria
Home Address: Kapellenstrasse 5
82008 Unterhaching
Germany
Tel.: +49 (0)176 24342096
E-mail: bernhard.dehlink@gmx.net

Education

09/2004 – 07/2007 **Doctorate student**
Vienna University of Technology / Infineon Technologies AG
"Integrated MM-Wave Frontend Design in SiGe Bipolar Technology"
PhD advisor: Prof. Arpad L. Scholtz

23/04/2004 **Diploma Degree** with distinction
Vienna University of Technology
Diploma Thesis: "Atmospheric Impact on Laser Beam Propagation"

1998 – 2004 **Study of Electrical Engineering**, specialization in Communications and Radio Frequency Engineering

1997 – 1998 Military Service
1997 Matura (Qualification for university entrance)

Training

<i>12/11/2006</i>	RF and High Speed CMOS , Short Course, IEEE Compound Semiconductor IC Symposium (CSICS), San Antonio, TX
<i>04/09/2006 – 07/09/2006</i>	Low-Noise Analog IC Design , Intensive Course, Swiss Federal Institute of Technology (EPFL), Lausanne
<i>11/06/2006</i>	Si Bipolar and CMOS MM-wave ICs , Short Course, IEEE International Microwave Symposium (IMS), San Francisco, CA
<i>27/06/2005 – 01/07/2005</i>	RF Transceivers and Power Amplifiers , Intensive Course, Swiss Federal Institute of Technology (EPFL), Lausanne

Professional Experience

<i>Infineon Technologies AG</i> <i>09/2004 – 07/2007</i>	Doctorate student (Vienna University of Technology) Fields of Work: Design and characterization of – Receiver circuits for 77 GHz automotive radar [Dehlink 05, Dehlink 06,b, Knapp 07] – Receiver front-ends for communication purposes at 80 GHz [Dehlink 06,a]
---	--

Computer Skills

- Design Environments: ADS, CADENCE
- Maths Tools: Matlab, Mathematica
- EM-Simulators: Maxwell2D, HFSS
- Programming Languages: Delphi / Pascal, ASM, Labview
- OS: LINUX, Win2k, WinXP
- Text Processing: LaTeX, Microsoft Office

Language Skills

German (first language), English (fluent), French (good working knowledge)

References

Prof. Arpad L. Scholtz
(PhD advisor)

Vienna University of Technology
Vienna, Austria
email: arpad.scholtz@tuwien.ac.at
Tel.: +43 1 58801 38945

Dr. Werner Simbürger
(Head of Department)

Infineon Technologies AG
Munich, Germany
email: werner.simbuenger@infineon.com
Tel.: +49 89 234 48432

Dr. Hans-Dieter Wohlmuth
(former advisor at Infineon)

Frequentis GmbH
Vienna, Austria
email: hans-dieter.wohlmuth@frequentis.com
Tel.: +43 1 811504 112

Dr. Herbert Knapp
(advisor at Infineon)

Infineon Technologies AG
Munich, Germany
email: herbert.knapp@infineon.com
Tel.: +49 89 234 52018